AN INVESTIGATION ON THE EFFECTS OF MAGNETIC SHIELDING AND THE THERMOELECTRIC SEEBECK EFFECT FOR SRF APPLICATIONS

By

Spencer Combs

A THESIS

Submitted to
Michigan State University
in partial fulfillment of the requirements
for the degree of

Accelerator Science and Engineering – Master of Science

2025

ABSTRACT

The Facility for Rare Isotope Beams (FRIB) driving linear accelerator operates using 324 superconducting cavities, which operate with 80.5 MHz Quarter Wave Resonators (QWRs), and 322 MHz Half Wave Resonators (HWRs) respectively with four operational beta values. Improving the performance of these cavities, meaning increasing the Quality factor (Q) value, which is a factor of efficiency of power into the cavity versus power into the beam, will therefore improve the operation of scientific endeavors within FRIB. The FRIB 322 MHz HWRs are operated at a temperature of 2 Kelvin. At this frequency and temperature, Bardeen-Cooper-Schrieffer (BCS) surface resistance is negligible (0.5 nΩ). Residual surface resistance is the remaining dominant factor in this relationship, which is valued at around ~5 nΩ. Current R&D efforts indicate that residual surface resistance due to flux trapping causes 80% of losses within the cavity. One of the contributing factors of flux trapping within the cavity is the static ambient magnetic field present during cool down; a combination of residual magnetic flux from surrounding parts, and the earth's background field. Another possible contribution is from thermoelectric current effects generated by dissimilar metals at a temperature gradient, known as the Seebeck effect. This occurs while the niobium cavity is undergoing cryogenic cooling to reach the superconducting phase transition. A reduction strategy to limit these two contributing factors is to shield against the static magnetic field and eliminate the thermoelectric Seebeck effect in the subcomponents. The goal of this thesis is to understand and mitigate the residual surface resistance generated by static magnetic fields and thermoelectric Seebeck effects to allow for a higher intrinsic Q value (Q_0), and for the cavity to operate at a higher field. The research focuses upon 1) measuring the effectiveness of local magnetic shielding on the cavity, 2) demonstrating the thermoelectric Seebeck effect is generated by different metals during cryogenic cool down, and 3) measurement of the magnetic flux generated by these thermoelectric Seebeck effects. This thesis will conclude with paths forward to reduce the Seebeck coefficients on the cavity, improving operational performance and opening up possibilities of operating the $\beta = 0.53$ half wave resonating FRIB cavities at double their specification values, which would result in a Q_0 greater than 3E10, and with $E_{acc} = 15$ MV/m.

ACKNOWLEDGEMENTS

This paper could not have been possible without the immense support and assistance from the SRF and Superconducting magnet department at Michigan State University. I would like to thank the following people for assisting in their own ways towards my thesis:

Kenji Saito, my advisor, for always supporting and guiding me.

Ting Xu, for supporting me after Kenji retired, and always providing sound advice.

Chris Compton, for assistance with my thesis experimentation.

Laura Popielarski, for her help in scheduling and data management.

Joeseph Asciutto, for his unwavering support in creating sample, fabricating my system, and helping me complete measurements even after hours.

Andrew Koren, for assisting with the 3D modeling of the initial apparatus, and for his assistance in measurements.

Anthony DeMaio, for assisting with experimentation and readying each trial.

Hai Nguyen, for procuring equipment that enabled me to make these measurements.

Ryan Bliton, for loaning me his department's instrumentation when I needed it most.

Wei Chang, for his immense support in data acquisition and instrumentation calibration.

Spencer Drake, for his support with mechanical welding and sample fabrication.

My friends and fellow classmates for encouraging me.

Lastly, my family, for supporting me all this time.

Thank you all.

TABLE OF CONTENTS

1.Introduction

1.1 Overview of SRF projects

1.1.1 SRF Electron/proton accelerator projects

Superconducting radio-frequency cavities (SRF) are an application of superconductivity for radio frequencies. This technology has been in development for over 60 years since the initial research at Stanford University, USA in the 1960's, and is still evolving [1.1]. This technology allows for continuous operation of the beam and provides high quality beams at low operating power costs. It is used in the 12 GeV CW electron beam accelerator at the Thomas Jefferson National Laboratory (JLAB) [1.2], the European XFEL (electron beam) built and under operation at the Deutsches Elektronen-Synchrotron (DESY) in Hamburg and Zeuthen in Germany [1.3], and the SNS proton beam accelerators at Oak Ridge National Laboratory (ORNL) (pulsed beam operation) for neutron production [1.4]. The Facility for Rare Isotope Beams (FRIB) heavy ion accelerator built at Michigan State University, East Lansing, MI, USA [1.5] and the Linac (short for linear accelerator) Coherent Light Source (LCLS-II) X-FEL accelerator (long pulse electron beam operation) recently built at the Stanford Linear Accelerator Center (SLAC) in Menlo Park, CA [1.6] also use this technology. More projects that make use of SRF technology are the PIP-II 8GeV proton CW beam machine, currently under construction at the Fermi National Accelerator Laboratory (FNAL) in Batavia, IL, USA [1.7], and the upcoming electron ion collider (EIC) at Brookhaven National Laboratory (BNL), Long Island, New York [1.8]. Future projects like the international linear collider (ILC) in Japan [1.9], the future circular collider (FCC) proposed for the European Organization for Nuclear Research (CERN) in Meyrin, Geneva, Switzerland [1.10], and the circular electron positron collider (CEPC) proposed for China [1.11] would all be using superconducting RF cavities.

First, 1.5th, and 2nd-generation SRF large-scale projects on electron/proton

On the topic of electron beam acceleration, one of the first generation large scale SRF machines was TRISTAN SRF at the High Energy Accelerator Research Organization (KEK), in Tsukuba, Ibaraki, Japan [1.12]. Another few were the LEP-II at CERN, in Meyrin, Geneva, Switzerland [1.13], CESR SRF at Cornell University in Ithaca, NY, USA [1.14], HERA Electron Ring at DESY [1.15], Germany and CEBAF at Thomas Jefferson laboratory [1.16], which was under construction from 1989 until 2000. The former three machines were all electron/positron ring colliders, with the fourth one being an electron/proton collider. Each of these 1st gen machines accelerate several tens of milliamps of electron or positron beams by CW at an E_{acc} value of roughly 5 MV/m at a Q_0 value of roughly $1x10^9$ at a temperature of 4.3 Kelvin. By distinction, CEBAF is an electron recirculation machine with four turns, and accelerated electron beams of several hundreds of microamps, with an energy of up to 4GeV, operated at an E_{acc} value of roughly 5 MV/m at a Q_0 value of roughly $3x10^9$ at a temperature of 2 Kelvin.

Some 1.5 generation machines are the KEKB at KEK, in Japan, which was a post TRISTAN [1.17] machine, the CESR B-factory was a post CESR SRF [1.18] machine, of which, the RF cavity performance is similar to the first generation, but with the accelerating beam increased to currents greater than 1A. These high current SRF machines were under construction from 1995 to 2005. KEKB and PEP-II (normal conducting RF) at SLAC had discovered the CP violation in B-mesons, Drs. M. Kobayashi and T. Masukawa were awarded the Nobel Prize in 2008 because of this discovery. CERN has constructed the LHC [1.19], for proton-proton circulating collisions using

the LEP tunnel. The LHC helped facilitate the discovery of the Higgs boson. The researchers, Drs. P. W. Higgs and F. Englert, were awarded the Nobel prize in 2013 for this discovery. Some second-generation machines include the SNS at ORNL, a superconducting linac used to accelerate a proton beam [1.20], the superconducting electron linac EURO-XFEL at DESY [1.21], the LCLS-II [1.22] and the LCLS-II-HE at SLAC [1.23]. All three are superconducting electron linacs which are operated at an E_{acc} value of between 10 – 25 MV/m at a Q_0 value equal to between 1E+10 and 2.5E+10 at a temperature of 2 Kelvin. These machines began construction in 2010, and have not yet finished.

1.1.2 SRF Heavy Ion Accelerator Projects

First Generation machine for heavy ion beam

Then there are SRF heavy ion accelerators, which use charged ions of heavy elements to create high-energy beams that impact on targets, or with other particles. The following four examples are part of the first generation of these machines. These are: the Atlas machine at Argonne National Laboratory (ANL), in Lemont, Illinois (USA) [1.24], the tandem-booster at JAERI, in Tokai, Japan [1.25], the Acceleratore Lineare Per Ioni (ALPI) at the Istituto Nazionale di Fisica Nucleare (INFN) in Legnaro, Italy [1.26], and the Isotope Separator and Accelerator (ISAC-II) at TRIUMF in Vancouver, Canada[1.27]. ANL started their SRF research and development of heavy ion beam acceleration in 1973 and produced pioneering works in cavity structures and surface preparation. The prototype ATLAS machine successfully accelerated its first ion beam in June of 1978, with an expansion installation of four modules, including 24 cavities in total, in 1983. Their success had a marked impact on other first generation projects, namely on the idea that SRF technology can allow for high quality, high energy beams for heavy ion accelerators. The JAERI tandem-booster finished construction in 1994, and used 46 Quarter Wave Resonators (QWRs). Their cavity housing used Nb/Cu explosive bonded material, similar to the ATLAS machine at ANL. These cavities had an E_{acc} operating value within a range of 4.1 to 5.0 MV/m, at a Q_0 value close to $4x10^8$. ALPI also used QWRs, but these were made with Pb electroplated on copper, Nb/Cu sputtering, and full Nb cavities. This machine succeeded in its first beam acceleration in 1994. ISAC-II, a 20MV superconducting linac, was commissioned in 2006, and started operation in 2009. The cavities within ISAC-II had an E_{acc} operating value of around 6MV/m at a Q_0 value of around $1x10^9$.

The second generation of SRF heavy ion projects

Some second-generation SRF heavy ion beam facilities are the SPIRAL2 at the Grand Accélérateur National d'Ions Lourds (GANIL), in Caen, France [1.28], and the Facility for Rare Isotope Beams (FRIB) at MSU, East Lansing, in the USA [1.15]. SPIRAL2 is an 80 MeV SRF linear accelerator consisting of 26 accelerating cavities, enclosed in 19 cryomodules. It accelerates heavy ions up to the size of nickel, at intensities 10 times greater than other currently available machines do. It has been used in routine operation to conduct experiments at the Neutrons for Science Facility (NFS) since 2021. The FRIB machine was completed in February of 2022. A goal of this machine was to accelerate particles from as small as a proton to ions like Uranium, with an energy of up to 200 MeV per nucleon, in which it had great success. Another goal of this facility is to have heavy ions hit the target at a power of 400kW to produce high intensity radio-isotopes. The power of this machine is being upgraded steadily, and has been upgraded to 22kW as of September of 2024. Power updates will continue until 2028. FRIB is operated at an E_{acc} value of

about 6 MV/m at a Q_0 value of about $2x10^9$ at a temperature of 4.3K in its QWRs and an E_{acc} value of about 6-8 MV/m at a Q_0 value of about $1x10^{10}$ at a temperature of 2K in Half Wave Resonators (HWRs). The FRIB machine will be described in the last part of this section.

1.2 Power load on liquid refrigerators

The machines mentioned above used large capable liquid helium refrigerators, like those at 5 kW class at a temperature of 4.3K or 2K. The cooling efficiency of liquid helium is ~ 1/1000 at 4.3 K and ~ 1/3000 at 2 K. In other words, to remove 1W of heat, 1KW of power is required for cooling at 4.3 K, and 3KW for 2K. For example, with the FRIB machine, 5kW at 2K means consuming 15MW of power [21]. Even if the machine is superconducting, such an electric consumption is a big load for an institute. Knowing this, for the 3rd generation machines, many R&D operations are carried out in order to reduce the power dissipation of SRF cavities [1.9]. Another potential outcome of this thesis is the improvement of Q_0 performance within SRF cavities, and to reduce power dissipation. The details of this will be seen in the motivation section for chapter 2.

1.3 RF dissipation in SRF cavities

SRF cavities have a small surface resistance. It is about five to six orders of magnitude smaller compared to normal conducting cavities. As a result, RF dissipation, a mechanism caused by surface resistance, occurs on the SRF cavity surface, as seen in equations 1.3 and 1.4. This surface resistance depends on cavity resonant frequency, f, and cooling temperature, T, and is formulated as [1.29]:

$$R_s(f,T) = R_{BCS}(f,T) + R_{res} \tag{1.1}$$

$$R_{BCS}(f,T) = \frac{Af^2}{T} e^{\frac{-\Delta}{k_B T}} \tag{1.2}$$

Here, R_{BCS} is calculated using the BCS theory and is called BCS surface resistance. A is a constant value, k_B is known as the Boltzmann constant. On the other hand, R_{res} is a constant, which reflects the surface contamination and the ambient magnetic field in the cryostat. It is known as the residual surface resistance. RF dissipation can be described as:

$$P_{loss} = \frac{1}{2} R_s \int H_S^2 dS \tag{1.3}$$

Where Hs is the RF magnetic field on the cavity's surface. The intrinsic quality factor Q_o is defined as:

$$Q_0 = \frac{\omega U}{P_{loss}} = \frac{G}{R_S} \tag{1.4}$$

Here, ω is the angular frequency (ω=2πf), U is the stored energy in the cavity, and G is the geometrical factor. The accelerating gradient is calculated as:

$$E_{acc} = Z\sqrt{Q_o P_{loss}} \tag{1.5}$$

Here, Z is a constant value.

$$P_{loss} = \frac{E_{acc}^2}{Z^2 Q_0} \tag{1.6}$$

Where Z is

$$Z = \frac{\sqrt{\frac{R_{sh}}{Q_0}}}{L_{eff}} \tag{1.7}$$

and L_{eff} is the effective length of the cavity, R_{sh} is the shunt impedance, and Q_0 is the quality

factor.

The main factors that determine the operating power consumption of SRF cavities are the Q_0 value of the cavity and the accelerating gradient, represented by E_{acc}. From equation 1.4, the Q_0 value is inversely proportional to the surface resistance of the cavity, and the higher Q_0 produced, the less dissipation there is on the SRF cavity surface. From equation 1.6, the electric power consumption is reduced inversely proportional to Q_0. On the other hand, at a fixed Q value, the operating power increases in proportion to the square of the accelerating gradient. For example, if the FRIB's β=0.53 (where $\beta = V/c$) half-wave resonators (0.53HWR) are to be operated at 15 MV/m, which is double the current specification of 7.4 MV/m with $Q_0 = 7.6 \times 10^9$. Then, within the cooling capacity of the existing FRIB cryoplant, the Q factor would need to be increased, up to 3×10^{10}.

1.4 High Q and high gradient performance required for the third generation SRF projects

A high Q and high accelerating gradient is required in an SRF Cavity for CW operation, especially for the LCLS-II project [1.30]:

Total electron beam energy is 4GeV,
32 cryomodules including 8 ILC-type 1.3GHz cavities in each cryomodule,
Long pulse operation at 3.5ms,
An E_{acc} value of 16 MV/m at a Q_0 value of 2.7E+9.

The nitrogen doping method, using a furnace operated at 800-900^{O}C, was successfully developed to enhance the Q value from 1.5E+10 to 2.7E+10 at E_{acc}=16MV/m. Currently, SLAC is constructing the LCLS-II HE, using further improved N-doping furnace technology, where cavities will be operated at an E_{acc} value of 23 MV/m at a Q_0 value of 2.7E+10. The energy of the LCLS-II HE machine increases up to 8GeV, but it is not alone, with there being an increase in the LCLS-II machine to 8 GeV as well [1.24]. This Nitrogen doping can reduce the BCS surface resistance [25], therefore allowing SRF cavities to become more effective at a higher operational frequency. At a low frequency of 322 MHz, like FRIB 0.53HWR operated 2K, BCS surface resistance is only 0.5 nΩ. The surface resistance, from investigation, is dominated by residual resistance. This nitrogen doping method is not so effective. To push up the Q value of its cavities, FRIB has to develop its own technology to reduce the residual surface resistance.

1.5 FRIB Machine

The FRIB machine configuration is shown in Fig. 1.1 [1.31]. It was built on the main campus of Michigan State University to strengthen studies in isotope nuclear physics. This machine consists of three folded SRF linear accelerators. The FRIB machine configuration is as follows [1.31]. Uranium ions are produced by the Electron Cyclotron Resonator (ECR) and after the injection energy of 0.5 MeV, are accelerated by superconducting LINACs. The front of the first LINAC, LS1, has three cryomodules, each one including four β= 0.041 (80.5 MHz) quarter wave resonators and two superconducting thirty centimeter solenoids. The second section of the LS1, which has eleven cryomodules, each one including eight β = 0.085 (80.5 MHz) quarter wave resonators and three superconducting sixty centimeter solenoids. Heavy ions are accelerated up to 18MV per nucleon by LS1 before the beam is turned by 180^O via normal conducting bending dipole magnets, and enters the LS2 linear accelerator. For more information, please refer to additional documentation (see source 1.31).

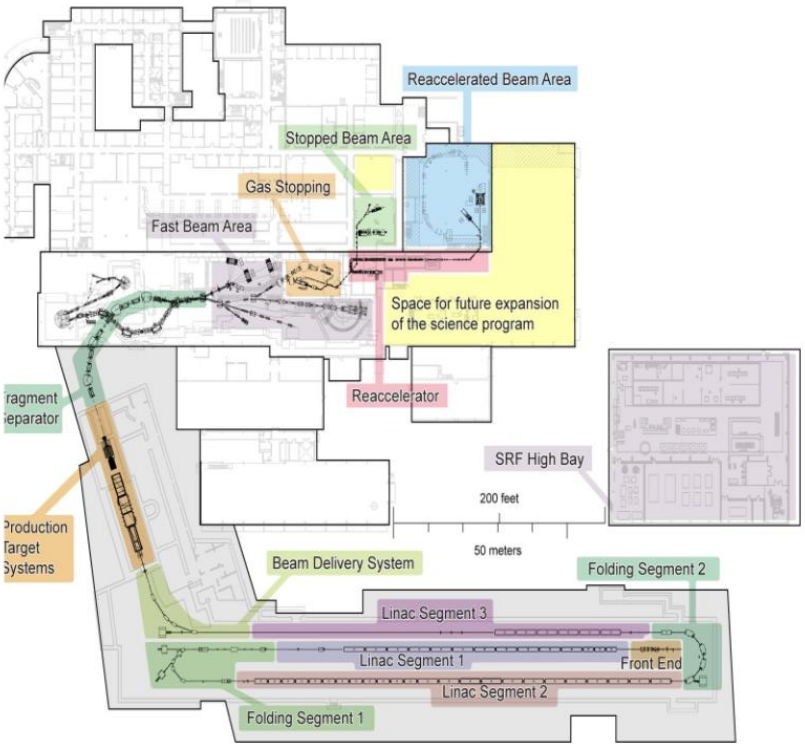

Figure 1.1 - FRIB Machine Configuration

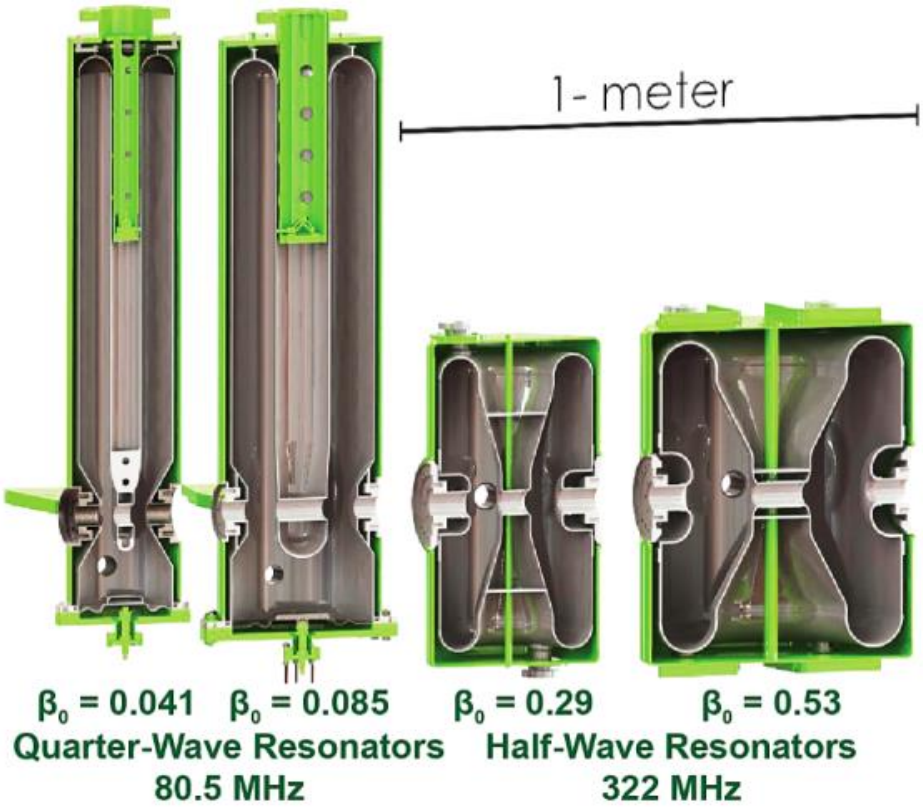

Figure 1.2 – FRIB Cavities

Maintainability for FRIB reliable user operation

The CD4 review of FRIB was successfully held on Feb. 1st and 2nd of 2022. Shortly thereafter, MSU announced the completion of FRIB. FRIB has since changed from the construction phase to the user service phase. Now FRIB is one of the four facilities NP operated, with FRIB being a 200 MeV per nucleon, 400 kW superconducting radio frequency (SRF) based linac with a variety of rare isotope beams for use in the study of nuclear structure and nuclear astrophysics. In the step-phased beam commissioning, FRIB superconducting cryomodules demonstrated an excellent SRF performance of a high Q value and a high accelerating gradient. The power of the machine started at several watts and currently has increased up to 22kW as of September 2024. The current power upgrade plan is to reach 400kW by 2028. In the power upgrade, the most difficult obstacles will be advances in the target and beam dump, which easily burn out due to the very thin Bragg peak on the heavy ions.

In parallel to the power upgrade, FRIB has been in use by researchers for nuclear science. In this service, the FRIB facility must maintain a high capability for operation, as well as reliability, in providing accelerated beams. The SRF and superconducting magnets department at FRIB takes this responsibility as the highest priority, and set research and development programs for these purposes. As is described in next section, in April 2022, a proposal was submitted to the DOE to enhance the FRIB machine's maintainability. Furthermore, a proposal was submitted to the DOE to aim for transformative accelerator research and development in SRF technology for restoring and increasing cavity performance in FRIB spare cryomodules. The goal of this proposal is to develop $\beta = 0.53$ HWRs operable at accelerating gradients of E_{acc} values greater than 10 MV/m, keeping a high Q_0 value of greater than $1x10^{10}$ for the restoration or construction of FRIB spare cryomodules.

Bibliography:

[1.1] H. Padamsee, “History of gradient advances in SRF”, https://arxiv.org/pdf/2004.06720

[1.2] P.A. Adderley, et al., “The Continuous Electron Beam Accelerator Facility at 12 GeV”, Phys. Rev. Accelerator and Beams 27, 084802 (2024), https://arxiv.org/pdf/2004.06720

[1.3] C. Schmidt et al., “Operational Experience with the European XFEL LINAC”, Proc. SRF2023, Grand Rapids, MI, USA, pp.34-50., https://inspirehep.net/literature/2723461

[1.4] Sang-ho Kim, “SNS Superconducting LINAC Operation Experience and Upgrade Path”, Proc. of LINAC08, Victoria, BC, Canada, MO103, pp. 11-15, https://accelconf.web.cern.ch/LINAC08/papers/mo103.pdf

[1.5] J. Wei, et al., “FRIB Commission and Early Operations”, Proc. of IPAC2022, Bangkok, Thailand, pp. 802-807. https://inspirehep.net/files/70d43f98284ff26bf6882e6b6e4f72b6

[1.6] A. Brachmann, “LCLS-II Commissioning Results”, Proc. of 14th International Particle Accelerator Conference (IPAC2023), Venice, Italy, pp.13-14. https://inspirehep.net/files/ccfe756f8c8411c8398da1483fe81bae

[1.7] R. Stanek, et al., “PIP-II Project Overview and Status”, Proc. of SRF2023, Grand Rapids, MI, USA,

pp.19-24. https://inspirehep.net/files/ccfe756f8c8411c8398da1483fe81bae

[1.8] C. Montag, et al., “The ECI Accelerator: Design Highlights and Project Status”, Proc. of 15th International Particle Accelerator Conference (IPAC2024), Nashville, TN, USA, pp.214-217. https://inspirehep.net/files/05ec5ca362004ecdb9564757f34bdb3a

[1.9] S. Michizono, “Current Status and Future Technological Collaboration for the ILC”, Proc. of SRF2023, Grand Rapids, MI, USA, https://accelconf.web.cern.ch/srf2023/talks/wekea01_talk.pdf

[1.10] CERN Homepage, https://home.cern/science/accelerators/future-circular-collider

[1.11] CEPC/IHEP Homepage, http://cepc.ihep.ac.cn/intro.html

[1.12] Yuzo Kojima, et al., “Superconducting RF Activities at KEK”, Proc. of the fourth Workshop on RF Superconductivity (SRF89), KEK, Tsukuba, Japan, 1989, A07, pp.85-95. https://accelconf.web.cern.ch/SRF89/papers/srf89a07.pdf

[1.13] P. Brown et al, “Operating Experience with the LEP2 Superconducting RF System”, Proc. of the 10th Workshop on RF Superconductivity, 2001, Tsukuba, Japan, pp.185-193. https://accelconf.web.cern.ch/srf01/papers/sa001.pdf

[1.14] S. Belomestnykh, et al., “Operating Experience with Superconducting at CESR and Overview of Other SRF Related Activities at Cornell University”, Proc. of the 1999

Workshop on RF Superconductivity, Santa Fe, New Mexico, USA, pp.24-30. MOA006.

https://accelconf.web.cern.ch/SRF99/papers/moa006.pdf

[1.15] B. Dwersteg, et al., "Operational Experience with Superconducting Cavities in the HERA E-Ring", Proc. of the 1995 Workshop on RF Superconductivity (SRF95), Gif-sur-Yvette, France, 1995, SRF95E02, pp.151-160.
https://accelconf.web.cern.ch/SRF95/papers/srf95e02.pdf

[1.16] C. Reece et al., "Performance of Production SRF Cavities for CEBAF", Proc. of the 1993 Particle Accelerator Conference, pp.1016-1018.

file:///C:/Users/Saito/Downloads/Performance_of_production_SRF_cavities_for_CEBAF.pdf

[1.17] T. Furuya et al., "Superconducting Accelerating Cavity for KEK B-Factory", Proc. of the 1995 Workshop on RF Superconductivity", Gif-sur-Yvette, France, 1995, pp.729-733.
https://epaper.kek.jp/SRF95/papers/srf95f35.pdf

[1.18] H. Padamsee et al., "Accelerating Cavity Development for the Cornell B-Factory, CESR-B", https://ieeexplore.ieee.org/stamp/stamp.jsp?tp=&arnumber=164441

[1.19] D. Boussard et al., "THE LHC Superconducting Cavities", Proc. of the 1999 Particle Accelerator Conference, New York, USA, 1999. Pp.946-948.
https://cds.cern.ch/record/386691/files/mop120.pdf

[1.20] S.-H. Kim et al., "Overview of ten-year operation of the superconducting linear accelerator at the Spallation Neutron Source", Nuclear Inst. and meth. In Phys. Res. Sec. A: Accelerators, Spectrometers, Detectors and Associated Equipment. 2012.
https://www.sciencedirect.com/science/article/pii/S0168900217301894

[1.21] N. Walker et al., "Performance Analysis of the European XFEL SRF Cavities from Vertical Test to Operation in Modules", Proc. of LINAC2016, East Lansing, MI, USA. pp. 657-662. https://accelconf.web.cern.ch/linac2016/papers/we1a04.pdf

[1.22] Dan Gonnella, "LCLS-II Commissioning".
https://accelconf.web.cern.ch/linac2022/talks/mo2aa02_talk.pdf

[1.23] SLAC home page, LCLS Linac Coherent Light Source,

https://lcls.slac.stanford.edu/lcls-ii-he

[1.24] M.P. Kelly, "Superconducting RF Cavities at ARGONNE National Laboratory", Proc. of the 10th workshop on RF superconductivity, 2001, Tsukuba, Japan. pp. 1-5.
https://accelconf.web.cern.ch/srf01/papers/tl001.pdf

[1.25] S. Takeuchi, et al., "First Three Year Operational Experience with the JAERI Tandem-booster", Proc. of the eighth workshop on RF Superconductivity, Abano Terme (Padova),

Italy, 1997. pp. 237-247. https://accelconf.web.cern.ch/SRF97/papers/srf97a26.pdf

[1.26] G. Bisoffi, et al., "ALPI QWR and S-RFQ Operating Experience", Proc. of SRF2007, Peking University, Beijing, China. pp. 55-62. https://accelconf.web.cern.ch/srf2007/PAPERS/MO404.pdf

[1.27] R.E. Laxdal et al., "ISAC-II: Status of the 20 MV Upgrade", Proc. of the SRF2009, Berlin, Germany. pp. 81-87. https://accelconf.web.cern.ch/SRF2009/papers/moodau05.pdf

[1.28] A. Orduz, "SPIRAL2 Commissioning and Operations", HB2023,

https://accelconf.web.cern.ch/hb2023/talks/tua3i1_talk.pdf

[1.29] Hasan Padamsee, Jens Knobloch, & Hays, T. (2008). *RF superconductivity for accelerators*. Wiley-Vch.

[1.30] P. Bishop et al., "LCLS-II SRF Cavity Performance PROTOCOL Development and Beamline Cavity Performance Demonstration", Proc. of SRF1015, Whistler, BC, Canada, pp.159-163. https://accelconf.web.cern.ch/SRF2015/papers/mopb033.pdf

[1.31] FRIB Parameter List, T1050-BL-000002-R018, Issued 24 April 2020.

2. DOE Grants and Motivation

2.1 DOE grant

In August of 2022, the R&D proposal entitled "Transformative accelerator R&D in SRF technology for restoring and increasing cavity performance in FRIB spare cryomodules" received a grant from the DOE (RC114424). Cavity production for the FRIB project had concluded at that time, but this proposal geared toward future FRIB spare cryomodules that would replace degraded cavities, which may occur during the long-term operation of the FRIB accelerator. Of the six FRIB cryomodule families, three have certified spares that were fabricated as part of the project baseline. The spare $\beta = 0.29$ and 0.53 cryomodules were not included in the baseline project, but are being planned within the future scope of maintenance for the FRIB machine. These spare cryomodules will utilize existing cavities that have been fabricated as part of production contracts. These spare cryomodules and cavities must have a high enough performance margin against further degradation during the lifetime of the machine's operation to be considered viable.

2.2 DOE grant R&D results

In this project, the primary study was of performance enhancement, specifically the accelerating gradient performance. Buffered chemical polishing using acid consisted of the following ratio: $HF:HNO_3:H_3PO_4 = 1:1:2$. This mixture, called BCP, was used for the production of cavities for FRIB. The resultant cavity performance is shown in Figure 2.1 for all FRIB production $\beta = 0.53$ HWRs [2.1]. This figure shows the statistics of performance for an FRIB $\beta = 0.53$ HWR during the certification test (vertical measurement) at a temperature of 2 K, to mimic operating conditions. All of these $\beta = 0.53$ HWR cavities exceeded FRIB specifications (represented by a star mark in Figure 2.1), however, the test data shows a Q drop onset, beginning at roughly 8 MV/m (B_p at around 85 milliTesla). This drop in the Q value limits the potential machine operation at accelerating gradients greater than 10 MV/m. In these Q drops, two different mechanisms combine: field emission (FE), which accompanies strong X-ray emission events, and another one referred to as a high field Q slope (HFQS). Here, the HFQS has two typical behaviors: the first being when the Q-drop does not accompany any X-ray events (pure HFQS), and secondly, when it accompanies weak X-ray events at a higher field than that of the onset of the HFQS (suspicious HFQS).

Table 2.1 summarizes the statistics of the field limit of all types of cavities seen in production at FRIB [2.1]. The proportion of $\beta = 0.53$ FRIB HWRs with field limits caused by FE is 74% and by HFQS is 25%. These two are the main limiting factors of the potential high gradient (E_{acc} greater than 10 MV/m) operation of FRIB cavities. Buffered chemical polishing (BCP) can treat these problems. The issues of FE and HFQS are mitigated or resolved by the research conducted as part of this project.

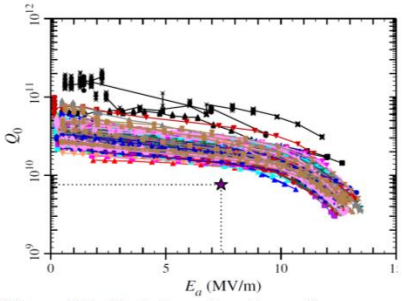

Figure 2.1: Statistics of cavity performance in the vertical test on the FRIB 0.53 HWRs.

Table 2.1: Statistics of the field limitation with all the cavity types, in FRIB production

Type	QWR-0.041	QWR-0.085	HWR-0.29	HWR-0.53
Total number of certificated cavities	16	106	72	148
1. Quench < B_p=85 mT	1 (0.6%)	0 (0%)	13 (18%)	2 (0.1%)
2. Field emission X-ray below B_p=85 mT	3 (19%)	41(39%)	21 (29%)	109 (74%)
3. Pure HFQS, including quench > B_p=85 mT	9 (56%)	26 (25%)	32 (44%)	21 (14%)
4. Suspicious HFQS X-ray onset > B_p=85 mT	3 (19%)	39 (37%)	6 (8%)	16 (11%)
HFQS total (3+4)	12 (75%)	65 (61%)	38 (53%)	37 (25%)

Four approaches were carried out in this project to resolve the issues mentioned above. The first approach resolves the Q drop issue. The second approach pushes up Q_0 performance. These two portions of the research were relatively easy, but left a large task ahead for future high Q cavity operation in cryomodules. Then, the program was challenged to develop higher effective transformative processing methods for high Q/G performance.

Table 2.2: Estimation of Q_0 at 8 MV/m from the FRIB 0.53HWR baseline data.

	R_{BCS}[nΩ]	R_{mg}[nΩ]	R_{other}[nΩ]	R_{LBT}[nΩ]	R_{res}[nΩ	R_S[nΩ]	Q_0* at 8 MV/m
Baseline (BCP)	1.6	2.8	2.8	0	5.6	7.2	1.5E+10
EP only	1.6	2.8	2.8	0	5.6	7.2	1.5E+10
EP + LTB	0.8	2.8	2.8	2	7.6	8.4	1.3E+10
EP + Magnetic shield	1.6	0.7 – 1.4	2.8	0	3.5 – 4.2	5.1 – 5.8	(2.1 - 1.9)E+10
EP + LTB + Magnetic shield	0.8	0.7 – 1.4	2.8	2	5.5 – 6.2	6.3 – 7.0	(1.7 – 1.5)E+10
CP with H_2O_2 + Cu	1.6	2.8	2.8	0	5.6	7.2	1.5E+10
CP with H_2O_2 + Cu, _+ Magnetic shield	0.8	0.7 – 1.4	2.8	0	3.5 – 4.2	5.1 – 5.8	(2.1 – 1.9)E+10
EP HNO_3 1500 ppm	0	2.8	2.8	0	5.6	7.6	1.9 E+10
EP HNO_3 1500 ppm + Magnetic shield	0	0.7 – 1.4	2.8	0	3.5 - 4.2	3.5 - 4.2	(3.1 – 2.6)E+10

*Q_0 = G/R_s, G=107.4 W for FRIB β = 0.53 HWRs

Solution 1: FE is a technical issue seen in surface cleaning. Better surface cleaning or smoothing of the surface can mitigate this issue. Electro-polishing (EP) can produce a smoother surface than that of BCP. The smooth surface produced by EP can make it easy to remove the particle contaminants, and result in mitigation of FE. On the other hand, HFQS is a performance issue inherent to cavities treated by BCP [2.3]. Post EP low temperature bake (LTB) (120 - 140 ^{O}C for 48 hours) post EP was developed to eliminate the HFQS in the 1.3 GHz ILC electro-polished cavities [2.3].

In this proposal, EP and EP + LTB are methods applied to the FRIB β = 0.53 HWRs. One concern with LTB is the additional surface resistance ($R_{LTB,}$ typically ~ 2 nΩ) generated by the LTB. This results in a benefit in using EP only, or EP+LTB, which was investigated, for high Q&G performance. These processes are expected to produce the cavity performance within the two dotted lines in Figure 2.2. This estimation is based on Table 2.2.

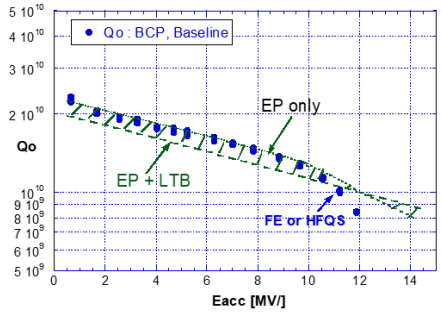

Figure 2.2: The cavity performance expected by electro-polishing and low temperature baking post EP. The blue solid circles are the typical FRIB β = 0.53 HWR performance produced by BCP. HFQS appears in the EP but FE is mitigated. EP + LTB eliminates the HFQS, but an additional surface resistance (R_{LTB}) by LTB appears as a result, and contributes to low Q_0 performance. This will reverse with the case of EP, but only at high gradient values.

Solution 2: When pushing up the Q/G performance of the FRIB HWR spare cryomodule cavities, the goal is to produce E_{acc} values of greater than 10 MV/m with a large enough Q value to keep heat dissipation below the limits of the current cryo system. The RF frequency of operation of FRIB HWRs is 322 MHz, and these cavities are operated at 2 K. At these conditions, the BCS surface resistance (R_{BCS}) is small enough that the residual surface resistance (R_{res}) dominates (see Table 2.2).

The second solution is to reduce the residual surface resistance, so that it pushes the Q_0 (unloaded Q) up. Magnetic flux trapping is thought to be a main contribution to residual surface resistance. An additional magnetic shield will be placed around the cavity during vertical testing. If the residual magnetic field could be reduced from the current value of 20 milligauss (mG) to around 5-10 mG, an improvement is Q_0 expected, as shown in Figure 2.3, using both the EP and EP + LTB methods. This method is viable for cryomodule production. HWRs in the spare cryomodule will have two layers of local magnetic shielding installed (present FRIB cryomodules use one layer of local magnetic shield).

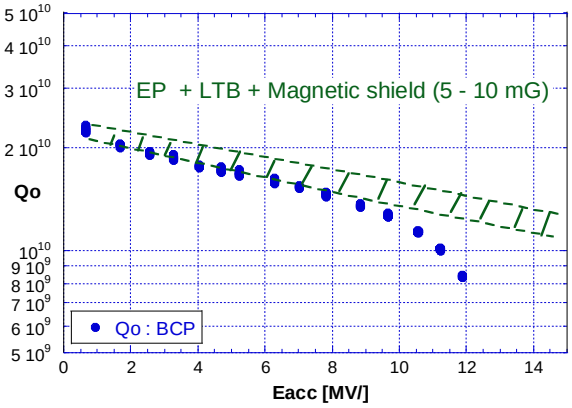

Figure 2.3: The expected magnetic shielding effect on the β = 0.53 HWR treated by EP+LBT. The performance is expected to be in between the top (5 mG) and the lower (10 mG) dotted lines.

Solution 3: The third solution is to develop the HFQS-free BCP, which is the validation of a new BCP using the recently developed CP acid mixture, initially developed as a part of a Michigan State University (MSU) PhD program [2.2]. This BCP is expected to produce HFQS-free performance, in combination with LTB. This includes an innovative concept of a copper catalyst in the BCP. The benefit of the simple preparation method of BCP as a solution is kept in the new method. This preparation method is expected to produce similar cavity performance as EP or EP+LTB in Figure 2.3, or Figure 2.4 when combined with the additional magnetic shield.

Solution 4: The fourth solution is to develop wet nitrogen doping to produce a high Q&G

performance. This is an innovative concept, and is preferable to the titanium helium jacketed cavities, like FRIB cavities. This method is similar to the first approach, but uses new EP acid, in which 1500 ppm of nitric acid (HNO_3) is added into the conventional EP acid. This recipe has the potential to provide nitrogen doping characteristics [6] with cavity performance, without 800 - 900 ^{O}C temperature annealing (wet nitrogen doping). This preprocessing is expected to produce the high Q&G performance seen in the dotted lines within Figure 2.4, by combination with magnetic shielding effect. Table 2.2 summarizes the estimated Qo based on the current BCP treated cavity performance of FRIB HWRs, for the above-mentioned approaches.

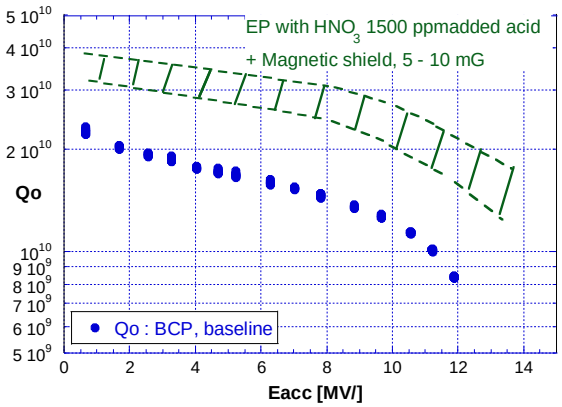

Figure 2.4: Expected high Q_0 and high gradient cavity performance (dotted line) by the fourth approach with additional magnetic shielding.

Objective-1 result: Electro-polishing, and Low temperature baking

FRIB's own EP facility was built in 2022 in the FRIB SRF High bay for future SRF development, collaborating with ANL. FRIB had completed the commissioning process by the end of December in 2022. This EP system was applied in bulk EP (to a depth of 120□m) on the SC 53-159 FRIB β = 0.53 HWR. In Figure 2.5 on the left, solid black squares show the result of the improved cavity performance by this EP process. The Q_0 achieved an increase in gradient performance up to 13 MV/m. Despite HFQS effects, Q_0 reached 1.0 x10^{10} at 10 MV/m. X-rays that would have been produced by FE were mitigated thanks to the smooth surface finishing by EP (Figure 2.5 on the right).

After this test, the cavity was baked in-situ at 120^{O}C for 48 hours, which is the so-called low temperature bake (LTB), and was subsequently cold tested. Figure 2.6 shows the surface resistance, which was measured at an E_{acc} value of 2.0 MV/m. This E_{acc} value was obtained using the formula in equation 2.1, of which Table 2.3 lists the results. Residual surface resistance improved from 5.9 nΩ (EP only) to 4.24nΩ (EP with LTB). Q_0 at E_{acc} = 10MV/m improved to 1.6x10^{10}. (Figure 2.5, on the left, shown in red diamonds). Though Q_0 had improved, it was still not high enough to reach the 12 MV/m operation goal, which required a Q_0 greater than 2x10^{10} to operate under the current FRIB cryoplant capability as shown in Figure 2.7.

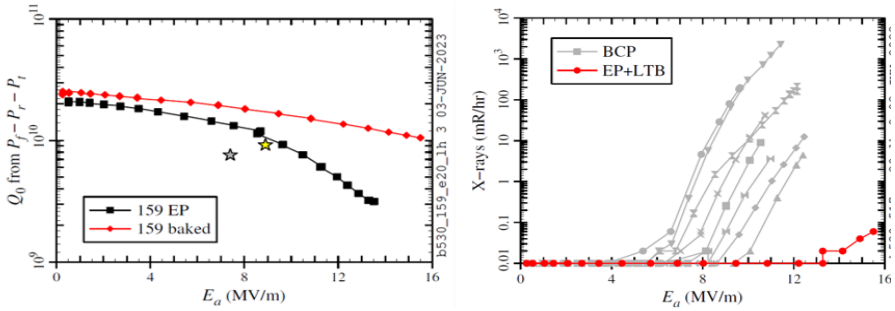

Figure 2.5: The left compares the Q_0 vs E_{acc} curve between EP and post EP + LTB at around 2K. The right compares the x-rays between the BCP treated FRIB production β = 0.53 HWRs and the electropolished β = 0.53 HWRs, each of which were low temperature baked in situ.

Objective-2 result: Local magnetic shield

To further increase Q_0, research to reduce residual surface resistance was performed. The cause of the high residual surface resistance is believed to be flux trapping from the ambient magnetic field in the Dewar. The current FRIB VT Dewar installed in the SRF High Bay has a global magnetic shield made of Mu-metal outside of the Dewar. Figure 2.8 shows the static ambient field measurement results in the Dewar at room temperature (RT). The specification of the static ambient field is less than 15 mG for FRIB production cavities. The measurement result was roughly 5 mG in the effective zone as shown in Figure 2.8. The residual surface resistance due to the static magnetic field is best represented by the following equation [1.29].

$$R_{mag} = 0.3[n\Omega] \times \sqrt{f[MHz]} H_{ext}[mG] \qquad (2.1).$$

Here, f is the cavity frequency. The frequency of the FRIB $\beta = 0.53$ HWR is 322 MHz. A residual resistance of 0.85 nΩ is expected at the ambient field of 5mG. If the ambient field reduces to zero, the expected Q_0 is 2.47×10^{10} at 2K at low field. The impact of the local magnetic shield looks small, but in objective 2 it was a necessary objective to reduce the ambient field in the VT Dewar as much as possible by using a local magnetic shield. The magnetic shield must have several holes for the RF ports, HPR rinsing ports, and the LHe inlet/exit ports. Effects of these features on magnetic field distribution were measured and compared to CST simulations. Results are detailed in Section 4.

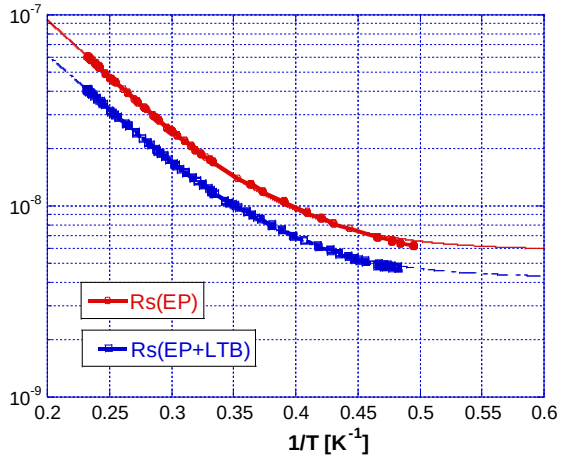

Figure 2.6: Result of data fitting with Rs vs 1/T using equation 2.1.

Table 2.3: Data fitting parameters in Fig. 2.6

	EP	EP+LTB
A [ΩK^{-1}]	2.14×10^{-5}	1.30×10^{-5}
D/k_B [K]	19.42	19.03
Rres [Ω]	5.90	4.24
R_{BCS} [Ω] at 4.3K	1.30	0.95
R_{BCS} [Ω] at 2K	0.65	0.42
Qo @ 2 MV/m @ 4.3K	1.49×10^9	2.07×10^9
Qo @ 2 MV/m @ 2K	1.64E+10	2.30×10^{10}

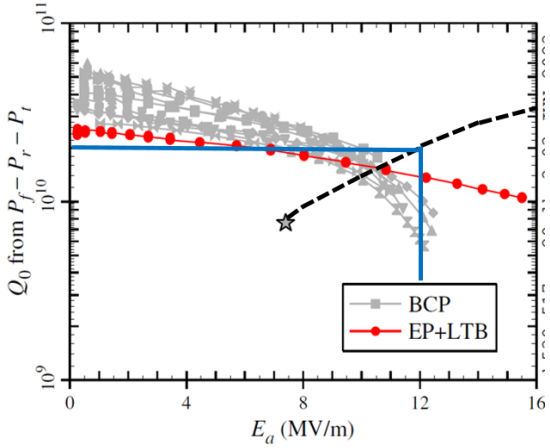

Figure 2.7: Comparison of Q_0 vs. Eacc curves of BCP and EP+LTB processed cavities. The dotted line is the Q_0 at a dissipation of 7.9 W, which is the current FRIB cryoplant capability.

The first study in objective 2 was to test a local magnetic shield's impact on the cavity performance, as seen in Figure 2.9. The results are shown in Figures 2.10 and 2.11. The local magnetic shield improved the residual magnetic field at E_{acc} = 2.0 MV/m by a small margin. It improved resistance from 4.24nΩ to 4.17nΩ, and Q_0 from 1.4E+10 to 1.5E+10 at 10 MV/m at an operating temperature of 2K, but was not enough to push the Q_0 to the high accelerating gradient operation point desired, for example, improving Q_0 to greater than 2E+10 at an E_{acc} value of 12 MV/m.

Objective 2-2 result: Uniform cooling and active field cancellation

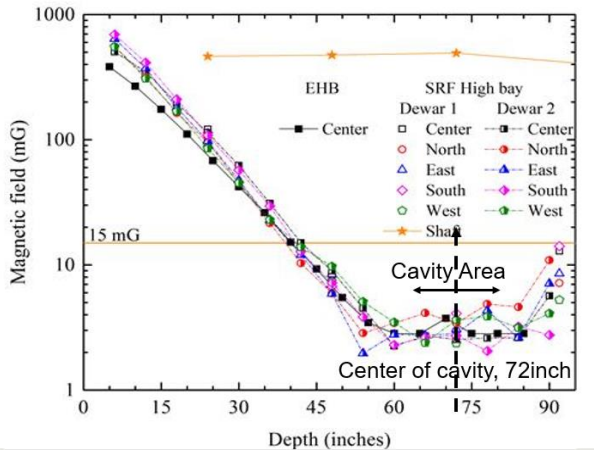

Figure 2.8: Static ambient magnetic field in a FRIB VT Dewar

Figure 2.9: Local magnetic shield covering a FRIB 0.53HWR

The limited effect of the shield on improving Q_0 indicates that the static ambient magnetic fields are not the main causes of residual resistance. Instead, the dynamic ambient magnetic field due to the thermoelectric current effect is the proposed cause of the residual resistance. FRIB cavities have several different material joints near the cavity, such as Nb/NbTi, Ti/Nb, and Ti/SS (titanium/stainless steel). These joints can generate Seebeck electric voltages if the cooling temperature is not uniform across the metal

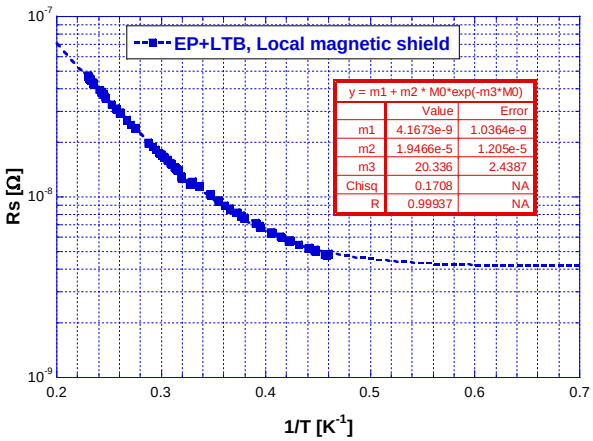

Figure 2.10: Effect of the local magnetic shield on residual surface resistance

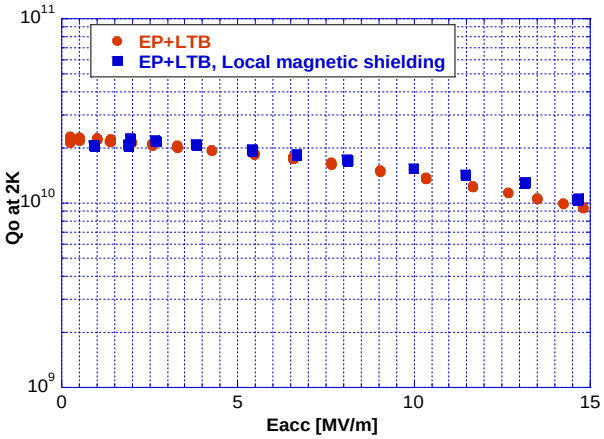

Figure 2.11: Effect of the local magnetic field on Q_0 vs E_{acc}

junctions. If Seebeck voltage generated by the temperature difference produce a thermocurrent, the cavity might trap the magnetic field produced by this thermocurrent at the superconducting critical temperature of the niobium (T_c = 9.25K), during cool down. The cause of the residual resistance aforementioned might be the flux generated by the thermoelectric current, trapped inside of the shield.

Distribution of flux gauge and temperature sensor

To monitor the magnetic flux and temperature during cool down, as shown in Figure 2.12, three flux gauges were distributed; one is at the bottom, outside the magnetic shield. The other two are on the bottom and top inside the magnetic shield. Six temperature sensors were distributed as shown in Figure 2.12 by black circles. The one in the center is simply on the beam port flange.

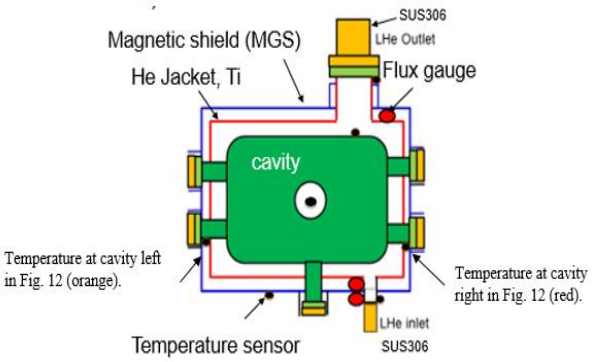

Figure 2.12: The LMGS is placed outside of the helium jacket to embrace the entire setup. Flux gauges and temperatures are installed as shown.

Uniform cooling method

The method of uniform cooldown was performed using the liquid helium inlet valve, watching the cavity temperature: when the cavity temperature decreased below 10K, the valve was closed, and then time was given to allow the temperature to warm up to an temperature on the order of 10s of Kelvin (30 K, 20 K, etc.), then the valve was opened again. This valve operation was repeated more than 10 times, with the temperature gradually increasing close to 10K, where the valve was then opened to collect liquid helium in the Dewar. Thus, the temperature difference during cooldown was kept around the value of 10K. The cavity was cooled down using this method, while observation of these sensors was performed, allowing close observation of the cool down, to make sure the cavity cooled as uniformly as possible. The output signals of these sensors are shown in Figure 2.13, which compare the uniform cooldown (Figure 2.13 right) and the conventional cooldown (Figure 2.13, left, fast cooldown) used during FRIB production cavity testing.

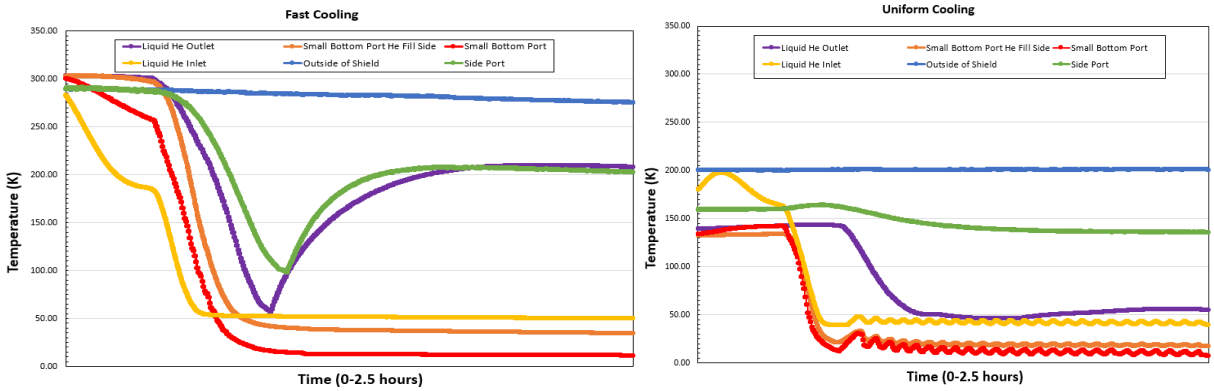

Figure 2.13: Trace of cavity cool down. The left is fast cooldown (normal cooldown), and the right is uniform cooldown.

The output signals from the flux gauges inside the magnetic shield are shown in Figure 2.14. The flux at around Tc reduces to ~ 6mG by the uniform cooldown method, while the fast cooldown

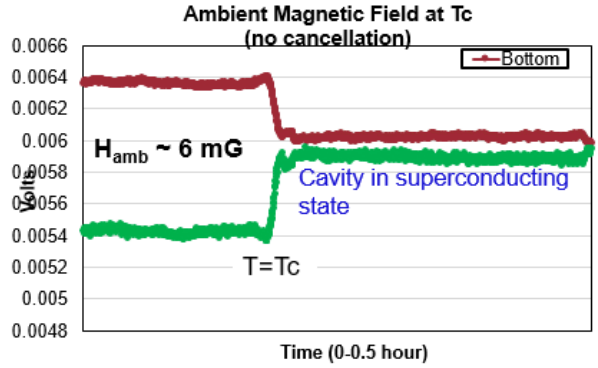

Figure 2.14: Ambient field during uniform cool down (left) and active field cancellation during uniform cool down (right)

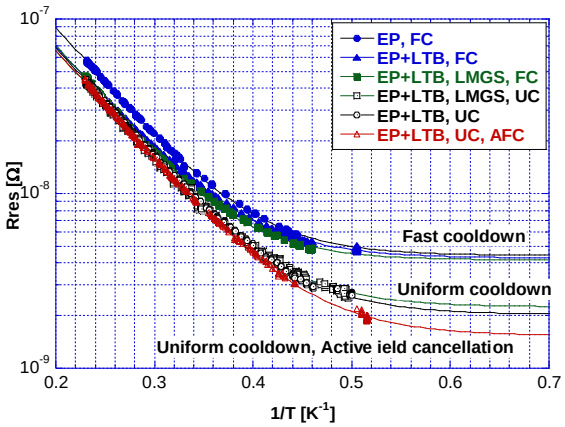

Figure 2.15: Impact of uniform cool down on the residual surface resistance.

case was reduced to ~ 18mG (not pictured in Figure 2.14).

Results of uniform cooldown with/without magnetic shield

The effect of the uniform cool down method on the residual surface resistance is shown in Figure 2.15 for with/without a local magnetic shield. For both cases, the uniform cool down reduced the residual surface resistance from 4.3 nΩ (fast cool down) to ~ 2.0 nΩ. Figure 2.16 shows the Q_0 vs E_{acc} curves at 2K for each case. Compared to the case of fast cool down, both have an improved Q_0 performance value, from 1.7 x 10^{10} to 2.3 x 10^{10} at 10 MV/m. One such result is a Q_0 value of 2x10^{10} at 12 MV/m.

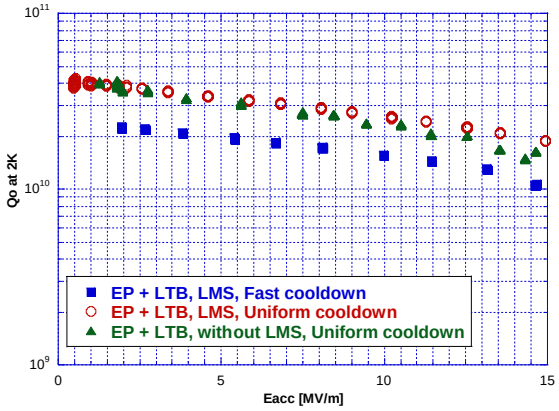

Figure 2.16: Impact of the uniform cool down. A large impact by the uniform cooldown method was observed.

Result of active field cancellation method

The uniform cool down method appears to be effective, but this method cannot cancel the static ambient fields like the residual magnetic field produced by the earth in the Dewar. To cancel the residual static ambient field after uniform cool down, active field cancellation using a Helmholtz coil at the top and bottom of the Dewar was performed. As seen in Figure 2.17, the residual magnetic field was reduced by around 3mG using this method. The residual surface resistance reduced by up to 1.3nΩ as well, as seen in Figure 2.15. The cavity performance was also improved, as shown in Figure 2.18. The Q_0 at an E_{acc} value of 12 MV/m improved to 3x10^{10} at the same Eacc value.

Figure 2.19 shows the relationship between the strength of the ambient magnetic field and the resultant residual surface field. Even if the ambient field is zero, a residual surface resistance of 1nΩ will remain, which does not have an explanation at this stage of development. The residual

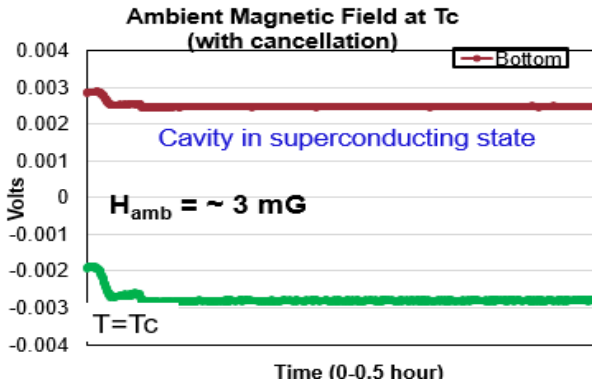

Figure 2.17: Impact of active field cancellation on the residual magnetic field in the Dewar.

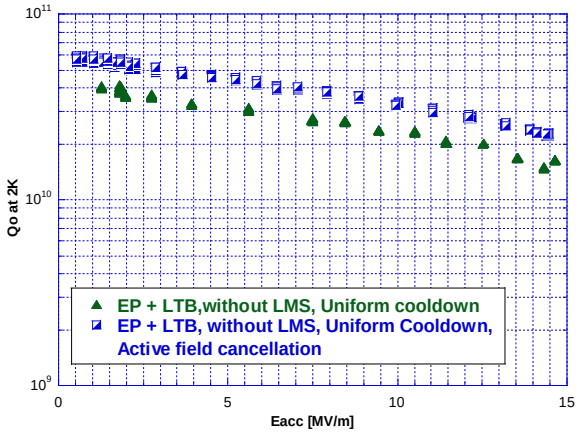

Figure 2.18: Impact of active field cancellation on the cavity performance.

surface resistance with just EP+LTB is 4.24 nΩ as seen in Table 2.3. It was found that about 80% of the residual surface resistance is caused by the ambient field, mainly induced from the thermoelectric current as generated by the Seebeck effect. Therefore, it is a high priority to resolve this issue in order to push up Q_0 performance values.

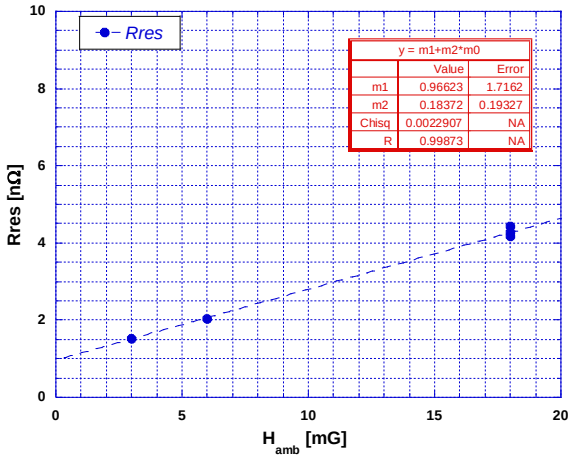

Figure 2.19 – The relationship between the strength of the ambient magnetic field, and the residual surface field

2.3 Motivation for this thesis

The above results give a strong sense of motivation for this thesis. It was learned that resolving the thermoelectric current issue is the highest priority to improve the Q_0 performance. The final goal is to realize a high Q and high accelerating gradient cavity performance in a real cryomodule. The local magnetic shield is an applicable method for use in the cryomodule, however the uniform cooling method developed here carries an innate risk for application to real cryomodules with a large heat capacity. The refrigerator installed in the FRIB High bay has a cooling capacity of only 600W, and can handle the cool down of the cavity with some flexibility. In contrast, a large-scale SRF accelerator project uses a liquid helium refrigerator with a cooling capacity greater than 5 KW. Such a cryoplant has a huge heat capacity, and it is not easy to perform a uniform cool down, as developed here. As such, a resolution to the thermoelectric current issue using a method that

will not overload the cryoplant's cooling capacity is needed.

To mitigate the thermoelectric current, it is necessary to develop a more realistic method. Even if Seebeck voltage is generated, its current does not flow if the thermoelectric circuit opens, and as a result, no flux is produced. It is more likely that the issue of a generated thermocurrent will be solved by inserting an insulator in the circuit (cooling path), using coating technologies. If this succeeds, it will mean a great contribution to third generation SRF accelerators. However, prior to such development, it is necessary to understand the characteristics of the thermocurrent itself, i.e. the Seebeck effect from the cryomodule production point of view. It is necessary to further study the Seebeck effect and the resultant thermoelectric current, especially for the different material joints Nb/NbTi, Ti/SS, Al/Cu and so on, which are often used in cryomodule construction. The motivation to investigate the characteristics of the Seebeck effect and thermoelectric currents for such material joints culminated in the design and fabrication of the measurement system described in this thesis. Description of the Seebeck effect takes place in Chapter 5, the system of measurement and results in Chapter 6, and the discussion of said results in Chapter 7.

When the issue of thermoelectric current has been resolved, the static ambient magnetic field issue will remain. This is due to an insufficient shielding of the cavity from earth's magnetic field, and magnetized materials in the cryomodule. Even stainless steel nuts or bolts are prone to magnetization by stress during fabrication or user operation. The local magnetic shield is thought to be the best way to reduce the produced static ambient field in the cryomodule. The impact of the local magnetic shield was not satisfactory, as seen by the results of objective two, but they should be considered in regards to later sections of this thesis. The local magnetic shield fabrication in objective two provided a great opportunity to study the relationship between the port size and the needed sleeve length to avoid field penetration in future shield designs. The study's results on the local magnetic shield of objective two lie in Chapter 4.

Bibliography:

[2.1] C. Zhong, et al., “Certification Testing of Production Superconducting Quarter-wave and Half-wave resonators for FRIB”, Nuclear Inst. and Methods in Physics Research A1014 (2021) 165675. https://www.sciencedirect.com/science/article/pii/S0168900221006604

[2.2] D. Luo and K. Saito, “Discovery of Copper Catalyst for New Chemical Polishing Acid on Superconducting Niobium”, https://arxiv.org/pdf/2001.02086

[2.3] D. Luo, K. Saito and S. Shanab, “Nitrogen Contamination Causes High Field Q-Slope (HFQS) in Buffered Chemical Polished SRF Cavities”. https://doi.org/10.48550/arXiv.1904.00145

3. RF loss mechanisms caused by ambient magnetic fields

The major focus of this thesis is the RF loss in superconducting cavities due to the ambient magnetic field. The understanding of the RF dissipation mechanism caused by the ambient magnetic field is paramount. In this section, the mechanisms are explained. The mechanism consists of three regimes: 1) the static ambient field (fluxoid) not moved by the RF field, 2) forced oscillation of the trapped fluxoid by the RF field, and 3) RF heating at weak-kink boundaries caused by trapped flux. The first one is explained in the Padamsee textbook [1.29]. A summary of this first cause comes first. The second and third ones are rather complicated, but the essential details are explained in the following pages.

3.1 RF dissipation by static ambient fields

Shown in Fig. 3.1, this model describes the process of RF dissipation, which is the RF current flowing through the flux trapped core area where there is a normal conduction due to the flux trapping. The RF dissipation due to flux trapping has the representation

$$A * H_{ext} = N * \Phi_o \tag{3.1}$$

where Φ_o is the quantum flux = h/(2e) = 2.067x10^{-16} Wb, A is the area of trapped flux, N is the number of quantum fluxoids, H_{ext} is the strength of the ambient magnetic field. The contribution to the residual resistance from N fluxoids is the normal state resistance R_n multiplied by the fraction of the normal-conducting area. Here, the full trapping effect is

$$\mathrm{R_{mag}} = N\frac{\pi\xi_0^2}{A}R_n = \frac{H_{ext}\pi\xi_0^2}{\phi_0}\,R_n \tag{3.2}$$

The upper critical field of Type-II superconductors is defined by:

$$\mathrm{Hc2} = \frac{\phi_0}{2\pi\mu_0\xi_0^2} \tag{3.3}$$

Therefore

$$\mathrm{R_{mag}} = \frac{H_{ext}}{2H_{C2}}R_n \tag{3.4}$$

Where $R_n = \sqrt{\frac{\mu_0\omega}{2\sigma}}$ and

$$R_{mag} = \frac{H_{ext}}{H_{C2}}\sqrt{\frac{\mu_0\omega}{8\sigma}} \tag{3.5}$$

R_{mag} is written as

$$R_{mag} = 0.3[n\Omega] * \sqrt{f[GHz]}H_{ext}[mG] \tag{3.6}$$

For FRIB 322 MHz,

$$R_{mag} = 0.17 * H_{ext}[mG] \tag{3.7}$$

namely, for 322 MHz niobium SRF cavities, the residual surface resistance of 0.85nΩ/mG occurs due to the ambient magnetic field. This value is close to the result given in Table 2.3 for H_{ext} =5mG.

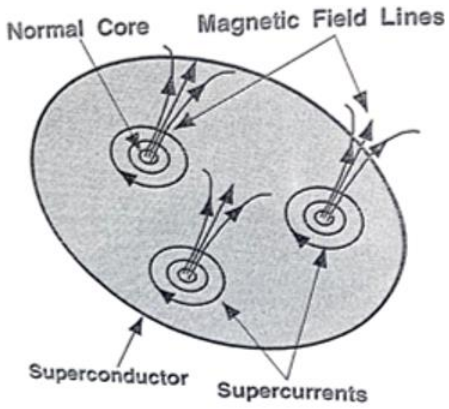

Figure 3.1 – RF dissipation generated by static flux trapping [1.29]

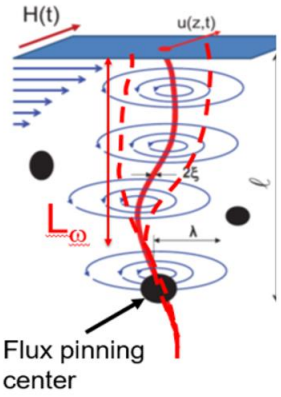

Figure 3.2 – Flux oscillations generated by the RF field [3.1]

3.2 RF dissipation by flux oscillation

Figures 3.1, and 3.2 are as follows: when the RF magnetic field (H_p) is exposed on the SRF surface, the superconductor produces a super-current to shield the field, and then this super-current interacts with the vortex line pinned at defects or contaminations in the metal, and is forced to oscillate through the Lorentz force (F_L). $F_L \times u$ (the displacement of the flux line) is the dissipation energy. The F_L is proportional to H_p, and the displacement, therefore the dissipation is proportional to H_p^2, which follows with

$$P = \frac{1}{2} R_i \left(\frac{B_o}{\Phi_o}\right) H_p^2 \tag{3.8}$$

And

$$R_i = \frac{B_o}{B_c} \sqrt{\frac{\mu_o \rho_n \omega}{2g}} \tag{3.9}$$

Here, B_o/ϕ_o is the number of flux lines in a bundle within the vortex; ρ_n is the resistivity of a normal conductor, with 2g = 1 clean Nb surface. The dissipation depends on the RF frequency ($\omega = 2\pi f$) as $\sqrt{\omega}$.

This gives the same result with model 3.1 but is larger by a factor of two. For 322 MHz FRIB HWRs,

$$R_i = 0.34B_o \tag{3.10}$$

The residual surface resistance of 1.7nΩ at B_o =5mG is expected for FRIB β = 0.53 HWRs. This value is smaller than that of the results in Table 2.1.

The vortex oscillation model (Figure 3.2) [3.3], while similar, gives another formula. A simple calculation gives

$$P_i = \frac{4\omega}{3\mu_0^2}\frac{\lambda^2}{j_d c(k)}B_{rf}^3 \tag{3.11}$$

$$R_i = \frac{8\omega}{3\mu_0^2}\frac{\lambda^2}{j_d c(k)}B_{rf} \tag{3.12}$$

$$c(\kappa) \approx ln(k) + 0.5 + e^{\left[-0.4-0.8\ln(k)-0.1\,(ln(k))^2\right]} \tag{3.13}$$

This derivation shows that the surface resistance is proportional to the RF magnetic field, and ω. For clean N_b, κ=1, c(κ) = 1.17, λ= 40nm, j_d=8x10^{11} A/m^2, and μ_o= 1.257x10^{-6}, with

$$R_i = \ 2.89 \times 10^{-16}\omega B_{rf} \tag{3.14}$$

For 322MHz FRIB HWRs (B_p/E_{acc} = 8.41),

$$R_i = \ 5.84 \times 10^{-7}B_{rf}[T] = 4.91 \times 10^{-8}\ E_{acc}\left[\frac{MV}{m}\right] \tag{3.15}$$

This value is greater by several orders of magnitude compared to the result [3.4], for BCP treated FRIB 0.53 HWR, which is:

$$R_i = \ 1.87 \times 10^{-10}\ E_{acc}\left[\frac{MV}{m}\right] \tag{3.16}$$

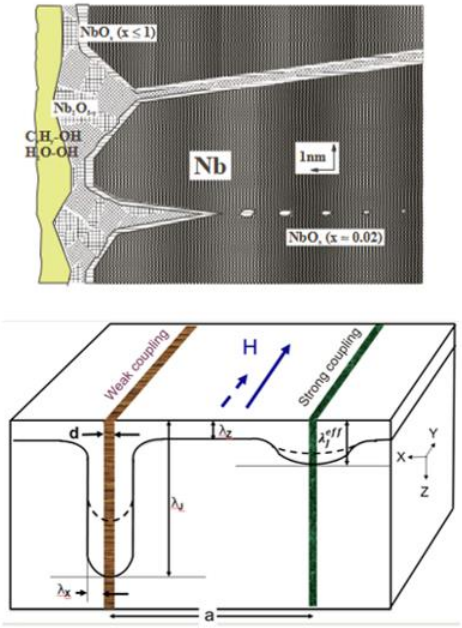

Figure 3.3 – Weak link or strong links shown at grain boundaries. The figure on top shows the insulation between grains [3.7]. The figure on the bottom is an illustration of the weak link or strong link interactions [3.8]

3.3 RF dissipation on Josephson junctions

Another source of trapped flux dissipation is the presence of hysteresis losses due to a Josephson fluxoid at "weak-link" locations or "strong-link" locations. The niobium material has a grain structure shown in Figure 3.3, at the top. As seen in Figure 3.3, at the bottom, in some cases, insulator materials (more than likely being niobium oxide) are sandwiched between grains. These grains can be weakly coupled (meaning a thicker insulator), which are called weak-links, or strongly coupled (meaning a thinner insulator) which are called strong-links. This SIS structure produces something known as a Josephson element. When the flux (fluxons) are trapped in the Josephson junction, and the RF field irradiates the fluxons, they are forced to oscillate, and in doing so, generate loss for the cavity. The resultant surface resistance has a hysteresis defined by the RF cycles [3.5], as seen in Figure 3.4. This surface resistance is linearly proportional to the RF field [3.6].

$$R_{hys}(B_p) = \frac{4}{3\pi}\frac{\omega}{2J_{cJ}[1+(\frac{\omega}{\omega_0})^2]^{\frac{3}{2}}}\frac{2\lambda}{a_J}B_C\left(\frac{B_p}{B_C}\right) = R^1_{res}\left(\frac{B_p}{B_c}\right) \tag{3.17}$$

For 1.5GHz cavities, the parameters are estimated to be a_j ~ 100nm, J_{CJ} ~ $8x10^{11}$ A/cm^2, ω_0 ~ 0.06GHz [3.6], and B_c = 200m. A comparison between experimental results and theoretical estimates for the hysteresis surface resistances at 2K is shown in …. FRIB 322MHz parameters are listed in Table 3.1. A difference close to an order of magnitude in size can be seen between the theoretical and experimental results.

Table 3.1: Hysteresis surface resistance

1.467 GHz Cavity	Before baking (BCP)	After 100-120^{O}C baking
R^1_{res}/B_c [Ω/mT], B_c=200mT	$5.50x10^{-11}$	$1.01x10^{-10}$
Theoretical estimate	$6.55x10^{-10}$	$1.00x10^{-9}$
322MHz FRIB HWER	2.22×10^{-11}	

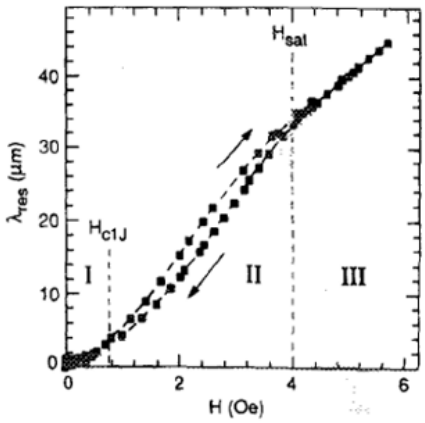

Figure 3.4 – High field effects on the penetration depth at 85 K with high temperature superconductors, which are displayed as λ_{res} (~ R_{hys}) vs B. Note that the hysteresis due to the flux inclusion at modest field values. Regime II is the hysteric surface resistance [3.5]

Bibliography:

[3.1] A. Gurevich, “Dissipation caused by oscillating vortices in the SRF cavities”, TTC meeting, CERN, Nov. 8-9, 2018. https://conference-indico.kek.jp/event/298/https://indico.cern.ch/event/741615/contributions/3180378/attachments/1749680/2834393/Gurevich_TESLA_vort.pdf

[3.2] A. Gurevich and G. Ciovati, “Effect pf vortex hotspots on the radio-frequency surface resistance of superconductors”, Phys. Rev. B87.054502 (20130). https://journals.aps.org/prb/pdf/10.1103/PhysRevB.92.134501

[3.3] D. B. Liarte, et al., “Vortex Dynamics and Losses Due to Pinning: Dissipation from Trapped Magnetic Flux Resonant Superconducting Radio-Frequency Cavities”, Phys. Rev. App. 10, 054057 (2018), https://journals.aps.org/prapplied/pdf/10.1103/PhysRevApplied.10.054057

[3.4] Y. Wu, “Development of Wet Nitrogen Doping to Enhance Q Performance of β=0.53 Half-wave Resonators”, TTC High Q and High Gradient Virtual meeting, Sep. 12, 2024. https://conference-indico.kek.jp/event/298/timetable/#20240912

[3.5] J. Halbritter, “RF residual losses, surface impedance, and granularity in superconducting cuprates”, J. Appl. Phys., 68(12), 15 December 1990. https://doi.org/10.1063/1.346875

[3.6] G. Ciovati and J. Halbritter, “Analysis of the Medium Field Q-Slope in Superconducting Cavities Made of Bulk Niobium”, Proc. of the 12th International Workshop on RF Superconductivity (SRF2005), Cornell University, Ithaca, New York, USA. 2005. pp. 230-235. https://accelconf.web.cern.ch/SRF2005/papers/tup02.pdf

[3.7] J. Halbritter, “Material Science of Nb RF Accelerator Cavity: Where Do We Stand 2001?” Proc. of the 10th Workshop on RF Superconductivity, 2001, Tsukuba, Japan. https://accelconf.web.cern.ch/srf01/papers/ma006.pdf

[3.8] J. Halbritter, “Granular Superconducting and Their Intrinsic and Extrinsic Surface Impedance”, Journal of Superconductivity”, Vol. 8, No 6, 1995, pp. 697. https://link.springer.com/content/pdf/10.1007/bf00727492.pdf

4. Local magnetic shield

The Dewars used for FRIB SRF cavity testing use a global magnetic shield to reduce the ambient field to 5 milligauss (mG) at the cavity zone in the Dewars. To reduce the ambient field to less than 0.1 mG, a local magnetic shield (LMS) was fabricated so that it surrounded the cavity, as mentioned in Chapter 2. The LMS was made of Permalloy [4.1]. The structure of the LMS is cylindrical in its base geometry, as can be seen in Fig. 4.1. This LMS was designed to reduce the static ambient field to < 0.1 milliGauss in the effective zone. When in use, the LMS is fastened on the outside of the helium jacket using mechanical fixings.

Fig. 4.2 shows the assembly of the shield in simulation, and as fabricated. The LMS has ten holes in total: the RF input/pickup port, two Beam line ports, two ports for cavity support, two high-pressure water rinsing ports, and liquid helium in/out ports. The biggest design challenge was the penetration of the ambient magnetic field through these holes. Considering these issues, sleeves were placed on them as seen in Fig. 4.2 on the left. A real example is shown in Fig.4.2 on the right.

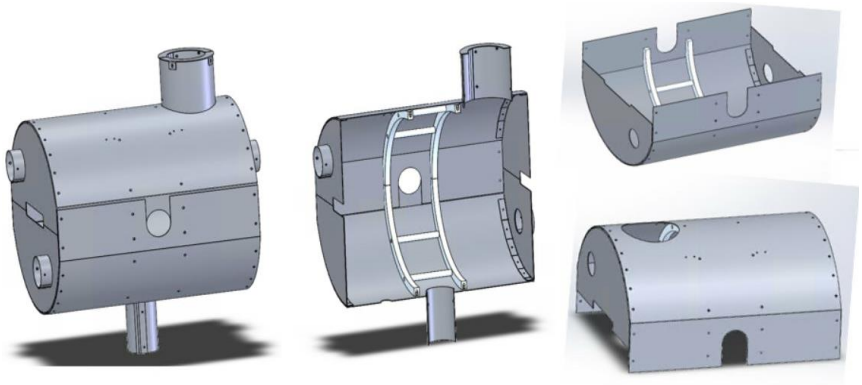

Figure 4.1: The structure of the local magnetic shield fabricated as part of objective two in the grants admitted by the DOE.

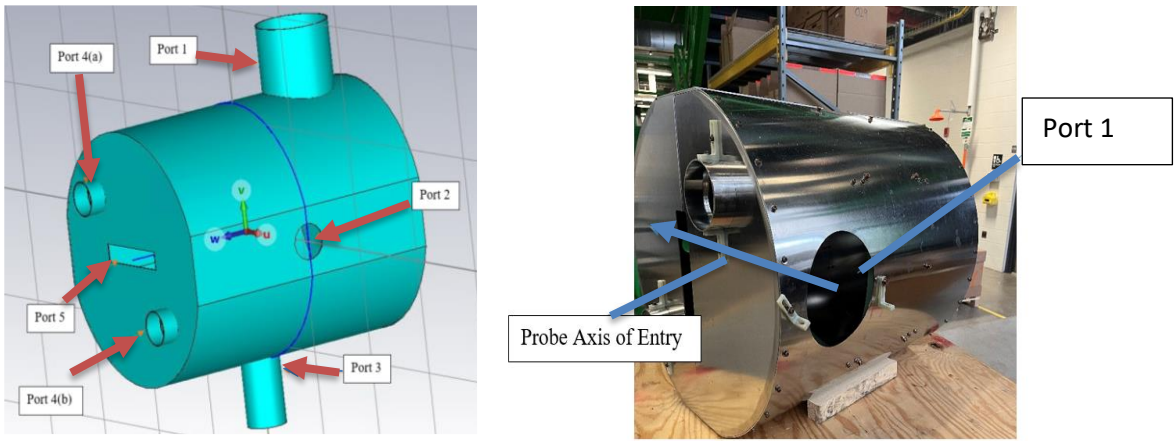

Figure 4.2: The assembled LMS. The figure on the left shows the simulated design, and on the right is the fabricated version.

The magnetic field surrounding the LMS was measured to assure its effectiveness. In this measurement, the interest was in the relationship between the diameter of hole vs. field penetration depth, and sleeve length vs. field penetration depth. The motivation behind this being that, if a general guideline on sleeve length, port diameter, and penetration depth were found, a

recommendation as to how long sleeves could be made for what hole size could be made, making future designs easier. To find this guideline, measurements of the field penetration were made, and compared to simulations of the penetrating magnetic field using CST Studio Suite (for more information on the program, please see the manufacturer's website.)

4.1 Ambient field measurement method with LMS

The shield was measured down each port's axis as shown in Figure 4.2. The model of flux probe used in these measurements is the MMZ-2508-UH Lake Shore gauss meter probe. At first, the magnetic field measurements were offset by the background magnetic field inside of the room. The shield was secured in place, and the probe was calibrated using a zero gauss chamber so as to remove the offset, and achieve an accurate reading inside of the shield.

Figure 4.3 – Magnetic shield measurement environment

(The setup here was used because the shield needed to be secured in place, while the measurement apparatus moved around the shield to measure the other ports. Bulk metal was avoided by using plastic carts, and the only metal used was aluminum (non-ferromagnetic). Wooden blocks were used to prop the sensor and probe so as to not disturb the magnetic field.)

4.2 Measurement results without sleeves

Each port was measured along the axis, both with and without the sleeves, running along the cavity an inch at a time, and taking measurements at every increment. The results of the measurements are in Figures 4.4 and 4.5 (Port 1, the liquid helium exit port), 4.6 (Port 2, the beam line port), 4.7 (Port 3, the RF input coupler port), 4.8 (Port 4(a), the rinsing port), and 4.9 (Port 5, the cavity support slot). Four HPR rinsing ports (port 4(a)-(d)) had similar results compared with each other through the simulation data (see 3.3.4), so only one port , 4(a), was measured. Two others ports (Port 2 (a)-(b), port 5(a)-(b)) are also measured in this way, due to their mirrored symmetry about the shield. The LHe inlet port, as shown on the opposite side of Port 1, was not measured due to its small size, which the probe could not easily fit through. These measurements were performed in FRIB's East Highbay, which has a varying magnetic field background every day. There was not a proper location to perform the experiment that would accurately depict the conditions inside of

the Dewar without background fields present. To clarify, the importance of these measurements is to obtain relative magnitude instead of the absolute field within the shield. A measurement made relative to the background magnetic field shows the magnitude of the field inside of the shield when the background is measured, and accounted for.

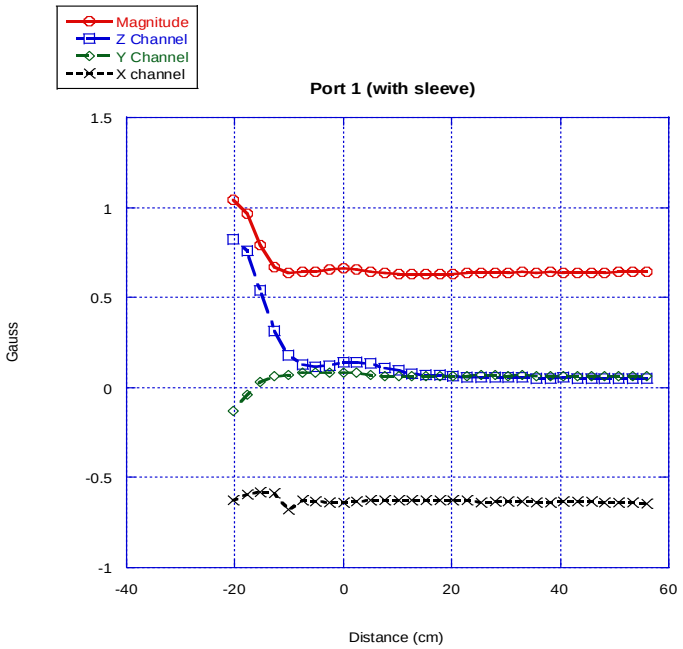

Figure 4.4: The measurements taken with a sleeve on Port 1 (LHe exit port)

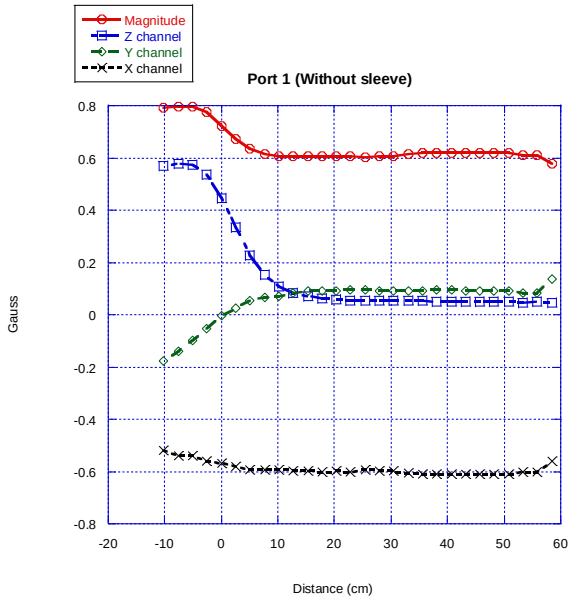

Figure 4.5: The measurements taken without a sleeve on Port 1 (LHe exit port)

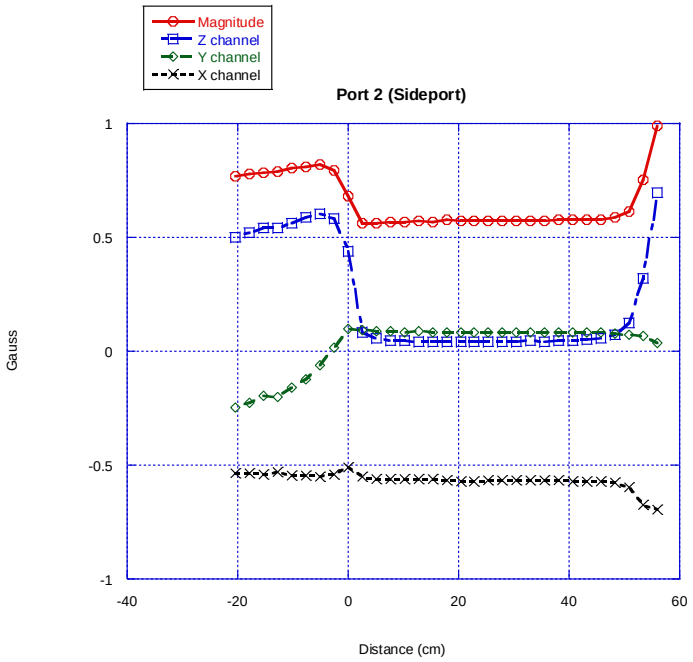

Figure 4.6: The data from port 2 (beam line port) without the sleeve.

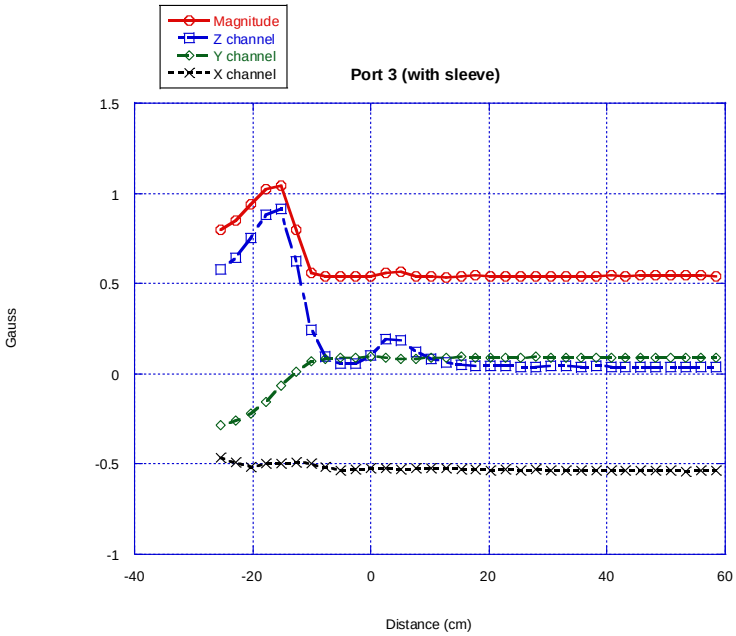

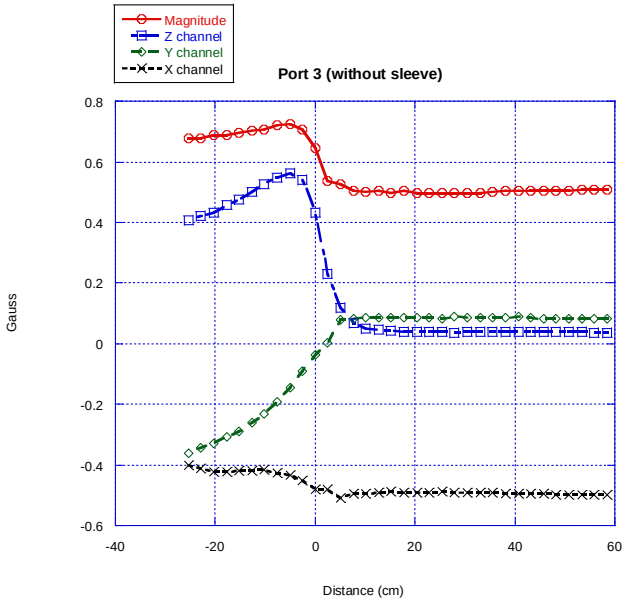

Figure 4.7: Port 3 (input coupler port) data for without/with sleeve. Top for with sleeve, and bottom for without sleeve.

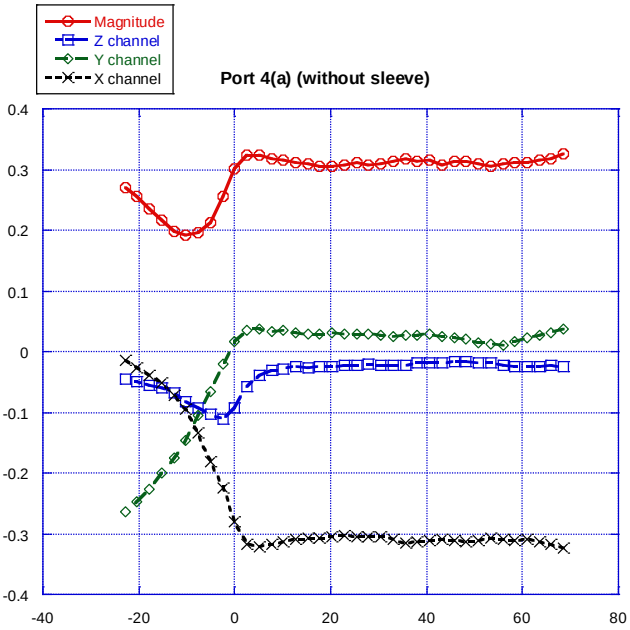

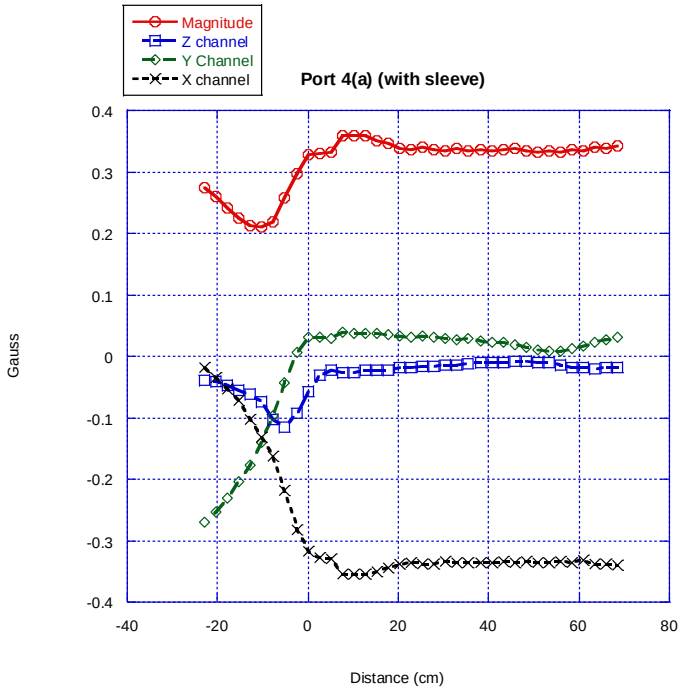

Figure 4.8: Port 4a (HPR rinsing port) data for without/with sleeve. Top for without sleeve and bottom for with sleeve.

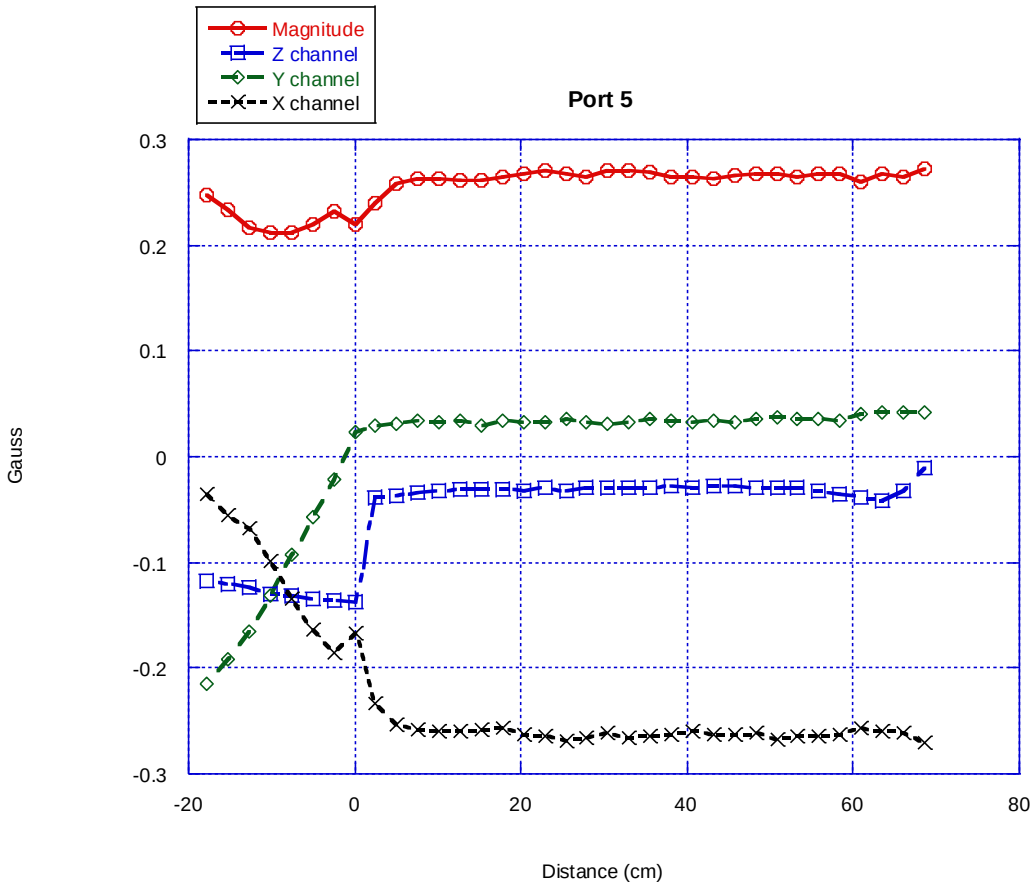

Figure 4.9: Port 5(a) (cavity support port) ambient magnetic field data is graphed here.

4.3 Measurement results with sleeves

The sleeves were then reattached for Port 1, Port 3, and Port 4(a). The measurement results for these ports, with the sleeves attached, are listed above, and labeled appropriately. It was noticed that the sleeves had a marked impact on the field penetration depth, which was expected from the simulation results.

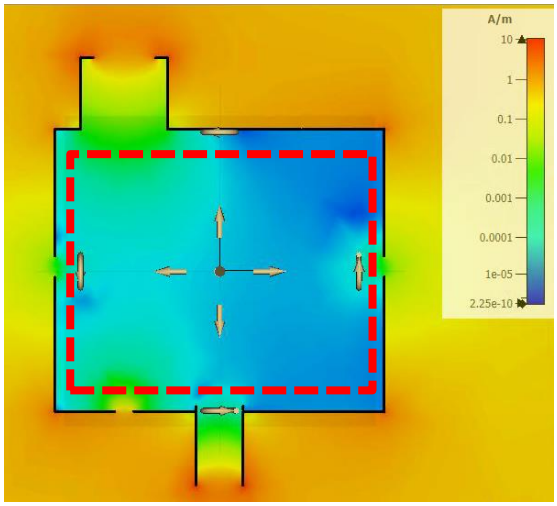

Figure 4.10: Simulation of the field distribution about the local magnetic shield. The dotted box outlines the cavity area.

4.4 Simulation of the magnetic distribution

A software package known as CST studio [3.2] was used to model the overall field distribution in the LMS. All of these geometries and design choices are reflected in the 3D simulation. The applied field was -39.789 A/m, which is roughly 500mG. The configuration is the same as the VTA Dewar with global magnetic shield. The simulation result is shown in Fig. 4.10. The maximum strength of the ambient field is 0.008 A/m (0.1mGauss) nearby the LHe inlet port on the bottom (the small hole). Other cavity zones have a field measured well below 0.1mG.

Detailed simulations were carried out to analyze the effect of a sleeve on each port, using CST studio, which allowed simulation of the penetration depth of the magnetic field. Fig, 4.11 shows an example of these analysis results, with Port 1 (sleeve length = 167.6 mm), the LHe outlet port, which has the biggest impact on the interior magnetic field distribution. This figure assumes an ambient field strength of 500 mG = 39.79 A/m (Earth's magnetic field) in the vertical direction. The figure graphs the normalized distance versus the magnetic field, with the normalized distance being the distance into the shield divided by the diameter of the port it enters through. The penetration depth is shortened from 1.57 to 1.06 in the normalized unit ($L_{penetrate}/D$), when the sleeve is placed on the port. The effective zone extends due to the shorter field penetration depth.

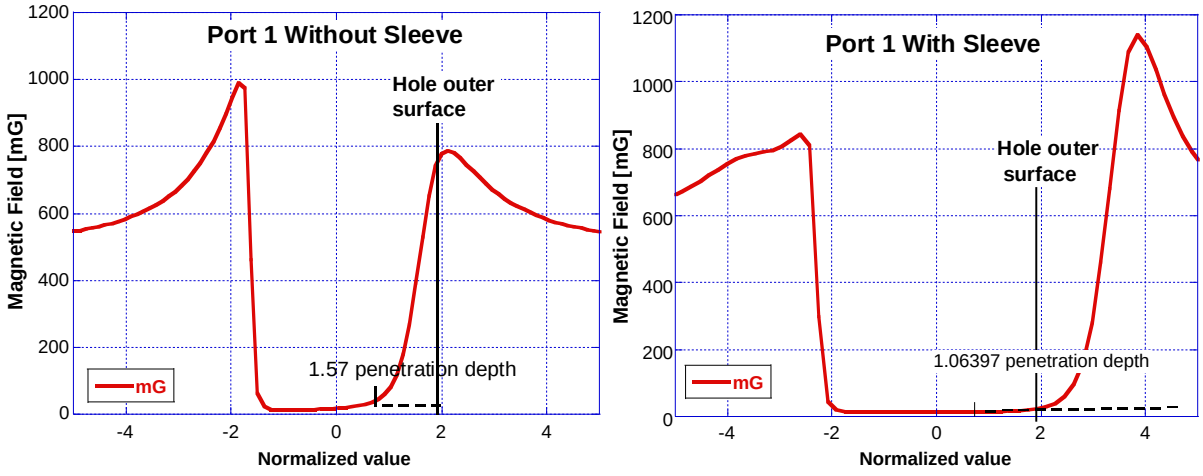

Figure 4.11: Port 1 with the sleeve attached (left), simulated with an ambient magnetic field of 500milliGauss. Right for without sleeve.

4.5 Discussion about magnetic field shielding

Table 4.1, 4.2 and 4.3 list the field penetration depth without/with sleeves. These results are shown in Fig. 4.12, and 4.13 to compare the simulation and measured results of all ports, on each axis. The length of each port's sleeve is as follows: Port one has a sleeve that is 167.7 mm in length, Port three has a sleeve that is 165 mm in length, and Port four has a sleeve that is 40.05 mm in length. As a conclusion for this section, it is the personal recommendation of this researcher that a sleeve be used that has a length of at least 100 mm.

Table 4.1: Field penetration depth dependence on the hole diameter (X axis)

Simulation results					
Port	Diameter (cm)	Field Penetration depth without sleeve (cm)	Normalized field penetration depth without sleeve	Field penetration depth with sleeve (cm)	Normalized field penetration depth with sleeve
Port 1	17.73	16.21	0.9143	13.09	0.738
Port 2	8.255	1.674	0.203	3.46	0.42
Port 3	10.145	10.8	1.0646	2.94	0.29
Port 4(a)	7.595	4.45	0.586	4.91	0.646
Port 5	4.225 (width), 20.965 (height)	5.565	1.32	9.162	2.168
Measurement results					
Port 1	17.73	12.7	0.7163	7.62	0.4298
Port 2	8.255	2.54	0.308	2.54 (No sleeve)	0.308
Port 3	10.145	5.08	0.5	-5.08	-0.5
Port 4(a)	7.595	2.54	0.3344	7.62	1.0033
Port 5	4.225 (width), 20.965 (height)	5.08	1.2	5.08 (No sleeve)	1.2

Table 4.2: Field penetration depth dependence on the hole diameter (Y axis)

Simulation results					
Port	Diameter (cm)	Field Penetration depth without sleeve (cm)	Normalized field penetration depth without sleeve	Field penetration depth with sleeve (cm)	Normalized field penetration depth with sleeve
Port 1	17.73	16.21	0.9143	13.09	0.738
Port 2	8.255	1.674	0.203	3.46	0.42
Port 3	10.145	10.8	1.0646	2.94	0.29
Port 4(a)	7.595	4.45	0.586	4.91	0.646
Port 5	4.225 (width), 20.965 (height)	5.565	1.32	9.162	2.168
Measurement results					
Port 1	17.73	10.16	0.573	-2.54	-0.1433
Port 2	8.255	0	0	0 (No sleeve)	0
Port 3	10.145	5.08	0.5	-10.16	-1
Port 4(a)	7.595	2.54	0.3344	0	0
Port 5	4.225 (width), 20.965 (height)	0	0	0 (No sleeve)	0

Table 4.3: Field penetration depth dependence on the hole diameter (Z axis)

Simulation results					
Port	Diameter (cm)	Field Penetration depth without sleeve (cm)	Normalized field penetration depth without sleeve	Field penetration depth with sleeve (cm)	Normalized field penetration depth with sleeve
Port 1	17.73	16.21	0.9143	13.09	0.738
Port 2	8.255	1.674	0.203	3.46	0.42
Port 3	10.145	10.8	1.0646	2.94	0.29
Port 4(a)	7.595	4.45	0.586	4.91	0.646
Port 5	4.225 (width), 20.965 (height)	5.565	1.32	9.162	2.168
Measurement results					
Port 1	17.73	12.7	0.7163	12.7	0.7163
Port 2	8.255	2.54	0.3077	2.54	0.3077
Port 3	10.145	10.16	1	10.16	1
Port 4(a)	7.595	5.08	0.66886	5.08	0.66886
Port 5	4.225 (width), 20.965 (height)	2.54	0.601	2.54	0.601

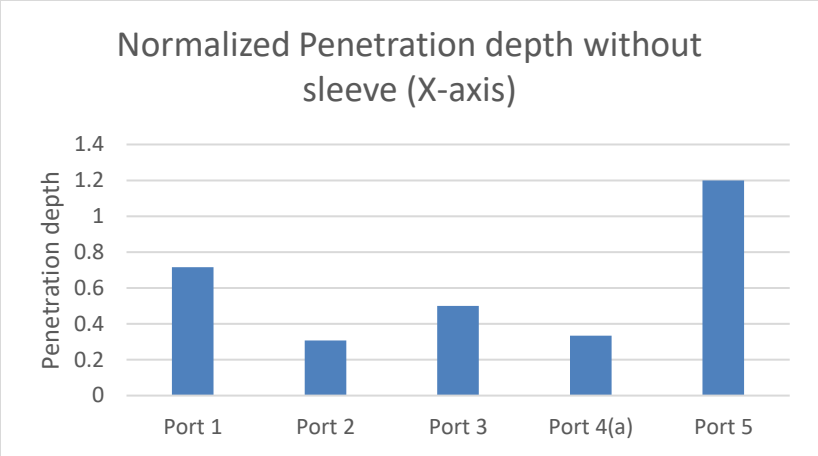

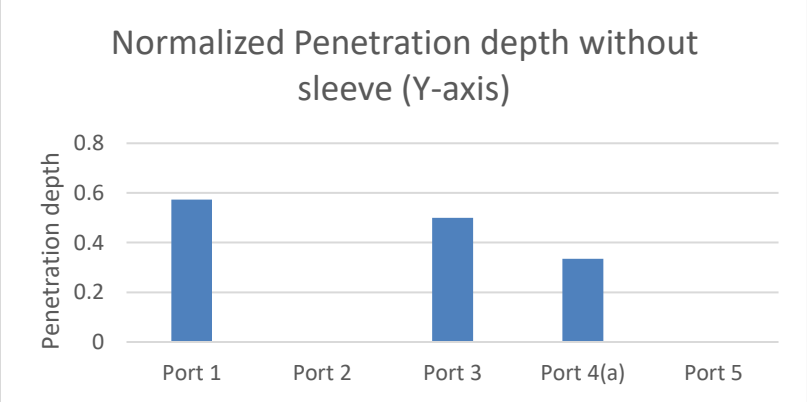

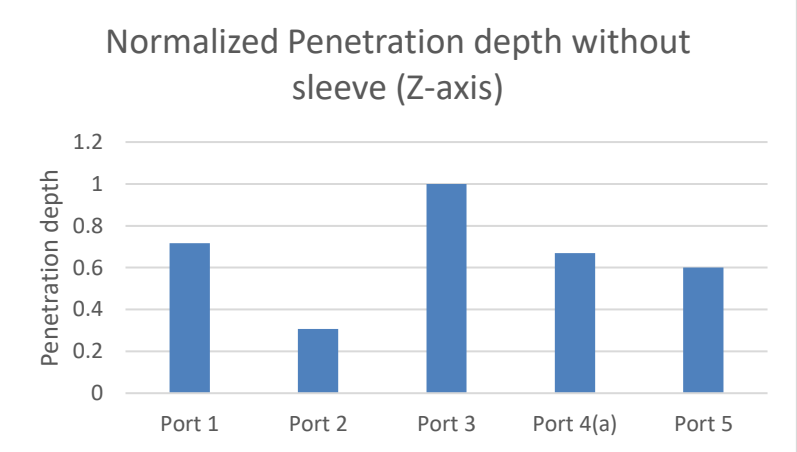

Figures 4.12(a) through 4.12 (c)

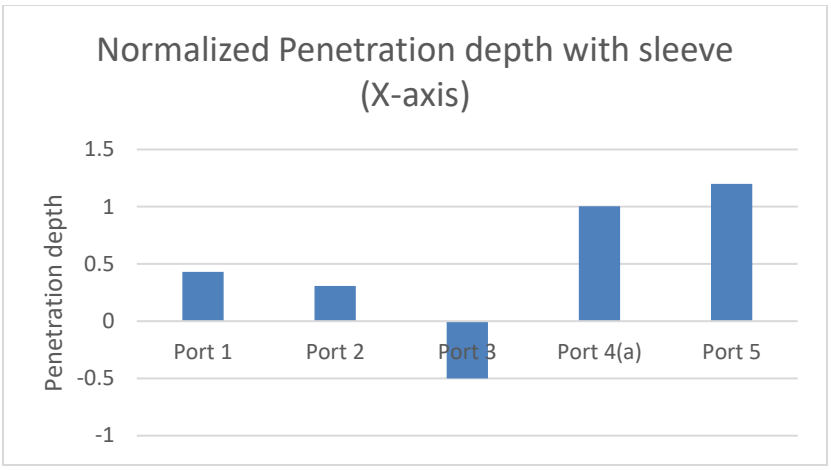

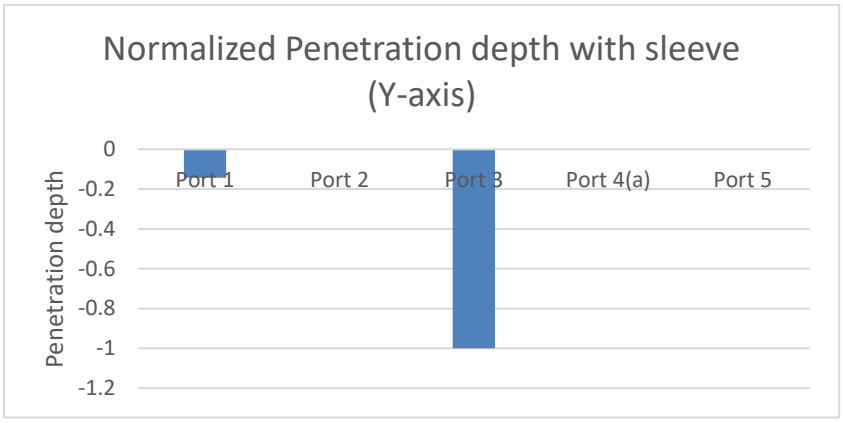

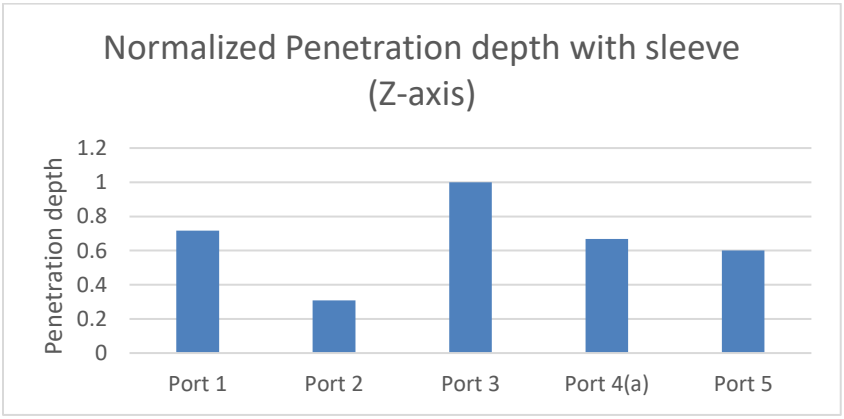

Figures 4.13 (a) through 4.13 (c)

Figures 4.12(a) – 4.12(c) and 4.13(a) – 4.13(c): The penetration depth for each port, on each axis, in its normalized value ($L_{penetration}$/Diameter of port), gathered from raw data measured in each environment. This data represents how far the magnetic field penetrates within each port, with (4.12) and without (4.13) the sleeves.

Bibliography:

[4.1] T.N. Lamichhane, L. Sethuraman, A. Dalagan, H. Wang, J. Keller, M.P. Paranthaman, Additive manufacturing of soft magnets for electrical machines—a review, Materials Today Physics, Volume 15, 2020, 100255, ISSN 2542-5293, https://doi.org/10.1016/j.mtphys.2020.100255 , (https://www.sciencedirect.com/science/article/pii/S2542529320300791)

5. Dynamic Ambient magnetic field

The ambient magnetic field that was investigated as part of this research has two known contributions thus far: The static ambient field that exists as part of the earth's field, and the dynamic ambient magnetic field generated by effects such as the Seebeck effect. The contribution from the Seebeck effect is the main focus of this portion of the paper, and the method in which the Seebeck voltage is generated. The Seebeck effect was investigated through constructing an apparatus that would measure it directly. The apparatus used to measure this effect had to be designed, fabricated, tested, and refined so that the effect could be measured with great reliability and reproducibility. To understand how this apparatus works, what is done to operate it, how the results in Chpater 6 were derived, and how they were confirmed and compared, a groundwork of understanding behind the Seebeck effect must first be laid down.

5.1 What is the Seebeck effect?

As a bit of quick history, the Seebeck effect, first observed in 1821 by Thomas Johann Seebeck, is an effect generated between two dissimilar metals joined at opposing thermal junctions. These junctions must have a temperature differential between one another to generate a voltage, that depends on the innate Seebeck coeffcient of the metals used. Every metal has a Seebeck coeffcient, and when they are laid in series with one another, they generate a small amount of potential, on the order of microvolts. It is not a significant amount of voltage, but for every metal that is joined in series, the voltage adds or subtracts (depending on the type of conductor it is), meaning that the effect is cumulative. A metal's seebeck coefficient is dependent upon the temperature it is held at, as well as what type of material it is. N-type materials have negative Seebeck coefficients, whereas P-type materials have positive coefficients. Depending on the joining mechanism for the two metals, as shown below in Figure 5.1, it is possible to form long chains of metallic seebeck connections that generate larger voltages in cumulative effect.

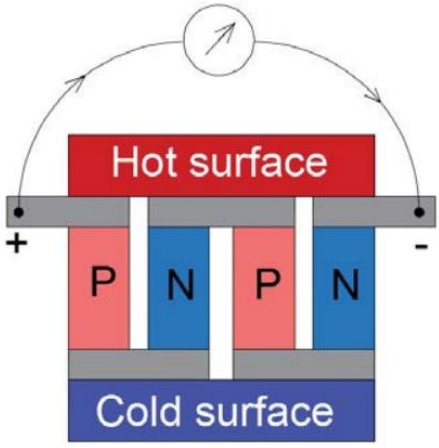

Figure 5.1 – Seebeck circuit diagram [5.1]

5.2 Mathematic understanding of the Seebeck effect

The Seebeck effect follows a relatively straight-forward set of mathematical parameters, defined below. The equations have had their symbols changed to match the rest of this paper, where S is the Seebeck coefficient, V is the voltage in μV, and T is the temperature in Kelvin. It should be noted, however, that for doped semiconductors, the equation becomes noticeably more complex (equation 5.3). These equations comprise the entirety of the thermoelectric effect, but are closely tied to two other thermoelectric equations. These equations are, namely, the Peltier effect, and the Thomson effect, both of which are considered to be closely tied to eachother and to the Seebeck effect. For the purposes of this paper, the Thomson and Peltier effects will be set aside, and instead, the focus will be set upon the Seebeck effect. The following equations are gathered from various sources detailed in the bibliography of this Chapter.

$$S = \frac{\Delta V}{\Delta T} \tag{5.1}$$

(Absolute Seebeck coefficient calculation) [5.2]

$$\Delta V = (S_A - S_B)\Delta T \tag{5.2}$$

(Approximation of the Seebeck coefficient calculation for two metals)[5.3]

$$S = \frac{8\pi^2 k_B^2}{3eh^2} m^* T \frac{\pi^{\frac{2}{3}}}{3n} \tag{5.3}$$

(Doped semiconductor seebeck coefficient) [5.2]

where k_B, e, h m^* and n are, respectively, the Boltzmann constant, the carrier charge, Planck's constant, the effective mass of the charge carrier, and the carrier concentration. The equations used for calculation of the results in this paper are as follows:

$$S_a(T_{ave}) = -\frac{V}{\Delta T} + S_b(T_{ave}) \tag{5.4}$$

(Simplified approximate calculation of the integral method based on [5.8], suitable for large values of ΔT) [5.7]

$$\frac{\Delta V_{ab}}{\Delta T} = S_{ab}(T_0) + \Delta S_{ab}(T_0) \tag{5.5}$$

(Simplified calculation of the differential method from [5.8], suitable for small values of ΔT) Where T_0 is defined as:

$$T_0 = \left(\frac{T_1 + T_2}{2}\right) \tag{5.6}$$

Equations 5.4 and 5.5 are different ways of calculating the Seebeck coefficient for different values of ΔT, but for the purposes of this paper, larger ΔT values were obtained and used for calculation. Equation 5.4 was predominantly used for the bulk of the mathematics of this paper. It is through the above equations, though, that the Seebeck coefficient can be derived if one of the metal's coefficients in the junction is known apriori. For the purposes of this thesis, bonded

metals and pure niobium will be investigated and characterized, due to their involvement and role in the construction of FRIB HWRs, whether they are $\beta = 0.53$ or otherwise. More information on the joining of metallic samples can be found in chapter 6.

The "absolute" Seebeck coefficient refers to the Seebeck coefficient of one metal with respect to the temperature difference across its ends, and the voltage generated due to that temperature differential. In order to find the absolute Seebeck coefficient of a metal, two temperatures must be established across the metal as in Figure 5.2, which details two setups that can be used for the experiment. One in which the samples are clamped at the heat and cold sources, and another in which the sample is clamped instead of the temperature sources. These two configurations represent the potentiometric (four-probe) and the axial-flow (two-probe) arrangements. In these cases, $T_2 > T_1$ for the purposes of defining temperature.

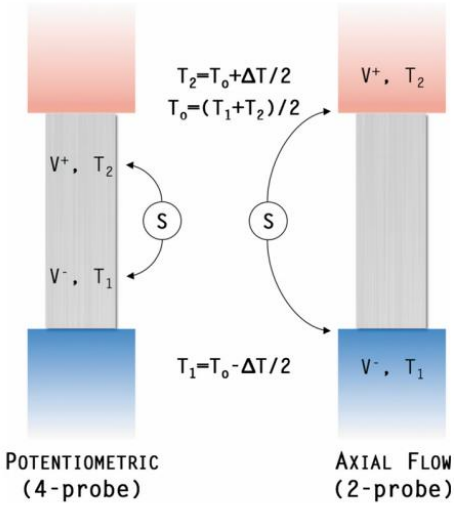

Figure 5.2 – Axial-flow and Potentiometric sample setup diagrams [5.8]

5.3 Magnetic contribution from the Seebeck effect

A magnetic field, B, is usually generated by a current, I, and for a current to flow, a complete circuit must be introduced. It is already a known fact that the seebeck effect produces a voltage difference across two points. At one end, heat is removed by a cooling method of choice, where the other end is heated. On its own, the seebeck effect does not generate a current, unless it is generated within a circuit. The mehcanisms behind the magnetic contribution to this effect is detailed much more extensively by Ansermet et al. [5.6], but for the purposes of this paper, it is sufficient to say that a generated current, running through the circuit, generates a magnetic field. It is this magnetic field that is thought to become trapped inside of cavities when cooldown occurs, causing losses, as well as a degraded Q_0 and E_{acc} performance value.

The magnetic field that is generated by this current, when flowing through the sample, is defined by the integral in equation 5.7 for its theoretical calculation as

$$\oint Hdl = I_{enc} \tag{5.7}$$

where H is the magnetic field intensity (Amps per meter) (A/m), and I_{enc} is the current enclosed (Amps) (A) by the path, or the sample length.

The integral demonstrates that the line integral of the magnetic field H over the path enclosed is equal to the current enclosed. This is also known as Ampere's Circuit law, which can be simplified for the case of this thesis, to equation 5.8

$$H * L = I_{enc} \tag{5.8}$$

where L is the path length, or the sample length, in meters.

It is desired to understand, theoretically, the magnitude of the magnetic flux density B contributed by the metallic sample in use. This can be determined by equation 5.9

$$B = \mu_r \mu_0 H \tag{5.9}$$

where μ_r is the relative magnetic permeability of the material, and μ_0 is the permeability of free space.

It can then be compared to the experimentally measured magnetic field, and from there, it can be directly correlated to determine how much current was generated by the closed seebeck circuit. The purpose of understanding and measuring the magnetic field from the experiment is to determine the magnitude of the field generated by the seebeck effect, and thereby, its effect on the system. It has already been stated previously, and in the abstract that most of the loss inside of the $\beta = 0.53$ HWR cavities is thought to be due to the residual resistance generated by the dynamic ambient field. This dynamic ambient magnetic field, in this case, is generated by the seebeck effect in a circuit with the other metal parts inside of the cavity.

Bibliography:

[5.1] Milkov, Nikolay & Evtimov, Teodossi & Punov, Plamen. (2015). Advanced technologies for waste heat recovery in internal combustion engines. International journal MTM. IX. 60-66.
[5.2] Xingyi Zhu, Yue Yu, Feng Li, A review on thermoelectric energy harvesting from asphalt pavement: Configuration, performance and future, Construction and Building Materials, Volume 228, 2019, 116818, ISSN 0950-0618, https://doi.org/10.1016/j.conbuildmat.2019.116818, https://www.sciencedirect.com/science/article/pii/S0950061819322482
[5.3] S. Kasap, 2001, *Thermoelectric Effects in Metals: Thermocouples*, Web-Materials, Thermoelectric Effec#38D8EF.pdf
[5.4] Xiaoli Liu, Ruchita Jani, Esther Orisakwe, Conrad Johnston, Piotr Chudzinski, Ming Qu, Brian Norton, Niall Holmes, Jorge Kohanoff, Lorenzo Stella, Hongxi Yin, Kazuaki Yazawa, State of the art in composition, fabrication, characterization, and modeling methods of cement-based thermoelectric materials for low-temperature applications, Renewable and Sustainable Energy Reviews, Volume 137, 2021, 110361, ISSN 1364-0321, https://doi.org/10.1016/j.rser.2020.110361, https://www.sciencedirect.com/science/article/pii/S1364032120306493
[5.5] Ning Jia, Jing Cao, Xian Yi Tan, Jinfeng Dong, Hongfei Liu, Chee Kiang Ivan Tan, Jianwei Xu, Qingyu Yan, Xian Jun Loh, Ady Suwardi, Thermoelectric materials and transport physics, Materials Today Physics, Volume 21, 2021, 100519, ISSN 2542-5293, https://doi.org/10.1016/j.mtphys.2021.100519, https://www.sciencedirect.com/science/article/pii/S2542529321001802
[5.6] Ansermet JP, Brechet SD. Magnetic Contribution to the Seebeck Effect. Entropy (Basel). 2018 Nov 30;20(12):912. doi: 10.3390/e20120912. PMID: 33266636; PMCID: PMC7512497.
[5.7] Shpani, Liana and Ge, Mingqi and Holic, Adam and Liepe, Matthias and Sears, James and Verboncoeur, Nicole; Measuring the Seebeck Coefficient at Cryogenic Temperatures for LCLS-II-HE Project; 10.18429/JACoW-LINAC2022-THPOGE15; JACoW; LINAC2022; THPOGE15; 2022.
[5.8] Martin, J. , Tritt, T. , Wong-Ng, W. and Uher, C. (2010), High Temperature Seebeck Coefficient Metrology, Journal of Applied Physics, [online], https://doi.org/10.1063/1.3503505 (Accessed April 15, 2025)

6. Measuring the Seebeck thermoelectric effect

The Seebeck thermoelectric effect is thought to be the largest contribution to the residual resistance on SRF cavities, due to the buildup of potential charge between metals. It is the purpose of this section of the thesis to investigate and validate the Seebeck thermoelectric effect using the metals commonly found within SRF cryomodules. Metals like Copper, Nickel Copper, Aluminum, Titanium, and Niobium will have their theoretical seebeck coefficients validated and compared to experimental data taken during experimentation. It is necessary to understand the design, and fabrication of the measurement system developed for the measurement of the Seebeck coefficient. Each experiment's data, and the methodology of experimentation are also explained within this section. Each experiment will investigate pairings of two dissimilar metal combinations, and report the comparison between theoretical and experimental voltage measurements.

6.1 Seebeck measurement system design

The Seebeck measurement apparatus's design took inspiration from L. Shpani et al. [5.7] as a starting reference. Initially, the shape of the apparatus was designed to be a cylinder, so that it could fit in line with the Dewar's chamber. The Dewar's chamber is 20.32 cm in diameter, and 153.035 cm in depth for reference. It was also necessary for the apparatus to be easy to transfer in and out of the Dewar, so that the design could be modified, and adapted as necessary. This would mean constructing it out of aluminum, or another lightweight and heat conductive material. Considerations about the first method of cool down comprised of submerging the entire cylinder in the liquid nitrogen. The shape of the holding vessel was important for the path that the heat would flow through to cool down the sample. The cooling path of the vessel had to be thought out carefully so that cool down of one end of the sample, while keeping the other end warmer, was possible. This posed an issue; considering that controlling the cool down of the entire assembly would be impossible if the entire vessel was submerged, the cooling would be too strong to sustain a higher temperature at the other end. More importantly, the cool down would be too rapid to sustain a careful gradient over time.

The solution to this was to affix one end of the sample directly to a cooling source, while allowing the other end to remain warm, and cool over time. To this, a cold head with a copper fixing was designed to be attached at the end of a reservoir filled with liquid nitrogen. The sample was electrically separated from the copper fixture by a ceramic spacer (see Figure 6.2 and 6.3) which cut the thermoelectric circuit in the sample from flowing through the copper head. Using a vertically aligned sample holder allowed use of the larger depth of the Dewar to better contain the apparatus and sample. The vertical orientation also allowed fabrication of larger samples of metal to test within the Dewar. Figure 6.1 shows the construction of this testing apparatus inside of the Dewar.

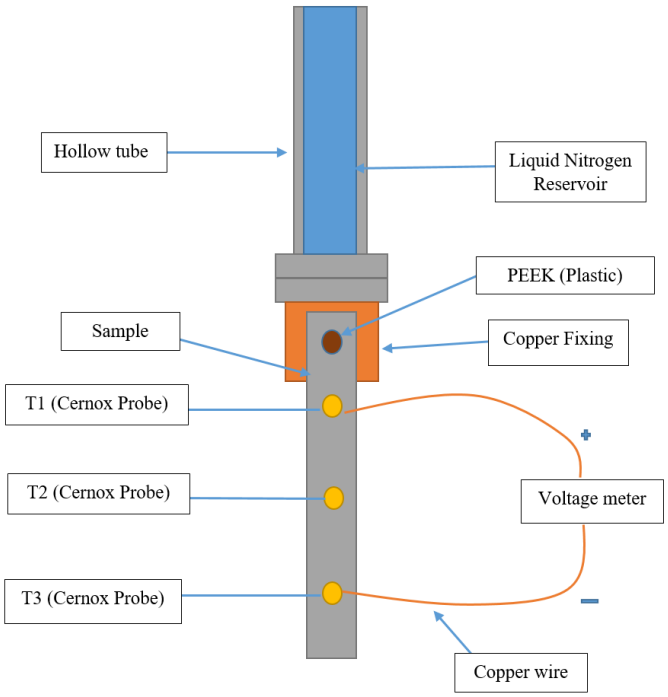

Figure 6.1 – Apparatus setup inside of the Dewar

The samples used were designed to be long strips of metals that had bored holes drilled through them to bolt to the copper fixture, and to bolt the temperature probes directly to the surface of the metal, where the voltage measurements would be made. Figures 6.2, 6.3, 6.4, 6.5, 6.6 and 6.7 illustrate these samples.

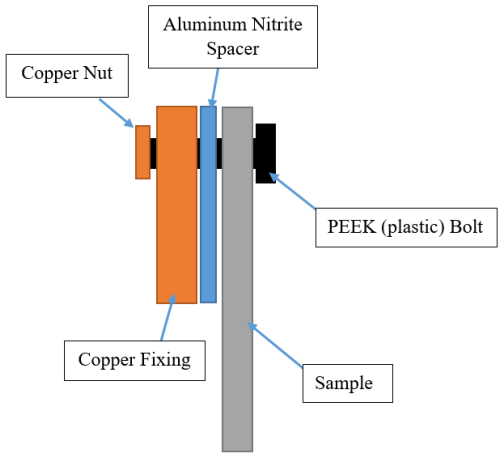

Figure 6.2 – Cross section of Copper fixture assembly (Side view)

Figure 6.3 – Aluminum Nitrite and Nitrate spacers

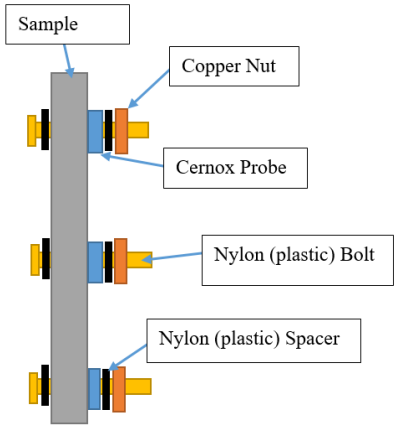

Figure 6.4 – Cross section of Cernox probes attached to the sample

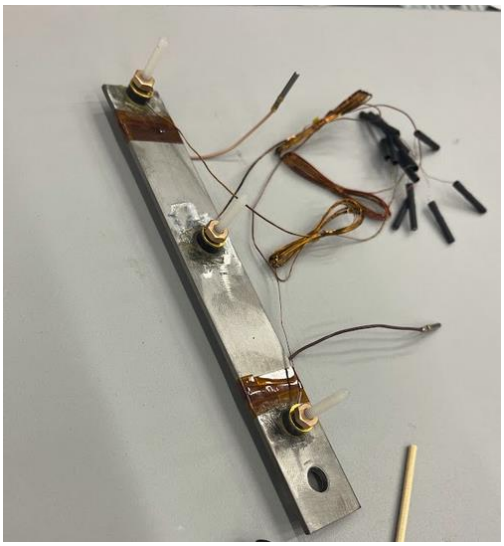

Figure 6.5 – Assembly of bolted Nb sample

Figure 6.6 – Stainless Steel and Titanium Bimetallic sample

Figure 6.7 – Niobium and NbTi alloy Bimetallic sample

The Seebeck coefficient is an innate property of a metal sample, measured in units of microvolts per Kelvin (µV/K). When two metals are placed in a series circuit, much like the one shown in Figure 6.3, the Seebeck coefficients, innate to each metal, combine to provide a cumulative effect from both coefficients. If one were to try and calculate the Seebeck coefficient for a metal which was unknown, using a known Seebeck coefficient value for a metal at a given temperature would allow for the calculation of the other metal in the series. The concept of the design inspired from Liepe et al. [5.7] was to use wires of different metals attached at opposite ends of

the sample to generate a combined Seebeck coefficient (See figure 6.8)

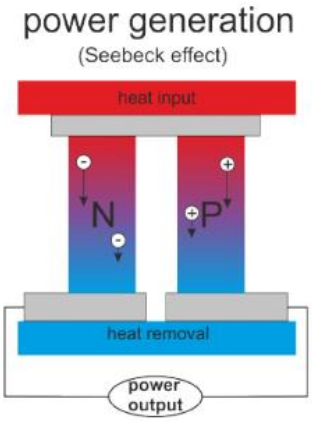

Figure 6.8 – Seebeck effect diagram

The voltage measurements, integral to the design of the system, needed to be made at the same location as the temperature measurements. This is so that the temperature differential and voltage generated could be made at the exact same spots. The importance of this comes down to the fact that when making accurate Seebeck voltage calculations, there must be no question as to how much voltage is being generated at the sites where the temperature is taken. When calculating the Seebeck voltage (see Chapter 5), the mathematics imply there needs to be a certainty behind the temperature differential and the voltage produced from that differential. The original plan to measure voltage was to be take the measurement two wires of a metal different from the sample, with one at each end (see Figure 6.9). A bolt to the sample would mechanically fasten each wire. In order to receive better electrical contact, and to assure that a connection was secure, wires were welded to the sample instead (see Figure 6.10). Copper was the metal that was best available for use at the time, and it had a well-known Seebeck value. This prompted its use in the electrical connection to the samples used in this thesis.

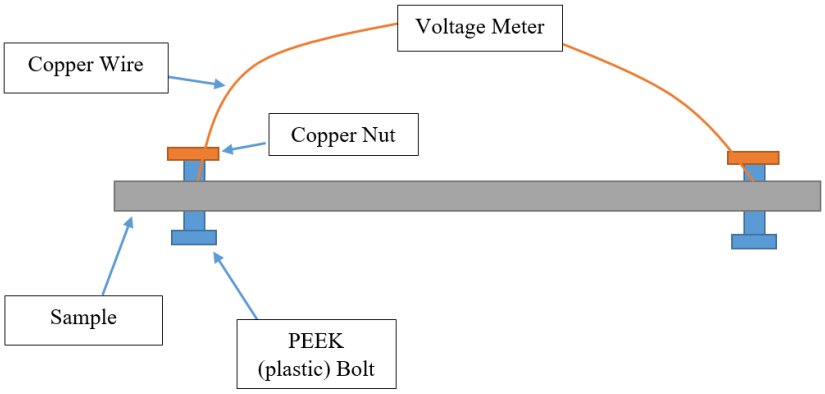

Figure 6.9 – Mechanical fastening method for the sample

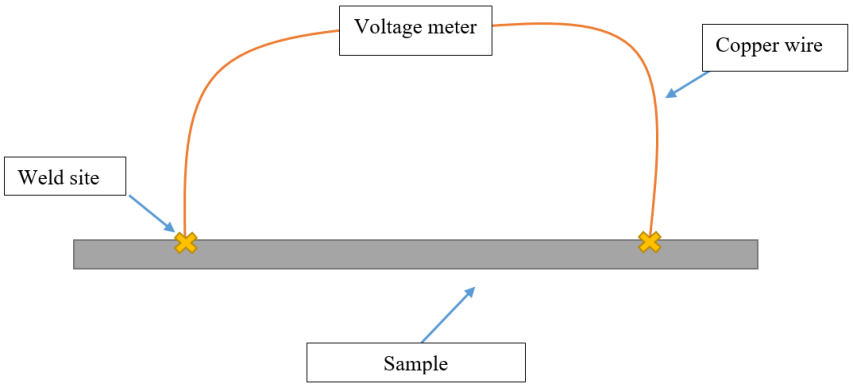

Figure 6.10 – Welding-fastening method for the sample

6.2 Fabrication and assembly of the system components

The decision was made to attempt to produce a measurement apparatus similar to the ones in [5.7] and [6.1]. For the wires of both the temperature sensors and the voltage output to be received through the cold head, shown in Figures 6.11 and 6.12, there needed to be a harness created for the wires to connect and feed to outside measurement boxes. Caution was necessary, as a connection between metallic joints at any location could cause a short, or an unwanted second Seebeck connection. The harness for this project used a wire connection fed through the top of the vessel using a 19-pin connector, which fed all of the measurement data to the boxes used. It was originally designed as a piece of twisted ribbon cable that coiled around the tube for the cold head so that temperature measurements could be made with some reliability. Due to the sensitive nature of the voltage measurements, and the temperature sensors, the ribbon cable was shielded in aluminum tape and foil to prevent any signal noise from coming through.

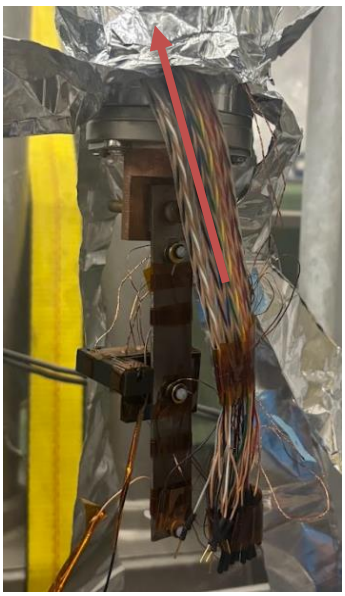

Figure 6.11 – Wires feeding through the harness into the Nb sample

Figure 6.12 – Cold head feed through

The temperature probes chosen for use in initial testing were RTD probes that adhered to the surface of the sample. Several trials were conducted to understand the lowest temperature the system could reach, to understand what could be improved. The initial temperature measurements on the copper block showed that the cold head did in fact reach close to liquid nitrogen temperatures. Then, work on a set of trials to determine the potential temperature gradient that could be established across the metallic sample, and the copper cold block began. The results were not ideal, as shown in table 6.1 below for one of the initial trials.

Table 6.1

Time (Minutes)	Temp (Cu) (Kelvin)	Temp (Nb Sample) (Kelvin)
0	294.35	294.29
7	228.61	261.89
17	93.104	148.82
27	86.065	122.97
37	85.15	119.8
47	84.535	119
57	84.205	118.55
67	83.979	118.15

The solution to this was to eliminate any outside temperature effects that would warm or prevent the sample from cooling down properly. The radiative heat effects of the dewar itself had to be considered, since the dewar was not being cooled down. Black body radiative heat effects must have been keeping the sample from reaching the temperature desired. The sample was then shielded, and the copper block was surrounded with a metallic aluminum umbrella structure, made from foil and tape. In addition, the sample was wrapped in MLI, which is a multi-layer insulative material that is designed for low temperature black body effects. When these materials

were used in combination, the results were much more favorable. The temperature that was achieved across both of the sensors attached to the copper block was around 77 K, as seen in table 6.2 below.

Table 6.2

Time (Minutes)	Temp (Cu) (Kelvin)	Temp (Nb Sample) (Kelvin)
0	293.59	293.54
10	204.48	214.004
20	106.76	134.67
30	92.448	119.02
40	87.54	110.19
50	84.343	103.39
63	81.417	96.487
70	80.465	93.815
80	79.72	90.742
90	79.012	88.39
100	78.676	86.66
110	78.293	85.264
120	78.007	84.198
130	77.77	83.302
140	77.593	82.586
150	77.437	81.971
160	77.342	81.592
170	77.24	81.169
180	77.161	80.861
190	77.094	80.602
200	77.03	80.366

The original setup would allow for the sample to bolt the sensors onto it. Since it was not possible to use metallic bolts, out of concern for an unwanted metallic junction and Seebeck effect, the metallic bolts were switched to plastic nylon bolts. The plastic nylon bolts were separated from the metal sample with small nylon spacers and copper nuts that were spaced from the metallic sample. Two ways to hold the temperature sensors in place were considered, which would allow re-use of the sensors. One of them was as described above, with plastic nylon bolts and spaced nuts, and the second option was to use a varnish (GE Low Temperature Varnish (59-C5-101)) that could be dissolved using acetone. The important part of this consideration is that there needs to be reliability and reproducibility within the data, both temperature and voltage. The probes fixed to the sample were XCX-1010-CU-HT-1.4LE-10582 Cernox temperature probes.

6.3 Temperature calibration of system probes

To assure that the temperature readings were accurate, calibration for the temperature probes is a necessary step. To start with calibration, curves from the original manufacturer website were uploaded to the probes. The temperature intended for measurement was around 77 K, the temperature of liquid nitrogen. The ideal scenario assumed that the probes did not need any calibration to begin with, and the worst case was that each sensor read completely different numbers for the same temperature. When calibrating, it is important to make measurements with the probes on the same material, close together, set to the same temperature.

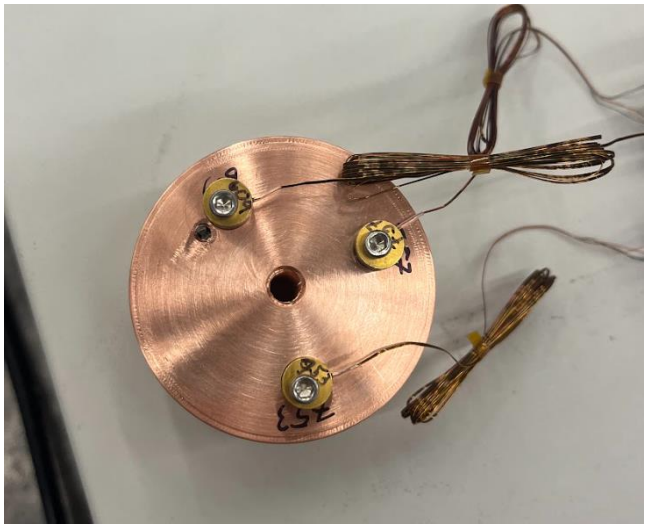

Figure 6.13 – Nitrogen calibration block

Figure 6.14 – Copper block submerged in liquid nitrogen

The setup above shows a copper cylinder with the sensors secured to the top surface of it, submerged within liquid nitrogen. The process for calibration is simple: Submerge the cylinder with the sensors attached, and allow the liquid nitrogen to boil off over time. The result should be a cool down and warm up curve that shows the gradual increase in temperature. It was important to understand if there were any inconsistencies in the warm up data, so that it was possible to account and correct for it during cool down in the Dewar. A different temperature measurement at the same point in time has a variety of causal factors, such as different response times, and problems transitioning in temperature. It is hard to say which of these makes the most contribution over time, but in the end, it is desired to be able to report temperatures with consistency and reliability. If the cool downs for the Seebeck effect were to be accurate, it was important that all three sensors showed the same temperature on the same piece of metal, cooled down at the same time. The three cool down trials conducted yielded the results shown below.

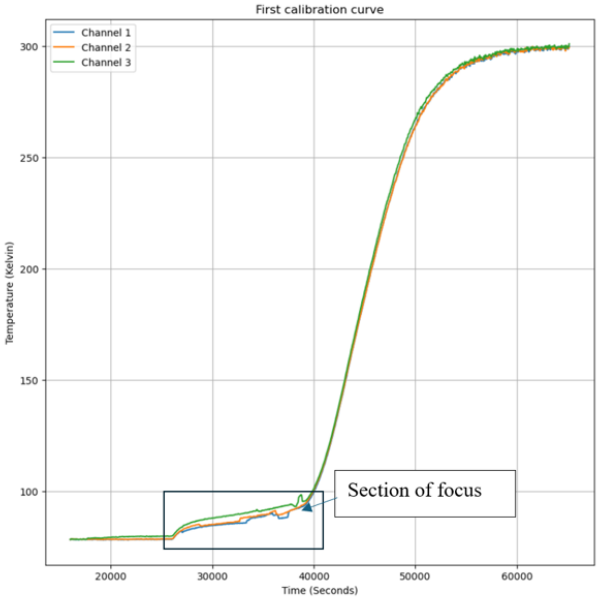

Figure 6.15 – First Graph

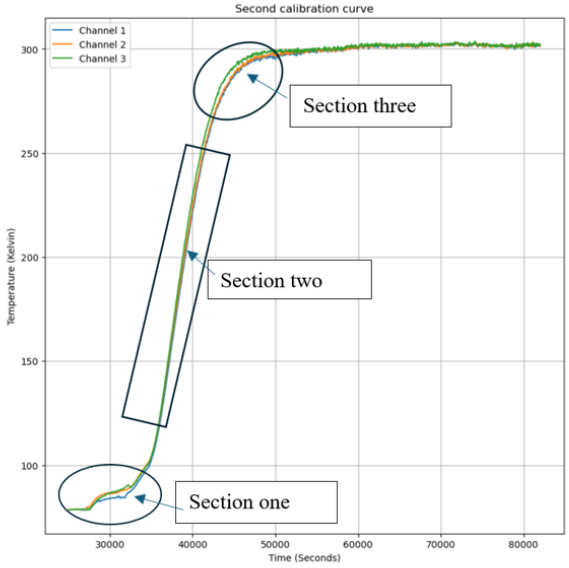

Figure 6.16 - Second Graph

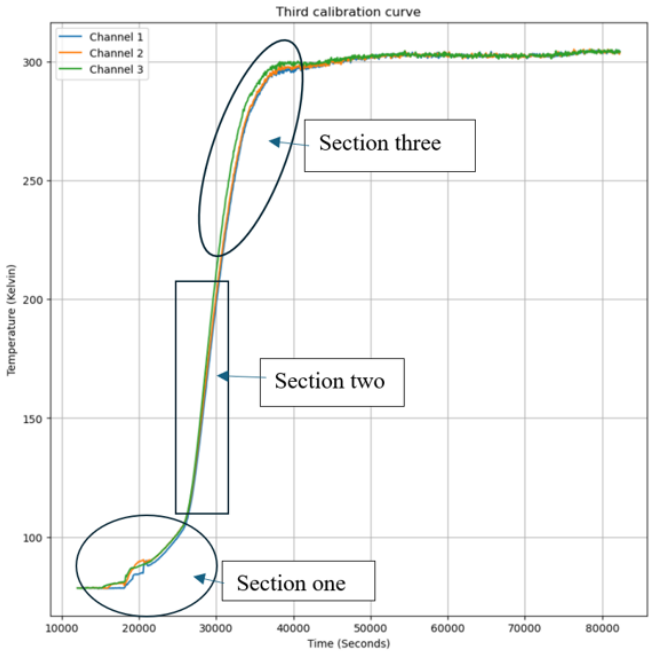

Figure 6.17 – Third Graph

The cooldown trials above show that each curve has at least one area where the measurements do not match each other, indicating that the sensors either do not agree, or that during warmup and cooldown, the response time for each sensor is different. Additional analysis revealed that the second and third trials were similar with their results, particularly in the highlighted region shown above. In addition, the first trial had a different behavior, which may have been due to the lowering rod affixed to the block left inside of the cylinder, unlike trials two and three. The point at which the sensors disagree seem to be when the liquid nitrogen has completely boiled off, and the temperature starts to climb again. At this point, the copper cylinder starts to warm up, and slowly climbs in temperature towards 293 K (room temperature). In the second and third graphs (Figures 6.16 and 6.17), the warmup starts to differ in section 3, where the third probe reads a different temperature over time than the first and second probes. In the first graph (Figure 6.15), this does not take place, which means that something was fundamentally different about the first trial. Further attempts to categorize and understand the difference in temperature over time resulted in the figure 6.18 below, which depicts the line of best fit for the third trial for ΔT of Channel 3 and Channel 2.

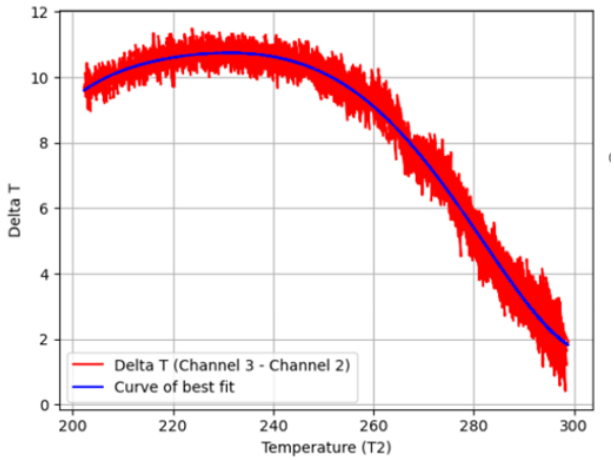

Figure 6.18 – Line of best fit for ΔT (Trial 3)

To understand why the probes were reading such different temperatures in these regions, another series of temperature measurements were taken. This time, it was to ascertain whether the sensors could reach an agreement at a known temperature. The three additional mediums used for calibration were hot water (approximately 303 K), ice water (273 K), and dry ice (approximately 194 K when sublimating). Below are the three setup conditions used for each test.

Figure 6.19 – Ice bath calibration test with the sensors submerged underneath a layer of MLI sheeting

Figure 6.20 – Dry Ice calibration test with the sensors placed directly into dry ice pellets

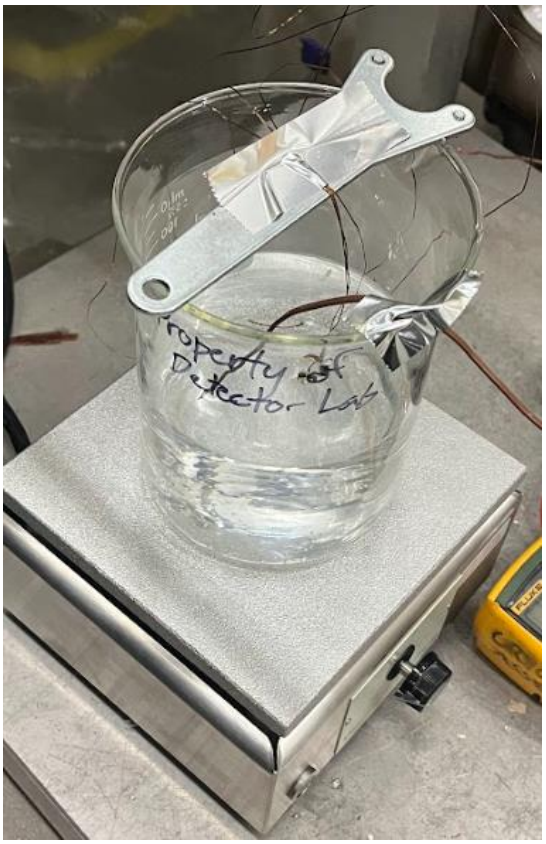

Figure 6.21 – Hot water calibration test with sensors submerged in 30 C water on a hot plate

The results of the temperature calibration experiments show that at higher temperatures, the Cernox probes are not reliable, due to the 10 K difference in actual temperature versus what the Cernox probes measured. The reason for this may be that the operational upper limit of the probes is set at 330 K, where at which point, they stop reading temperatures entirely. The output on the temperature box becomes an "Over Under" output. The reading indicates that this is the maximum temperature for the probes to handle, and that the other measurements may be more accurate. The following tables have this data, with analysis done to determine the average temperature, and the standard deviation of each probe from that average. The following figure represents the line of best fit between the original temperatures (the accepted values), and the experimental data points. The equation for each line represents a correction equation that allows correction of the temperature data received from the Seebeck experiment to come as close to the real value as possible. The correction equation's purpose is to correct for the temperature probe's error, and produce an accurate reading of what the temperature really is.

Table 6.3 – Original Temperature data (in Kelvin)

	Liq. Nit. 1	Liq Nit. 2	Liq Nit. 3	Dry Ice 1	Dry Ice 2	Dry Ice 3	Dry Ice 4	Ice water 1	Ice water 2	Ice water 3	Ice water 4	Hot water 1
Channel 1	78.111	78.421	78.421	190.5	188.87	187.53	190.52	280.39	281.64	281.73	281.58	315.97
Channel 2	78.211	78.504	78.517	190.15	188.01	187	189.3	280.22	281.91	281.06	281.06	315.45
Channel 3	78.158	78.5	78.509	190.12	188.12	187.5	189.09	280.16	280.98	280.66	281.07	315.06

Table 6.4 – Average data for each trial, and standard deviation from each channel

	Average Liq. Nit. (K)	Average Dry Ice (K)	Average Ice water (K)	Average Hot water (K)
Channel 1	78.31766667	189.355	281.335	315.97
Channel 2	78.41066667	188.615	281.0625	315.45
Channel 3	78.389	188.7075	280.7175	315.06
Standard Deviation	0.039730885	0.329209913	0.252671834	0.372767

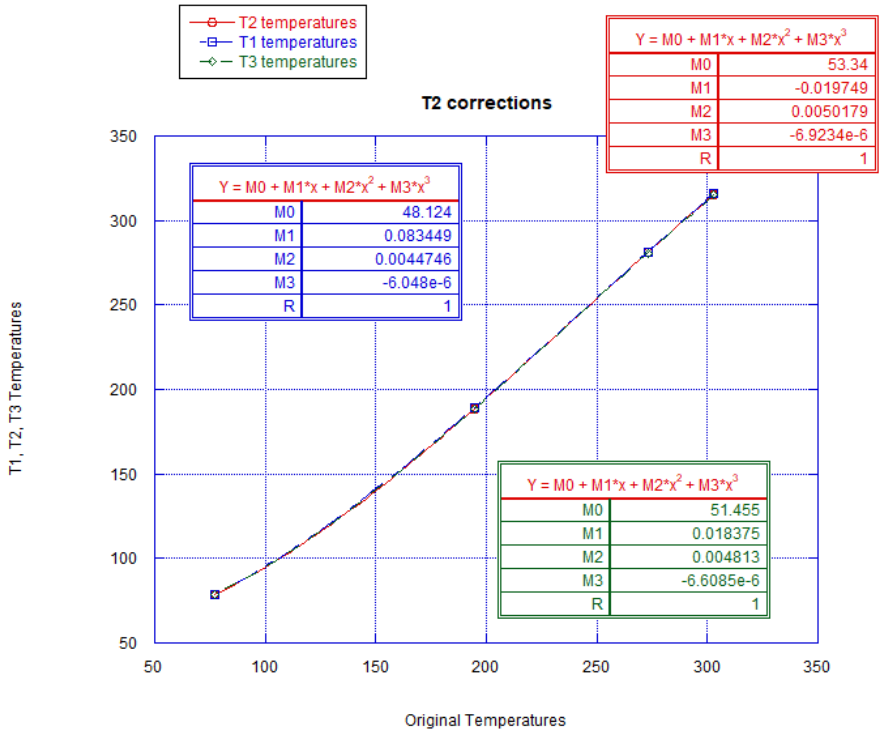

Figure 6.22 – Lines of best fit for accepted temperature vs measured average temperature

The figure above shows the relation between the original temperatures, and the measured average temperature that was recorded for each sensor. The relationship between the two of them is given by the associated third order polynomial for each sensor. When running the temperature through the polynomial for each sensor, it should correct to find the actual temperature for each sensor, giving a more accurate reading for each one. The reading is then used to find the ΔT between the hot and cold ends (T_1 and T_3), before being plugged into equations 6.2 qand 6.3 (below) from section 6.6. It is shown again below to give a better understanding of how the seebeck measurement validation works, however, it is detailed better in the next section of the paper.

6.4 Seebeck measurement validation

In order to validate that the seebeck measurements are within an acceptable percent error of the theoretical value, there must first be an understanding of what the expected Seebeck coefficient's value should be. There are multiple literature resources that can substantiate the expected Seebeck value ranges for a given material, and a temperature. Using these such ranges, one can extrapolate a curve of best fit, and use it to find a seebeck value for any given temperature. Figure 6.23 shows the ranges of values for Niobium, and a few other given materials. Figure 6.24 shows the curve of best fit for a graph of Temperature versus Seebeck ceofficient for niobium, which cointains an equation that will be useful in validating the seebeck coefficient for that temperature range and sample. Figure 6.25 shows the same, but for titanium, which has a lower order polynomial fit.

Table 5.2. Values of S in Pure Transition Metals below Room Temperature (μV deg^{-1})

Element	Orientation	10 K	20 K	50 K	80 K	100 K	150 K	200 K	250 K	273 K	References
Group IIIB											
Sc	Ave	−1.6	−3.0	−8.0	−12.7	−14.0	−15.6	−16.3	−16.5	−16.2	64N1, 69M1, 69V1
Y	Basal	−0.3	−0.4	−3.3	−4.5	−4.4	−3.1	−1.9	−0.9	−0.7	59J1, 61B1, 65S2, 69T3,
	c-axis	−0.5	−0.4	−2.8	−4.5	−4.9	−4.6	−3.2	−1.4	−0.5	69V1
La		–	–	–	0	+0.3	+0.4	+0.7	+1.0	+1.3	61B1, 69V1
Group IVB											
Ti	Ave	–	–	−3.0	−3.0	−2.6	0	+2.0	+4.0	+4.5	41P1, 51W1, 69V1
Zr	Ave	–	–	0	+3.0	+4.5	+7.5	+8.5	+9.5	+9.5	41P1, 52A1, 69V1
Hf	Ave	–	–	–	0	0	+2.5	+3.7	+4.7	+5.3	69V1
Group VB											
V	Ave	+0.19	+0.76	+2.45	+2.91	+2.65	+1.52	+0.72	+0.26	+0.13	41P1, 63M1, 67S2, 70C1
Nb	Ave	+0.31	+0.98	+2.73	+3.09	+3.13	+1.42	+0.65	−0.04	−0.20	41P1, 65W1, 70C1
Ta	Ave	+0.36	+1.03	+1.41	+0.78	0	−0.8	−1.5	−2.0	−2.2	41P1, 70C1
Group VIB											
Cr	Ave	+3.1	+6.7	+8.2	+5.0	+5.0	+7.0	+11.8	+17.5	+18.8	41P1, 68S1, 68T2, 74G3
Mo	Ave	−0.02	−0.11	−0.48	−0.2	+0.1	+0.94	+2.50	+4.08	+4.57	41P1, 70C1
W	Ave	+0.05	−0.28	−2.78	−3.70	−4.04	−2.45	−1.41	−0.10	+0.56	41P1, 70C1, 73G2, 73T1, 74G2

Figure 6.23 – Table of Seebeck coefficients for some pure transition metals [6.4]

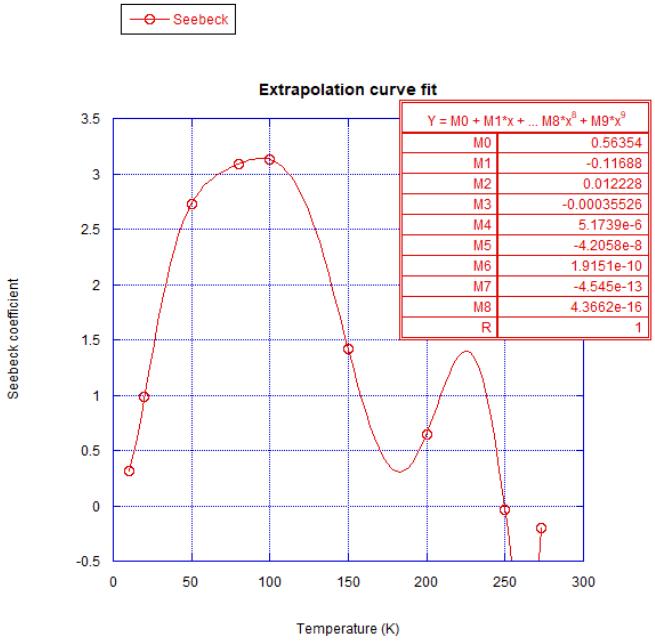

Figure 6.24 – Niobium extrapolation curve

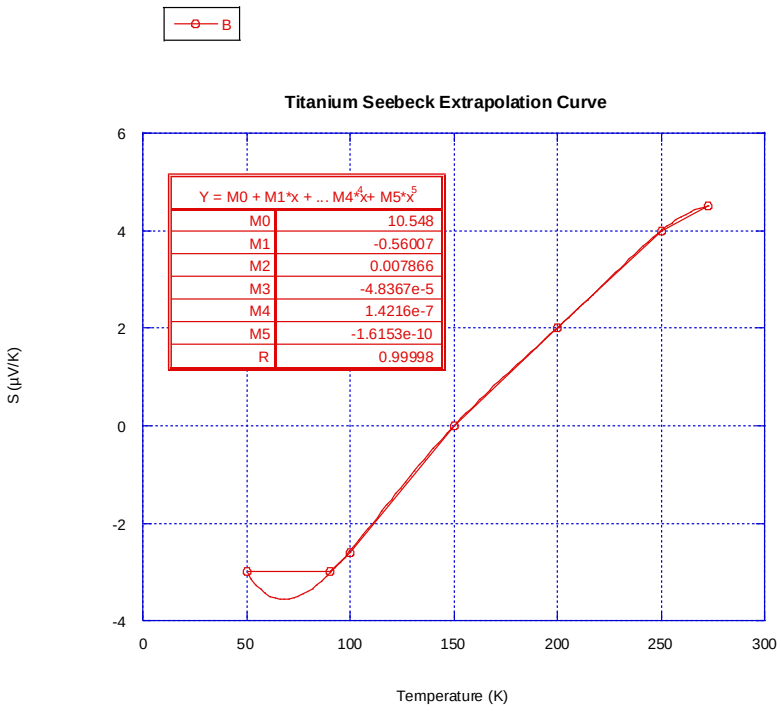

Figure 6.25 – Titanium extrapolation curve

When using the seebeck coefficient, refer to equation 6.1 below to determine the appropriate voltage generated.

$$\Delta V = S * \Delta T \quad (6.1)$$

Where S = Seebeck Coefficient (µV/K)

The following equation, which is taken from Chapter 5, also for the calculation of the seebeck coefficient, is used when the reference material has a known seebeck coefficient, but the metal it is connected to does not. When calculating the voltage, the order of magnitude should be taken into account. Microvolts are most often the unit of measurement for voltage in this experimental process, and as such, are hard to measure directly. In order to assure that the voltage received is close to what is expected, the theoretical value calculated from the theoretical seebeck coefficient for each metal is compared with the experimental voltage received. This voltage should remain within roughly 10% of the original theoretical value, though outside error sources should be recognized and understood. The ambient temperature in the air, the initial offset of the voltage meter due to that temperature, shielding of wires, and good thermcal and electrical contact are all points of importance to check before beginning the measurements.

6.5 Sample Preparation

There were three samples used during the development of this thesis document. The first sample tested was a strip of niobium, which was flash etched over its surface using Buffer Chemical Polish (BCP), and sanded near the points of contact for the cernox temperature probes to ensure a proper thermal connection. The second sample was a square of explosion bonded stainless steel to titanium, which was reasonably shorter than the rest of the samples, as seen in figure 6.3. The

last sample investigated was a strip of niobium that had been welded to a piece of NbTi alloy, using titanium as a filling material in the gap. Apiezon L grease was used as a thermal paste to help ensure even thermal contact between the sensors and the sample. It was applied to the copper cold head and aluminum nitrite spacer for each experiment as well. The measured dimensions of each probe are described below in table 6.5. The different geometry of the stainless steel to titanium sample contributed most to the results shown in section 6.6 and 6.7.

Table 6.5 – Sample dimensions

Sample	Length	Width	Thickness
Niobium	146.3 mm	20.3 mm	2.15 mm
SS/Ti	45.1 mm	43.05 mm	3.1 mm
Nb/NbTi	129.8 mm	Nb: 29.4 mm NbTi: 30.25 mm	Nb: 3.2 mm NbTi: 3.35 mm

The reason the SS/Ti and Nb/NbTi samples were fabricated follows from the location of the materials on a physical SRF cavity. The helium filling and helium return ports have stainless steel and titanium junctions, where the two metals meet to form a bond. The beam flanges, coupling flanges, and RF flanges all have niobium and NbTi junctions in them, where the metals are bonded. Refer to figfure 6.26 and 6.27 below for the locations of these junctions on the SRF cavities. The samples were chosen because these metallic junctions are commonly found on SRF cavities at FRIB. An experimental trial with each of them would allow for a deeper insight into what metallic junction type contributes the highest or lowest to residual resistance through dynamic ambient magnetic fields. The materials each have their own magnitude of contribution, but understanding that magnitude, and the source is the focus of this investigation.

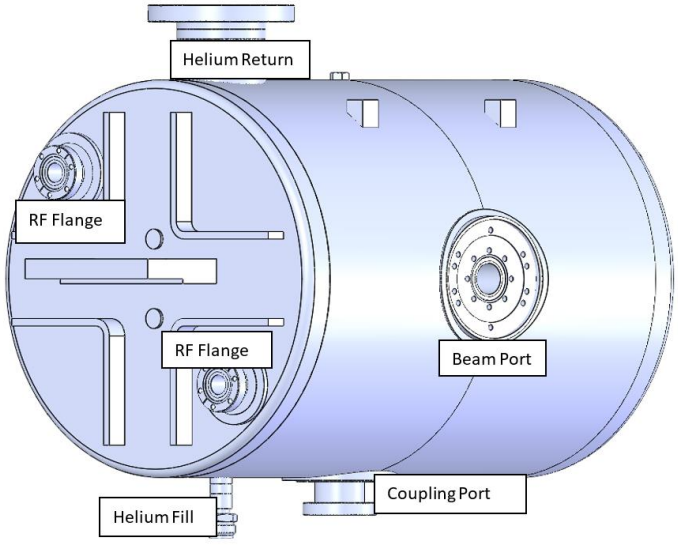

Figure 6.26 – Location of junctions on the SRF cavity (Side 1)

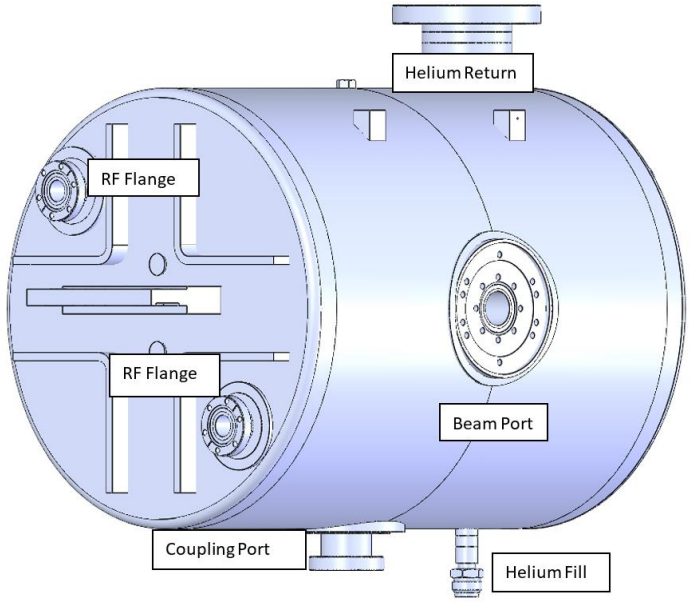

Figure 6.27 – Location of junctions on the SRF cavity (Side 2)

Each sample had a different method of preparation, with the two main joint methods investigated for this project being electron beam welding (EBW) and explosion bonding (EB). Explosion bonding is the process of producing a simple geometric gap between two flat plates of metal that have been spaced between each other. The two surfaces to be bonded are sanded and cleaned so that no defects or oxidation are present before the process can begin. A carefully measured mix of explosives is placed on the top of the top plate, slowly spread out to make a uniform surface. This uniform spread of explosives is key to the bonding process, due to the powderized nature of the explosives involved. When it has been spread thin all over the top of the plate, and the area has been cleared, the explosives are detonated, allowing for thw first metal to bond to the second metal almost instantaneously. Due to how fast the explosion occurs, no melting or shearing of metal takes place between the two plates. Once the dust settles, the two metals have been bonded effectively, with a virtually seemless weld. The sample of stainles steel bonded to titanium was bonded using the explosion bonding method. The two metals were annealed to one another, and a small portion of the large metal piece was cut off and prepared as a sample for the experiment.

Electron beam welding (EBW) is a process in which two metals are joined using a beam of high velocity electrons. The two metals are set at a small distance from each other, and are given a small gap for the weld to take place. The beam of electrons is emitted, and when they contact the metal, the metals quickly melt and fuse together. It should be noted that not all metals can be used in electron beam welding though, such as magnesium, lithium, and reactive metals of the same sort. Brass is not a good metal to electron beam weld, due to its composition involving zinc, which has a low melting point, and a reactive nature at higher temperatures. In general, metals should be welded using this method when they have similar thermal expansion coefficients, and similar melting points. Many metals can be joined using this method, with titanium and steel being some of the most popular materials. The disadvantages associated with this welding method involve setup cost and potential radiation effects from x-rays that are produced from the welding process.

6.6 Measurement of the Seebeck Coefficient

The results for measuring the seebeck coefficient are grouped by sample type, and are detailed below. The seebeck coefficients of each metal have been taken into account for these results. The raw data will be compared to expected theoretical values, and the temperature will be corrected based on equations 6.2 and 6.3. Each sample has copper wires welded to the ends to capture the voltage measurements.

$$48.124 + 0.083449x + 0.0044746x^2 + (-6.048 * 10^{-6})x^3 \quad (6.2)$$
(Best fit for T_1)

$$51.456 + 0.018375x + 0.004813x^2 + (-6.6085 * 10^{-6})x^3 \quad (6.3)$$
(Best fit for T_3)

$$0.56354 - 0.11688x + 0.012228x^2 - 0.00035526x^3 + (5.1739 * 10^{-6})x^4 - (4.2058 * 10^{-8})x^5 + (1.9151 * 10^{-10})x^6 - (4.545 * 10^{-13})x^7 + (4.3662 * 10^{-16})x^8 \quad (6.4)$$
(Niobium extrapolation equation of best fit)

$$10.548 - 0.56007x + 0.007866x^2 - (4.8367 * 10^{-5})x^3 + (1.4216 * 10^{-7})x^4 - (1.6153 * 10^{-10})x^5 \quad (6.5)$$
(Titanium extrapolation equation of best fit)

6.6.1 Niobium (Copper leads)

The first seebeck sample that was measured was a strip of Niobium metal, which had copper wires welded to each end so that the voltage could be taken. The copper wires had their seebeck coefficients calculated in reference to the niobium. By using the equation of best fit for niobium's seebeck coefficient (equation 6.4), one can use the average temperature of the sample at the cold and hot junctions and receive a Seebeck coefficient for niobium at that temperature (see equation 5.4). The seebeck coefficients for both niobium and copper are detailed in the tablkes below, for each average corrected temnperature. The theoretical calculations for the seebeck coefficients relies on the voltage from each experimental trial. The samples of data for each line were taken one hundred and twenty seconds apart from eqach other to acquire a wider selection of temperature ranges. This is so that, in subsequent trials, the seebeck coefficients for copper at the average temperature are already calculated. It is important to remember that calculations for the copper wires in the bi-metallic samples were not carried out, but only on the two metals involved in each bi-metallic sample. This is so that the data could be focused on the metals bonded within each sample, and not on the supporting connections. To note, it is important to consider all metals in a series for the Seebeck coefficient. For this particular set of trials, the copper coefficients have been calculated to set a precedent for their values at varying temperatures.

Trial 1 (Table 6.6)

Experimental Voltage (μV)	T_1* (K)	T_3* (K)	T_{ave}(K)	Δ T (K)	S(Nb) (μV/K)	S(Cu) (μV/K)
1.55	297.6796	305.7991	301.739388	8.1195142	46.46181	46.27091
3.97	279.4108	302.8004	291.105559	23.38961	16.48146	16.31173
5.74	256.3914	287.3727	271.882048	30.981205	-0.18984	-0.37511
6.51	234.1754	269.0506	251.612966	34.875198	-0.04234	-0.22901
6.23	212.0722	256.3891	234.230664	44.316965	1.328351	1.187772
5.34	188.5376	241.5124	215.025039	52.974784	1.282293	1.18149
3.62	163.3302	221.1767	192.253453	57.846487	0.454135	0.391555
0.367	132.5565	199.8487	166.202593	67.29225	0.649335	0.643881
-2.59	117.8931	178.1291	148.011123	60.236006	1.539319	1.582317
-4.31	109.4802	160.0186	134.749433	50.538379	2.23937	2.324651
-5.09	103.9997	144.7786	124.389178	40.778925	2.676402	2.801222
-5.3	100.275	132.7539	116.51448	32.478899	2.911081	3.074264
-5.18	97.28111	123.0341	110.157618	25.753008	3.036265	3.237407
-4.94	95.20675	116.8978	106.052281	21.691056	3.088885	3.316629
-4.62	93.33713	111.7432	102.540158	18.406066	3.118336	3.36934
-4.32	91.87414	107.983	99.9285517	16.108822	3.132029	3.400206
-3.98	90.81312	103.9262	97.3696739	13.113115	3.139502	3.443015
-3.75	89.89929	101.08	95.4896603	11.180736	3.14169	3.477088
-3.5	89.03112	99.06531	94.048214	10.034186	3.141685	3.490493
-3.28	88.45693	97.31545	92.8861927	8.8585155	3.140721	3.510986
-3.1	87.90318	95.66263	91.7829036	7.7594542	3.139078	3.53859
-2.96	87.58177	94.80539	91.1935808	7.2236192	3.13793	3.547697
-2.77	87.2407	93.854	90.5473483	6.6132983	3.136469	3.555322
-2.68	86.84185	93.03111	89.9364771	6.1892584	3.134901	3.56791
-2.55	86.48504	92.25979	89.3724171	5.7747532	3.133301	3.574879
-2.44	86.29065	91.75695	89.0237992	5.466292	3.132242	3.578614
-2.35	86.09009	91.18785	88.6389679	5.0977598	3.131013	3.592
-2.23	85.81119	90.60252	88.2068542	4.7913309	3.129561	3.594985
-2.17	85.75799	90.18436	87.9711718	4.4263698	3.128737	3.618981
-2.05	85.44596	89.90735	87.6766519	4.4613906	3.127678	3.587176
-2.02	85.24577	89.51674	87.3812584	4.2709721	3.126582	3.599542
-1.96	85.12631	89.3491	87.2377052	4.222795	3.126038	3.590186
-1.91	85.18349	89.22394	87.2037135	4.0404544	3.125908	3.598627
-1.88	85.05181	88.98889	87.0203513	3.9370769	3.1252	3.602712
-1.83	84.87342	88.7515	86.8124588	3.8780761	3.124383	3.596267
-1.81	84.87126	88.48462	86.6779381	3.6133638	3.123846	3.624765
-1.75	84.75733	88.42444	86.5908874	3.6671114	3.123496	3.60071
-1.7	84.57449	88.13513	86.3548116	3.5606397	3.122531	3.599974
-1.67	84.75301	88.28004	86.5165223	3.527028	3.123194	3.59668
-1.65	84.39203	88.11612	86.2540743	3.7240933	3.122114	3.565175
-1.6	84.26797	87.82708	86.0475233	3.5591136	3.121248	3.570799
-1.62	84.2608	87.50558	85.8831905	3.2447796	3.12055	3.619813
-1.6	84.21495	87.30832	85.7616372	3.0933677	3.120027	3.637263

Trial 2 (Table 6.7)

Experimental Voltage (μV)	T_1* (K)	T_3* (K)	T_{ave}(K)	Δ T (K)	S(Nb) (μV/K)	S(Cu) (μV/K)
8.07	307.6777	314.4609	311.0693	6.7831592	96.65126	95.46086
33.12	291.9219	311.6968	301.8093	19.774907	46.74043	45.06551
51.78	270.7464	302.6296	286.688	31.883142	9.588192	7.964105

61.75	247.8463	288.8578	268.3521	41.011527	-0.73275	-2.2385
63.09	225.9745	272.7121	249.3433	46.737625	0.189026	-1.16089
56.93	205.7824	256.2351	231.0088	50.452657	1.430467	0.30203
45.24	181.8544	238.1548	210.0046	56.30042	1.095438	0.291822
25.81	154.4937	219.4801	186.9869	64.986413	0.359409	-0.03777
-8.02	125.6269	198.5647	162.0958	72.937859	0.817394	0.92735
-36.17	111.8794	176.6508	144.2651	64.7714	1.744911	2.303403
-51.02	104.5288	157.3634	130.9461	52.834619	2.415086	3.380685
-56.55	99.89394	140.6068	120.2504	40.712895	2.810882	4.199892
-56.71	96.7552	127.4596	112.1074	30.704386	3.003747	4.850725
-54.11	94.47321	118.5544	106.5138	24.081182	3.08399	5.330775
-50.52	92.68862	112.1438	102.4162	19.455149	3.119136	5.715973
-46.72	91.06798	107.6449	99.35642	16.576879	3.134184	5.952646
-43.21	89.9624	104.1711	97.06675	14.208704	3.140034	6.181199
-40.04	88.90533	101.0883	94.99681	12.182953	3.141844	6.428008
-37.39	88.30492	99.04094	93.67293	10.736017	3.141464	6.624348
-35.35	87.64864	97.35548	92.50206	9.7068344	3.140226	6.781771
-34.37	87.23034	95.96278	91.59656	8.7324465	3.138735	7.074764
-33.27	86.84701	95.0883	90.96765	8.2412909	3.137443	7.173883
-30.46	86.40577	93.76405	90.08491	7.358283	3.135298	7.275225
-29.11	86.18592	92.95648	89.5712	6.7705561	3.133882	7.433525
-28.15	86.03161	92.40732	89.21946	6.3757057	3.132843	7.547827
-28.44	85.65968	91.69996	88.67982	6.0402825	3.131147	7.839236
-27.10	85.44596	91.22034	88.33315	5.7743871	3.129993	7.822808
-26.73	85.10099	90.56723	87.83411	5.4662404	3.128248	8.017448
-25.16	84.90229	90.19931	87.5508	5.2970268	3.127215	7.876878
-24.75	84.54358	89.55833	87.05095	5.0147552	3.125319	8.060356
-23.81	84.43294	89.19656	86.81475	4.7636195	3.124392	8.123618
-23.13	84.24862	88.78169	86.51515	4.5330693	3.123188	8.224968
-22.56	84.12691	88.51766	86.32228	4.3907536	3.122397	8.25975
-22.44	83.96536	88.22292	86.09414	4.2575614	3.121445	8.392258
-21.11	83.90326	88.02697	85.96511	4.1237171	3.120899	8.239846
-20.45	83.75922	87.83291	85.79607	4.0736877	3.120176	8.141277
-20.12	83.80412	87.74259	85.77335	3.9384727	3.120078	8.229277
-20.75	83.64104	87.54262	85.59183	3.9015784	3.11929	8.438875
-19.25	83.38884	87.2171	85.30297	3.828258	3.118014	8.145269
-18.67	83.3633	87.01111	85.18721	3.6478032	3.117496	8.236297
-18.26	83.28604	86.89135	85.0887	3.6053153	3.117052	8.182941
-18.24	83.11546	86.56254	84.839	3.4470856	3.115913	8.407287
-17.94	83.11546	86.59558	84.85552	3.4801252	3.115988	8.270918
-16.88	82.98545	86.2536	84.61952	3.2681533	3.114896	8.280511

Trial 3 (Table 6.8)

Experimental Voltage (μV)	T_1* (K)	T_3* (K)	T_{ave}(K)	Δ T (K)	S(Nb) (μV/K)	S(Cu) (μV/K)
10.09458	283.0513877	288.7419	285.8966	5.69048442	8.605676227	6.831735864
31.39244	263.4935602	286.0712	274.7824	22.5776538	0.619554082	-0.77086674
46.52792	242.2693064	274.5337	258.4015	32.2643853	-0.673079151	-2.1151621
52.32854	216.8356385	259.1017	237.9687	42.2660771	1.142775935	-0.09529828
47.46045	192.9505825	241.6192	217.2849	48.6686475	1.352949313	0.377774277
34.14336	164.9593568	223.2643	194.1119	58.3049907	0.502116503	-0.08348277
2.991683	130.9819675	202.759	166.8705	71.7770596	0.624771794	0.583091583
-29.8553	113.8862715	178.3086	146.0974	64.4223169	1.644551106	2.107981504

-48.1842	105.2829873	157.6099	131.4464	52.3269031	2.392900793	3.313730178
-55.6827	100.0346531	139.591	119.8128	39.5563522	2.823659729	4.231340087
-56.7957	96.50516229	127.4403	111.9727	30.935113	3.006156205	4.842117172
-54.649	94.11012466	119.1099	106.61	24.999761	3.082938506	5.268921007
-50.802	91.95547378	112.0636	102.0095	20.1081002	3.121652518	5.648097553
-46.4983	90.50151013	106.9882	98.74485	16.4866829	3.136171048	5.956525527
-42.6046	89.23633432	102.7335	95.98494	13.4972134	3.14136439	6.297912237
-39.639	88.33485705	99.54553	93.94019	11.2106713	3.141630595	6.677458094
-36.548	87.56840236	97.29144	92.42992	9.72303823	3.140123652	6.899026902
-34.5207	87.02629443	95.45773	91.24201	8.43143552	3.138031428	7.232321176
-32.2167	86.53351655	94.04033	90.28693	7.50681701	3.135822182	7.427486673
-30.4839	86.12299795	92.9165	89.51975	6.79349999	3.133733072	7.620942912
-28.9714	85.77838948	91.89688	88.83763	6.11848949	3.131655575	7.866704979
-27.8254	85.52658981	91.18785	88.35722	5.66125805	3.13007478	8.045127185
-26.6203	85.28345455	90.52669	87.90507	5.24324028	3.128502314	8.205578428
-25.4213	84.9817138	89.94762	87.46466	4.96590229	3.126894844	8.246069267
-24.6824	84.77174451	89.43289	87.10232	4.66114116	3.125518253	8.420865287
-23.9604	84.54070033	89.02212	86.78141	4.48141476	3.124259733	8.470881565
-22.905	84.37982896	88.80379	86.59181	4.42395906	3.123499244	8.300977085
-22.4117	84.25363547	88.52354	86.38859	4.26990088	3.122670452	8.371438667
-21.9281	84.07469455	88.16512	86.11991	4.09042308	3.121553445	8.482382772
-21.2461	83.87043474	87.79065	85.83054	3.92021754	3.120323994	8.539936504
-20.4384	83.88898401	87.55569	85.72234	3.66670749	3.11985734	8.693912547
-19.9688	83.67163638	87.3344	85.50302	3.66276677	3.118900181	8.570735158
-19.6235	83.55570405	87.09922	85.32746	3.54351988	3.118123256	8.655989754
-19.2903	83.51093769	86.90938	85.21016	3.39844102	3.117598871	8.793830962
-18.4213	83.40302608	86.66314	85.03308	3.26011054	3.116799446	8.767322575
-18.2029	83.36330344	86.44629	84.9048	3.08298359	3.116214467	9.020533922
-17.8332	83.25345318	86.32303	84.78824	3.06957883	3.115678805	8.92532598
-17.4272	83.19681167	86.18923	84.69302	2.99242144	3.115238255	8.939026904
-17.1244	83.22017172	86.16207	84.69112	2.94189845	3.115229431	8.936089774
-17.0508	83.06526608	85.88737	84.47632	2.82209924	3.11422594	9.156093549
-16.747	82.98333028	85.8304	84.40686	2.84706752	3.113898689	8.996091455
-16.5951	82.97909439	85.79552	84.38731	2.81643022	3.113806305	9.006063069
-16.1503	82.78376888	85.60931	84.19654	2.82554107	3.11289944	8.828735664
-15.6266	82.75208016	85.50572	84.1289	2.75364444	3.112575499	8.787447607

Where T_1* and T_3* are the temperatures at the top (cold side) and bottom (hot side) of the sample that have been corrected using Equations 6.2 and 6.3. T_{ave} is the average temperature between the corrected temperatures, T_1* and T_3*.

6.6.2 Stainless Steel – Titanium (Copper leads)

The second seebeck sample measured was a strip of bi-metal, of stainless steel explosion bonded to a piece of Titanium metal. The sample was noticeably shorter in length, and as such, the sample cooled down much faster than the other two. This gave rise to the results shown below, where the temperature levels out faster than in the two other cases. In addition, the seebeck coefficient for stainless steel, at temperatures below 300 K (room temperature), were unable to be located for verification of the calculation for theoretical voltage. In an effort to obtain results for the seebeck coefficient of stainless steel, the coefficients were calculated in reference to titanium. The titanium metal, using the extrapolation graph above, can have its Seebeck

coefficient calculated using a known temperature. In order to obtain this known temperature, the temperature calibration curves for T_1 and T_3 were used to correct for any error the sensors may have had. Once the Seebeck coefficient at a temperature was found, it was used to calculate a voltage based on the difference in temperature from T_1 to T_3. This voltage was used to calculate the Seebeck coefficient for stainless steel, by using the experimental voltage as a reference point. In order to receive the experimental voltage measured by the volt meter, the stainless steel part of the bi-metal had to have a corresponding Seebeck coefficient that would combine with the coefficient of titanium, to produce the experimental voltage in question. This relationship is illustrated by equation 5.2 in Chapter 5 of this paper.

Trial 1 (Table 6.9)

Experimental Voltage (μV)	T_1* (K)	T_3* (K)	T_{ave}(K)	Δ T (K)	S(Ti) (μV/K)	S(SS) (μV/K)
2.3	310.5415355	313.0078	311.7747	2.46630821	2.109152578	1.176584626
-0.6	293.9107042	302.8004	298.3555	8.88965957	3.674527715	3.742021863
-3.1	272.6477396	284.9543	278.801	12.3065767	4.479400598	4.731298431
-4.5	248.6771248	262.817	255.7471	14.1399006	4.173633693	4.49188204
-6.3	223.4876186	239.2937	231.3906	15.8060357	3.274596712	3.67317863
-9.2	203.7639495	216.5154	210.1397	12.7514572	2.406427541	3.127913709
-12.1	182.3945582	193.9425	188.1686	11.547991	1.545230938	2.593032237
-14.2	153.942739	167.1227	160.5327	13.1800099	0.446002224	1.523391401
-11.7	130.0420085	141.0957	135.5689	11.0537308	-0.700638102	0.357828057
-9.7	114.8936168	122.5146	118.7041	7.62095165	-1.578613935	-0.305807015
-7.5	105.0426066	110.1156	107.5791	5.07294854	-2.173997483	-0.695567347
-6.2	98.98703391	102.1412	100.5641	3.15415229	-2.537012703	-0.571349849
-4.9	95.12626354	97.16347	96.14487	2.03720885	-2.753569252	-0.348317571
-4.2	92.54908071	93.97275	93.26091	1.42366804	-2.887477311	0.062648626
-3.5	90.84609156	91.70528	91.27569	0.85918884	-2.975458441	1.098151253
-3.4	89.79672884	90.06927	89.933	0.27254409	-3.032758156	9.442287636
-2.7	88.76541528	88.99996	88.88269	0.23454826	-3.076229758	8.435260447
-3.2	88.19125206	88.34818	88.26972	0.15692699	-3.101020447	17.29062749
-3.6	87.79071321	87.81178	87.80125	0.02106541	-3.119667299	167.7765948
-3.2	87.38958481	87.29528	87.34243	-0.09430192	-3.137671054	-37.07123227
-2.1	87.06101023	86.81353	86.93727	-0.24747688	-3.153351633	-11.63899267
-2.9	86.86027645	86.56254	86.71141	-0.29773527	-3.16200252	-12.90219877
-1.8	86.58201757	86.36099	86.47151	-0.22102507	-3.171119185	-11.31499166
-1.7	86.36249286	86.0321	86.19729	-0.33039634	-3.181447526	-8.326783019
-2.1	86.15079761	85.71871	85.93476	-0.43208434	-3.191243046	-8.051405308
-1.8	85.7856772	85.51778	85.65173	-0.26789804	-3.2016994	-9.920673481
-1.4	85.60729417	85.05814	85.33272	-0.54915673	-3.213354464	-5.762717747
-1.2	85.32622828	84.86094	85.09359	-0.46528628	-3.221998903	-5.801056269
-1	85.07856608	84.5934	84.83598	-0.48517093	-3.231221588	-5.292350861

Trial 2 (Table 6.10)

Experimental Voltage (μV)	T_1* (K)	T_3* (K)	T_{ave}(K)	Δ T (K)	S(Ti) (μV/K)	S(SS) (μV/K)
-0.3	294.0501253	296.5559	295.303	2.5057662	3.897539745	4.017263602
-1.3	276.9513264	286.4084	281.6798	9.4570352	4.441409564	4.578873365
-4.1	251.3121517	264.6489	257.9805	13.336777	4.237260396	4.544680997
-5.7	222.9694809	237.6092	230.2894	14.63976	3.229575307	3.618925957
-7.9	198.5412147	210.991	204.7661	12.449794	2.192108826	2.826657456
-11.9	170.1354876	184.2851	177.2103	14.149652	1.12034029	1.961350402

-12.4	141.304976	154.4715	147.8882	13.166504	-0.110070838	0.831712969
-10.1	122.1063587	131.542	126.8242	9.435623	-1.148032215	-0.07762064
-7.5	109.2774447	115.82	112.5487	6.5425119	-1.909035796	-0.76268710
-6.3	101.2825944	105.4447	103.3636	4.1620634	-2.394362043	-0.88068977
-5.1	96.23150697	98.90295	97.56723	2.6714431	-2.685214869	-0.77613435
-3.4	93.02609718	94.75609	93.8911	1.729997	-2.858798889	-0.89347760
-4.2	90.85759688	92.01262	91.43511	1.1550279	-2.968532409	0.667743302
-2.8	89.48510512	90.27413	89.87962	0.7890243	-3.034997033	0.513689668
-0.7	88.51915482	89.04353	88.78134	0.5243785	-3.080358618	-1.74544510
-1.9	87.81155758	88.26319	88.03737	0.4516343	-3.110301429	1.096642028
-0.8	87.39773941	87.55569	87.47672	0.1579521	-3.132428727	1.932398157
-2.1	86.96280455	87.07827	87.02054	0.1154653	-3.150146015	15.0371406
-1.7	86.6614367	86.60061	86.63102	-0.060827	-3.165065589	-31.1131754

6.6.3 NbTi – Niobium (Copper leads)

The third Seebeck sample measured was a strip of bi-metal, of NbTi alloy welded using titanium filler to a piece of niobium metal. The method of calculation for the seebeck coefficient of NbTi was the same as the method for the stainless steel sample. The difference in the calculation came when the niobium metal, with a known extrapolation curve (shown above) was used to calculate the Seebeck coefficient of NbTi, as a reference material. The literature surrounding the Seebeck coefficient of NbTi was unable to be found for this temperature range, and as such, could not be validated with a relaible source. The following data is only experimentally gathered, due to the fact that theoretical calculations for the Seebeck coefficient of NbTi could not be achieved.

Trial 1 (Table 6.11)

Experimental Voltage (μV)	T_1* (K)	T_3* (K)	T_{ave}(K)	Δ T (K)	S(Nb) (μV/K)	S(NbTi) (μV/K)
2.3	301.9169406	309.0654	305.4912	7.148461056	63.30596007	62.9842125
-9.2	275.8793335	305.6065	290.7429	29.72713307	15.81659042	16.12607199
-48.2	249.3536807	302.9939	276.1738	53.64020503	1.151846241	2.050425954
-86.8	222.9694809	295.0727	259.0211	72.1032513	-0.71803428	0.485794929
-112.2	198.8523116	282.1801	240.5162	83.32776716	0.975571766	2.322061704
-128.5	173.2483985	267.1165	220.1825	93.86811997	1.425454061	2.794395934
-140.3	139.1526989	252.4412	195.797	113.2885415	0.551422403	1.789853034
-150.6	118.0503449	234.9888	176.5196	116.9384146	0.37475203	1.662609407
-151.2	107.6466174	218.2206	162.9336	110.5739659	0.780890191	2.148300673
-144.9	102.0872459	202.5965	152.3419	100.5092114	1.303085671	2.744744579
-133.6	98.71617426	189.3139	144.015	90.5976878	1.758546139	3.23319746
-121.5	96.36825854	178.0843	137.2263	81.71601127	2.117002221	3.603858935
-110.5	94.60718253	168.133	131.3701	73.52585835	2.396304379	3.899177007
-101.1	93.03235633	159.1782	126.1053	66.1458205	2.613543493	4.141984734
-92.3	91.91983477	152.4682	122.194	60.54833804	2.75078229	4.275184164
-84.4	90.9113048	145.6159	118.2636	54.7046008	2.866675667	4.409507509
-77.6	90.00195747	139.936	114.969	49.93401715	2.946675993	4.500726807
-71.1	89.27863553	134.8071	112.0429	45.52844468	3.004904581	4.566565659
-65.6	88.5521546	130.5122	109.5322	41.9600488	3.045640356	4.609032247
-60.6	87.64046769	126.2366	106.9385	38.5961216	3.079264344	4.64937029
-55.2	87.05288412	122.7978	104.9253	35.74491253	3.099808817	4.644084522
-50.6	86.56658272	119.6298	103.0982	33.06323491	3.114539401	4.644940166
-41.7	86.183729	116.733	101.4584	30.54924365	3.124802389	4.489811634
-40.9	85.72302166	114.1162	99.9196	28.39316462	3.132065429	4.572552974
-38.1	85.26606084	111.7432	98.50463	26.47713061	3.136864721	4.575842402

-36.1	85.02651309	109.8342	97.43035	24.8076724	3.139387488	4.594582454
-33.2	84.67306348	107.6275	96.1503	22.9544762	3.141216809	4.587557807
-31.3	84.38700448	105.7606	95.0738	21.37358184	3.14183092	4.606255565
-29.2	84.11975321	104.1627	94.1412	20.04290017	3.141726686	4.598601676
-27.6	83.8961194	102.8674	93.38176	18.97128579	3.141231905	4.596062132
-26.1	83.55357179	101.1957	92.37462	17.64209487	3.140043279	4.619459426
-24.3	83.2902904	99.81495	91.55262	16.52466065	3.13865102	4.609180462
-23	83.0765738	98.70031	90.88844	15.62373727	3.137266118	4.609385088
-22	82.94027525	97.68422	90.31225	14.74394901	3.135886489	4.628024042
-20.6	82.73377659	96.66098	89.69738	13.92720195	3.134240654	4.613360442
-19.4	82.56852209	95.59954	89.08403	13.03102176	3.13242911	4.621184202
-18.3	82.59381644	94.96282	88.77832	12.36900249	3.131465543	4.610970459
-17.6	82.41551493	94.11807	88.26679	11.7025556	3.129766757	4.633711758
-16.6	82.21171123	93.37647	87.79409	11.16475801	3.128104161	4.61492546
(No data)	82.10895027	92.69687	87.40291	10.58791942	3.126663629	3.126663629
-14.1	82.06634573	92.11935	87.09285	10.05300574	3.125481652	4.528047248
-13.3	81.91078335	91.40343	86.65711	9.492646135	3.123762556	4.524847123
-13	81.71309743	90.80928	86.26119	9.096179942	3.122143794	4.55131517
-12.4	81.595689	90.25392	85.92481	8.65823414	3.12072747	4.552890172

Trial 2 (Table 6.12)

Experimental Voltage (μV)	T_1* (K)	T_3* (K)	T_{ave}(K)	Δ T (K)	S(Nb) (μV/K)	S(NbTi) (μV/K)
4.6	305.9952276	314.9406	310.4679	8.945369389	92.51158913	91.9973566
-33.6	280.6566412	311.2254	295.941	30.56874113	27.36282353	28.46198557
-55.4	250.5406355	305.6518	278.0962	55.11117244	2.067539484	3.072780301
-95.4	220.3342537	294.2437	257.289	73.90944089	-0.58475221	0.706016576
-124.7	191.11137	281.4679	236.2896	90.35650491	1.235078827	2.615167622
-135.6	157.0470899	267.5294	212.2883	110.4823554	1.184346997	2.411692301
-154.8	127.620826	248.5618	188.0913	120.9409588	0.373893311	1.653856705
-159.2	112.7945252	229.9662	171.3804	117.1716575	0.482151443	1.84084179
-154	105.3345473	213.7444	159.5395	108.4098874	0.934898276	2.355432913
-142.4	100.9070137	199.085	149.996	98.17801025	1.430422507	2.880849131
-131.5	97.9069728	186.0556	141.9813	88.14859012	1.868600317	3.360399559
-120.1	95.90232156	175.5782	135.7403	79.67587968	2.191099966	3.69845703
-108.2	94.26661223	166.0709	130.1688	71.80432886	2.448959014	3.955831953
-99.5	92.80724556	157.6099	125.2086	64.80264488	2.64689748	4.182328637
-90.6	91.60192209	150.7917	121.1968	59.18979686	2.782296748	4.312965965
-83.8	90.63385006	144.5104	117.5721	53.87652431	2.88475669	4.440165118
-77.4	89.84533893	139.0238	114.4345	49.17841523	2.958198219	4.532059427
-71.3	89.00097766	133.9421	111.4715	44.94113273	3.01490709	4.601426959
-65.7	88.36180614	129.7209	109.0413	41.3590554	3.052646844	4.641174419
-61.3	87.68878877	125.7857	106.7373	38.0969235	3.081530586	4.690584398
-57.6	87.09499958	122.1375	104.6163	35.04254644	3.10255504	4.746271203
-53.6	86.63863364	118.9523	102.7955	32.31369671	3.116638397	4.775377739
-49.1	86.23717579	116.1937	101.2155	29.95655364	3.126096855	4.765137199
-45	85.72302166	113.6569	99.68995	27.93385795	3.132963146	4.743911411
-41.4	85.36321841	111.4501	98.40664	26.08684219	3.137133824	4.724140779
-38.7	85.15091179	109.2905	97.22069	24.13956218	3.139772534	4.742949912
-36.4	84.84456468	107.4804	96.16249	22.63585306	3.141205148	4.749273547
-35	84.36547968	105.5641	94.9648	21.19863591	3.141848425	4.792898056
-32.9	84.11975321	103.7997	93.95975	19.67999141	3.141641061	4.813389758
-31.5	83.85117623	102.1412	92.99618	18.29000997	3.140846587	4.863098246

-30.3	83.69512635	101.08	92.38758	17.38490173	3.140062265	4.882953911
-27.8	83.4690348	99.70874	91.58889	16.2397096	3.138720093	4.850573364
-25.7	83.28391358	98.55462	90.91927	15.27070894	3.137335341	4.820295844

6.7 Measurement of the magnetic Seebeck contribution

The measurement of the magnetic contribution of the seebeck coefficient for each sample is shown below. A preliminary test was performed in order to understand the magnitude of current running through the metallic sample, so as to compare that result with actual data received from the Seebeck circuit. The test consisted of a current source (Keysight E36312A current source), the metallic sample, and wires that connected the two ends of the sample to the source. Magnetic probes (Bartington Mag 01H Fluxgate Magnetometers) were used for the measurement of the magnetic field generated by the current being run through the metallic sample. What this test does is run a preset current range through the metallic sample used, and through monitoring of the magnetic field, a relationship between the amount of current and the magnitude of the magnetic field could be obtained. Current was driven through the sample from 1 to 30 mA. To experimentally measure the magnetic field, a short between the voltage input leads was created in hopes of creating a simple circuit that would allow for current generation. Current generation from the sample would then create a magnetic field, which could be compared to the experimentally determined current mapping performed prior. An additional test was performed for each sample, in which the probes for each location on the sample were switched with one another to ascertain if the magnetic field measured was consistent across the probes. This, also, could be compared to a theoretical current mapping produced by calculating the expected magnetic field using equations 5.4, 5.5, and 5.6 from Chapter 5. Below, each sample's graph is shown.

6.7.1 Niobium

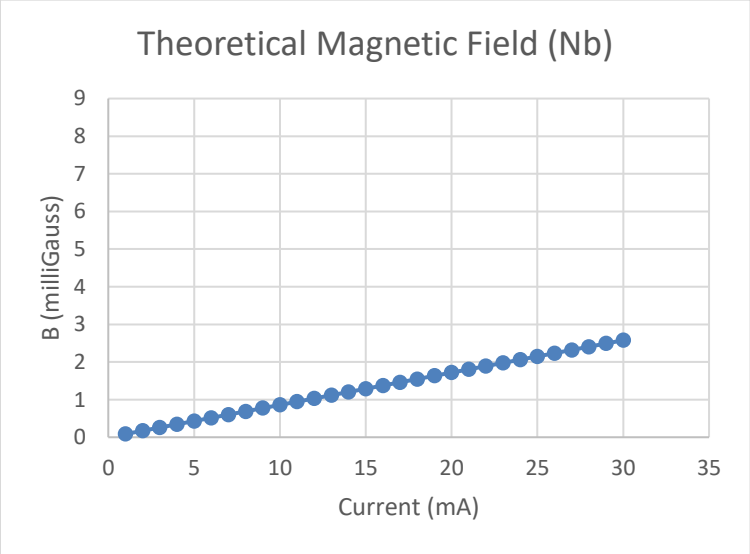

Figure 6.28 – Theoretical magnetic field calculation of the Nb sample

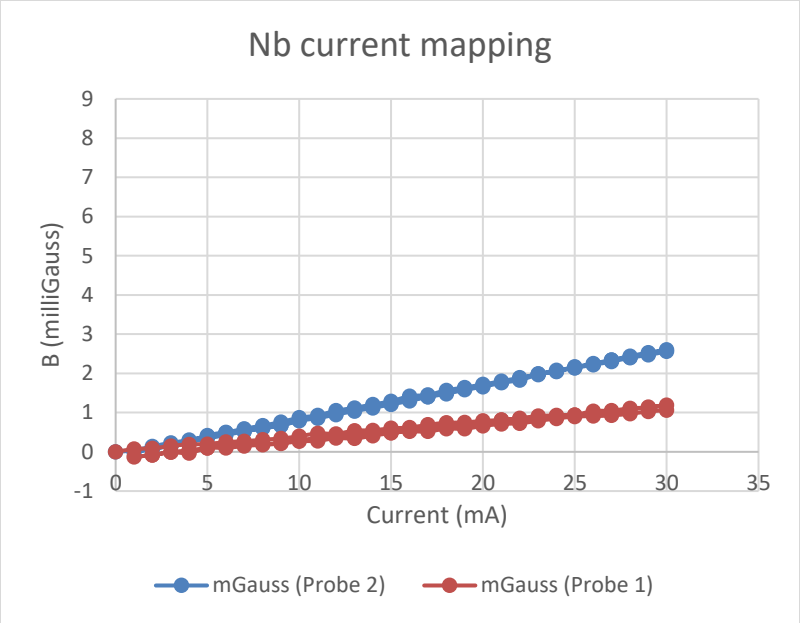

Figure 6.29 – Current mapping of the Nb sample (initial run)

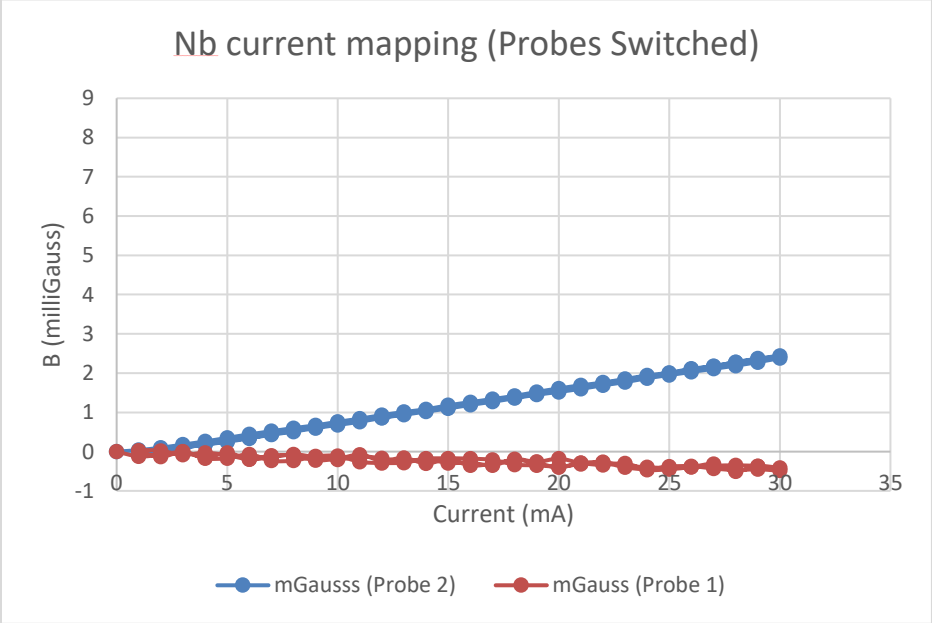

Figure 6.30 – Current mapping of the Nb sample (probe locations switched)

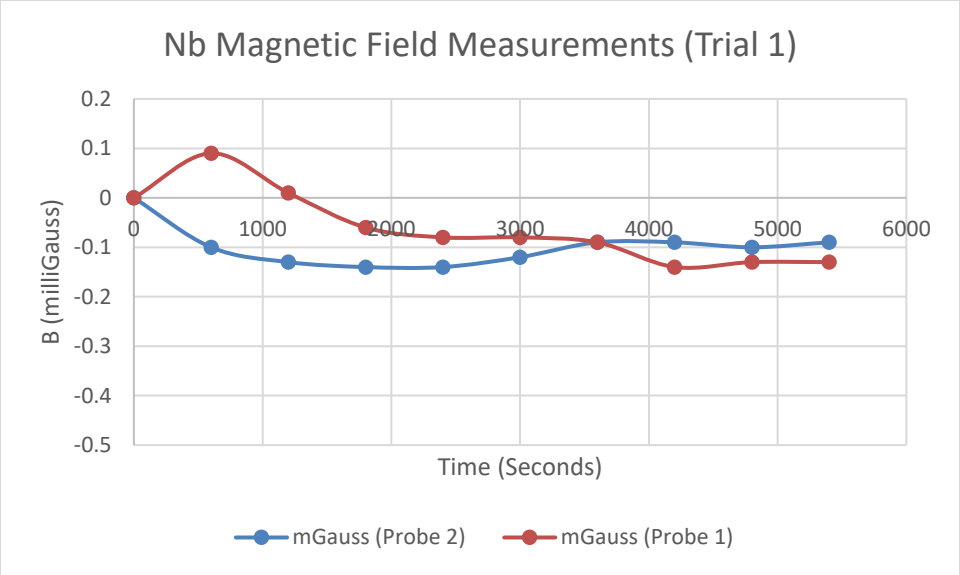

Figure 6.31 – Experimental field measurements for Nb (First trial)

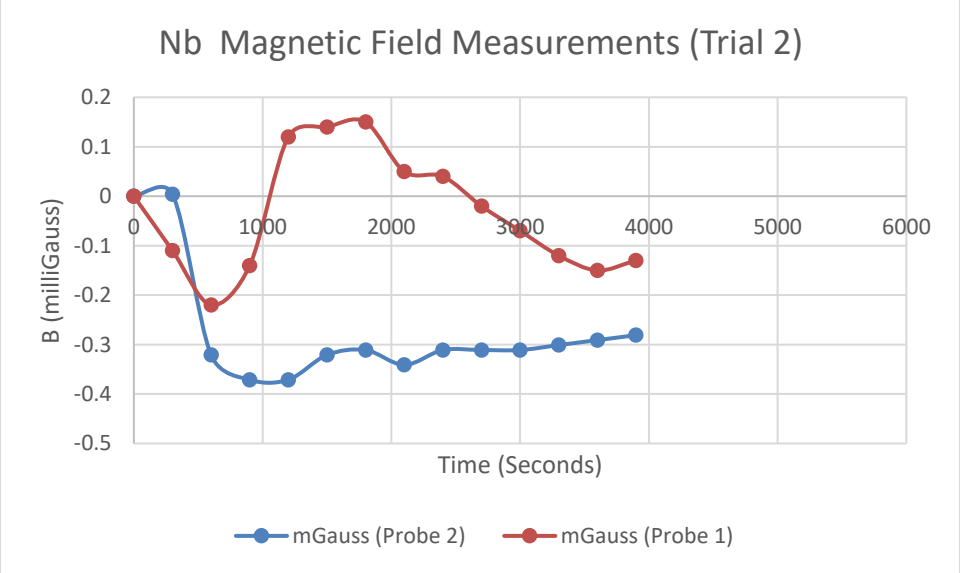

Figure 6.32 – Experimental field measurements for Nb (Second Trial)

6.7.2 Stainless Steel – Titanium

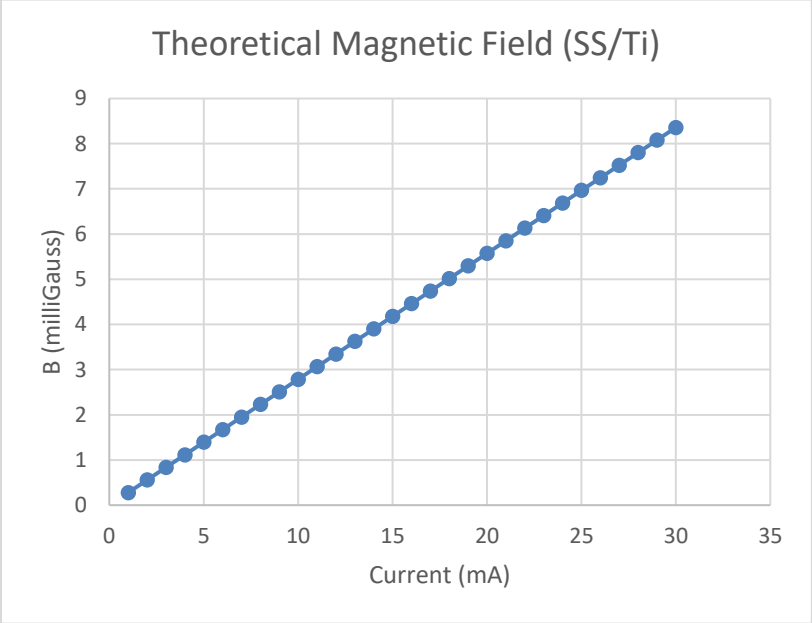

Figure 6.33 - Theoretical magnetic field calculation of the SS/Ti sample

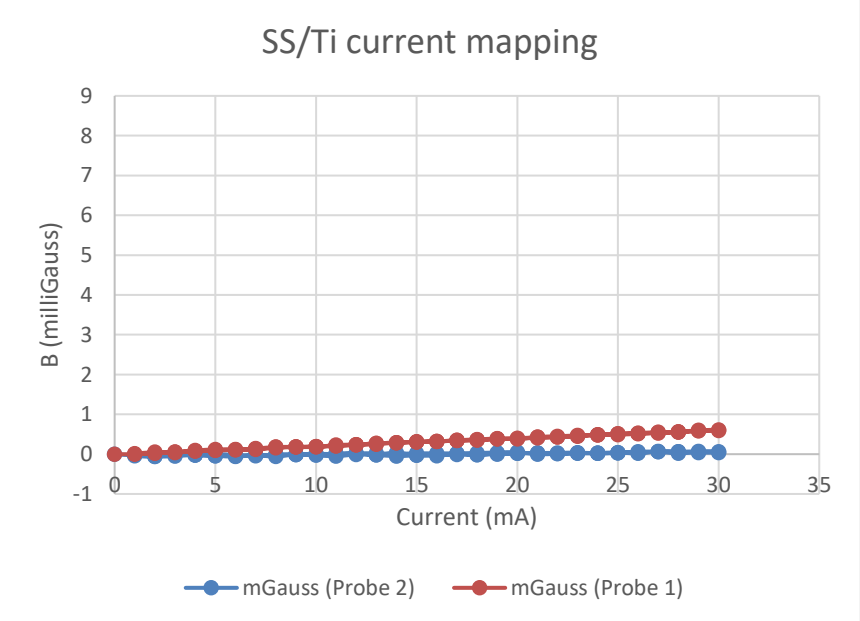

Figure 6.34 – Current mapping of the SS/Ti sample (initial run)

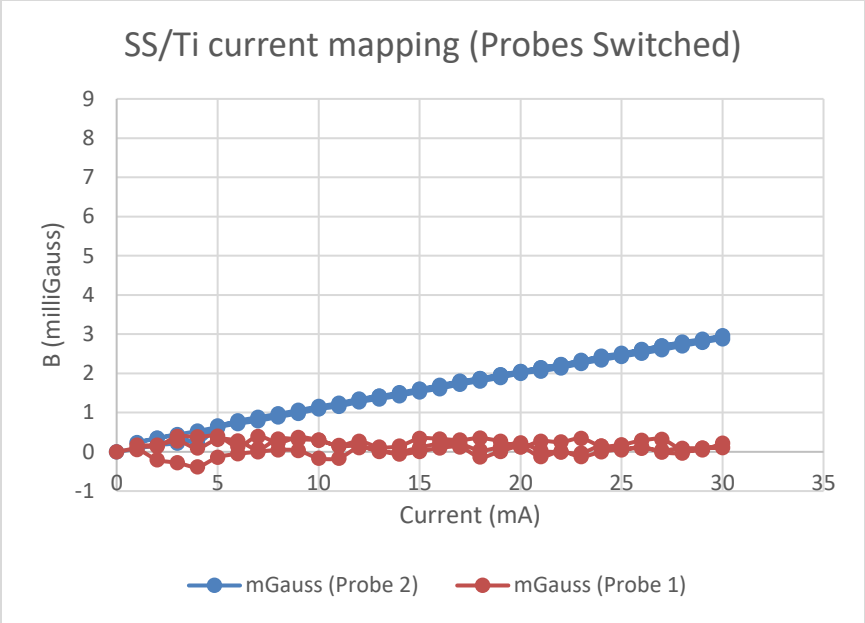

Figure 6.35 – Current mapping of the SS/Ti sample (probe locations switched)

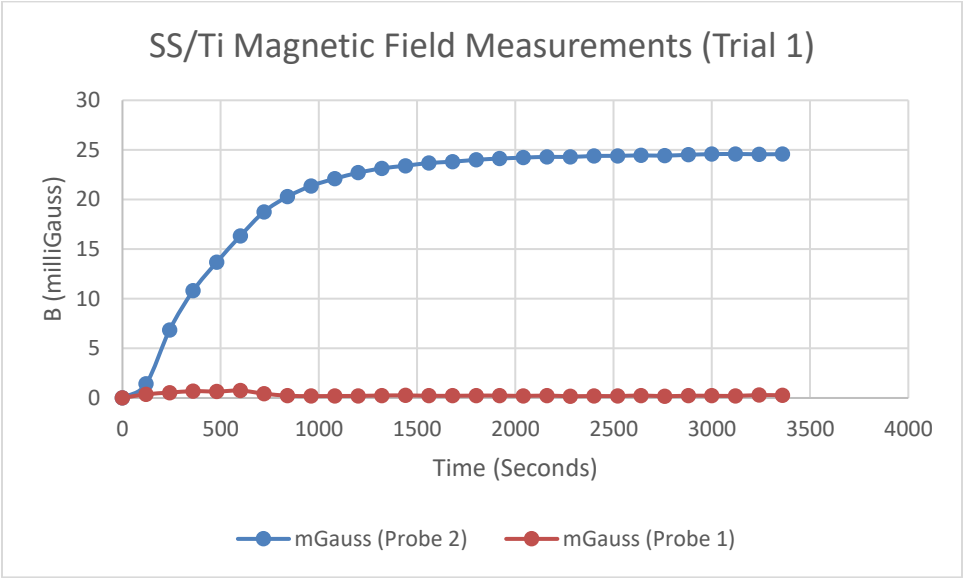

Figure 6.36 – Experimental Field Measurements for SS/Ti (Trial 1)

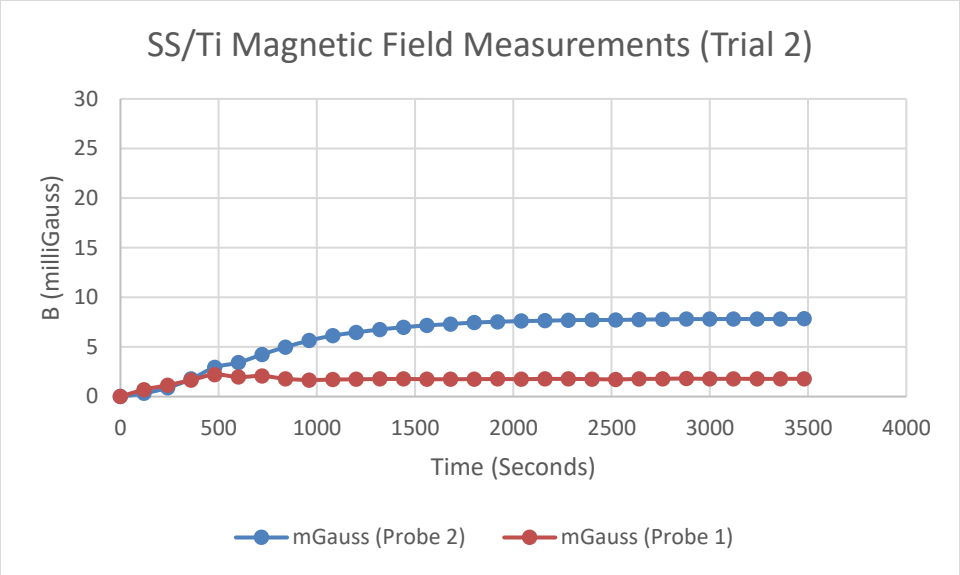

Figure 6.37 – Experimental Field Measurements for SS/Ti (Trial 2)

6.7.3 Niobium – NbTi

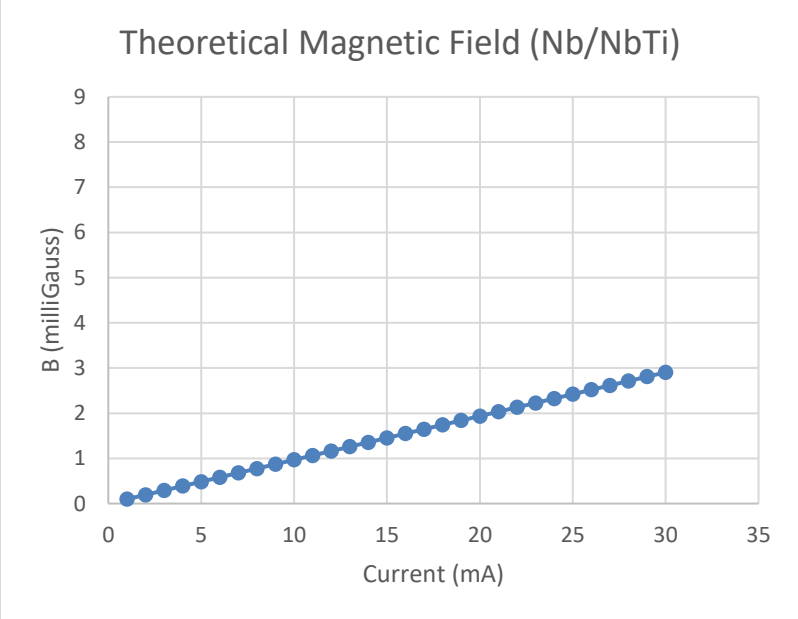

Figure 6.38 – Theoretical magnetic field calculation of the Nb/NbTi sample

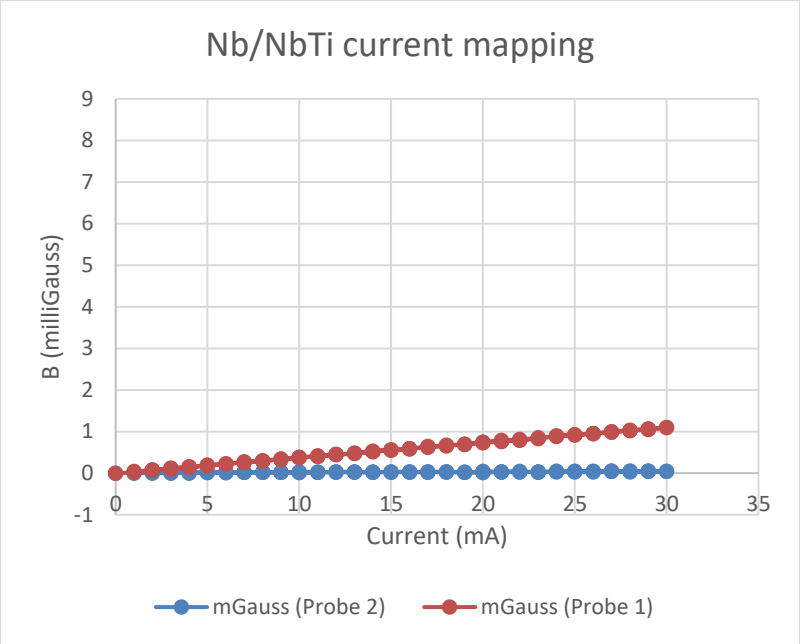

Figure 6.39 – Current mapping of the Nb /NbTi sample (initial run)

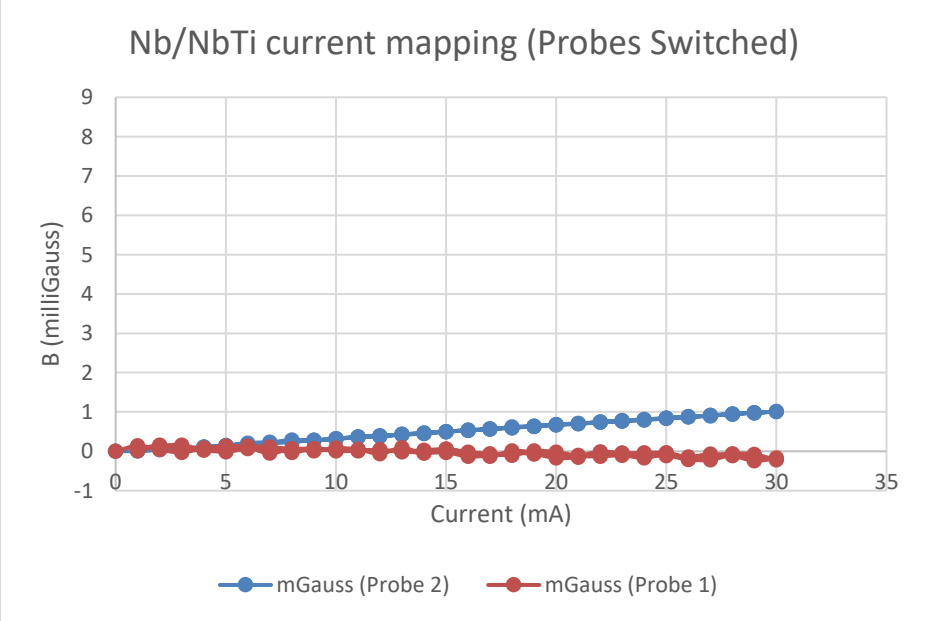

Figure 6.40 – Current mapping of the Nb /NbTi sample (probe locations switched)

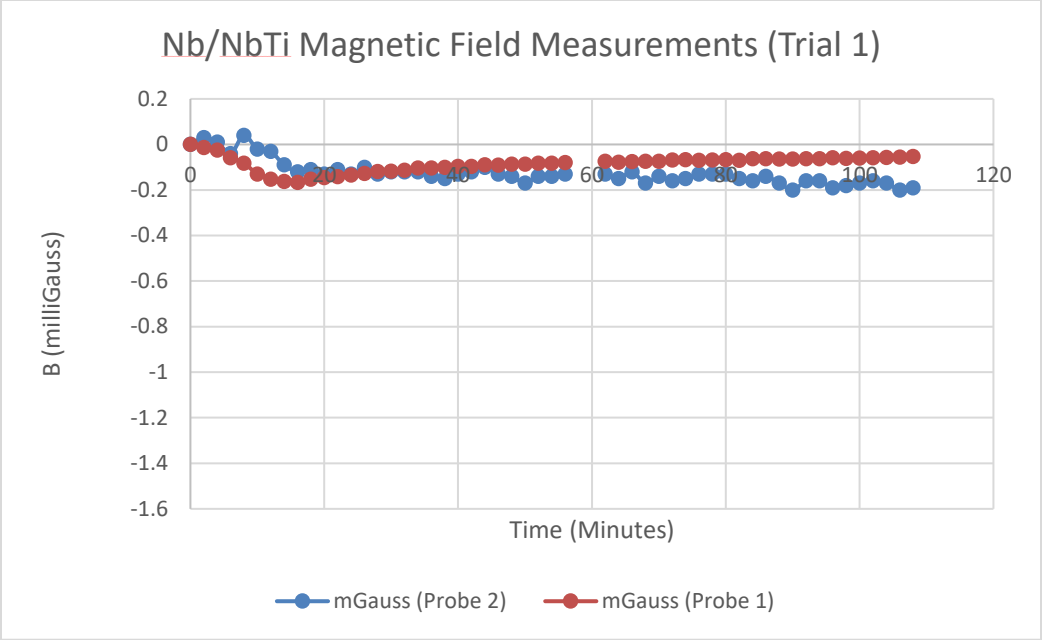

Figure 6.41 – Experimental field measurements for Nb/NbTi (First Trial)

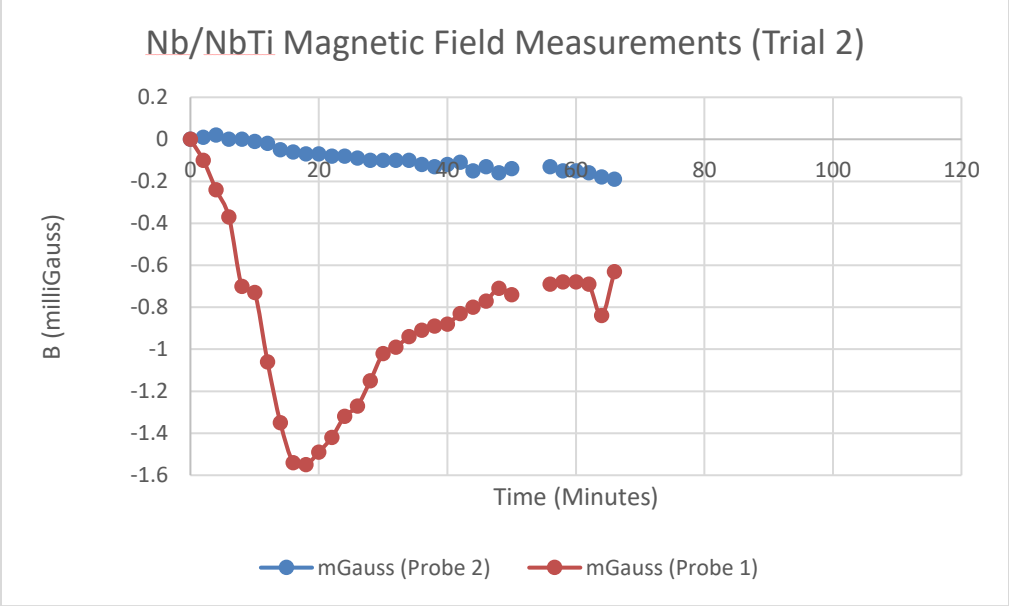

Figure 6.42 – Experimental field measurements for Nb/NbTi (Second Trial)

Bibliography:

[6.1] Takehisa Fukui, Junichi Tatami, Shuji Sakaguchi, Fumihiro Wakai, Tetsuya Senda, Takashi Akatsu, Tetsuya Baba, Yuji Noguchi, Masaru Miyayama, Atsushi Yamamoto, Susumu Yonezawa, Tomoichiro Okamoto, Motohide Matsuda, Masanobu Awano, Tsutomu Katamoto, Kenji Toda, Soshu Kirihara, Akihiko Suda, Kiyoshi Nogi, CHAPTER 6 - EVALUATION METHODS FOR PROPERTIES OF NANOSTRUCTURED BODY, Editor(s): Masuo Hosokawa, Kiyoshi Nogi, Mario Naito, Toyokazu Yokoyama, Nanoparticle Technology Handbook, Elsevier, 2008, Pages 317-383, ISBN 9780444531223, https://doi.org/10.1016/B978-044453122-3.50009-X,
https://www.sciencedirect.com/science/article/pii/B978044453122350009X

[6.2] J. Corcoran, S. Raja, P.B. Nagy, Improved thermoelectric power measurements using a four-point technique, NDT & E International, Volume 94, 2018, Pages 92-100, ISSN 0963-8695, https://doi.org/10.1016/j.ndteint.2017.12.002,
https://www.sciencedirect.com/science/article/pii/S0963869517302190

[6.3] Blatt, F. J., Schroeder, P. A., Foiles, C. L., & Greig, D. (1976). Thermoelectric Power of Metals. In Springer eBooks. Springer Nature. https://doi.org/10.1007/978-1-4613-4268-7

7. Discussion

In this Chapter, the discussion over the results found in Chapter 6 will start with the understanding of the experimental data. To validate the experimental data, sources have been used in Chapter 6 to reference appropriate values for Seebeck coefficients. For the magnetic contribution of the Seebeck effect, there is literature on the subject, but none so specific as to characterize the metallic samples used in this paper. In order to better serve the general scientific body reading this thesis, magnetic measurements will be explained as thoroughly as possible. The discrepancies in these experiments will be discussed as well, regarding data matching over the trials conducted in this thesis, and whether this data confirms or disproves the abstract at the beginning of this paper. The discussion of the data measured in Chapter 6 will serve as a basis for future results to come, and at the end of this Chapter, recommendations are made as to the proposed solution for dealing with the thermoelectric current effects, and the magnetic field generated by the current.

7.1 Comparison between existing results and experimental data for voltage generation

In this section, each sample will be discussed separately, with commentary on the implications for each sample's direct experimental results. The data taken for each sample, both theoretical and experimental, will be compared to one another, and conclusions will be drawn from the comparison. It is unknown if the voltage from the Seebeck effect alone will have an effect on the cavity, but in a closed circuit, it should generate a current and resulting magnetic field. Both of these are discussed at length in the next section.

7.1.1 Niobium

The niobium sample was the first one on which testing was conducted, and was a single metal sample to serve as a baseline for the rest of the experimentation. Niobium was chosen because it is the metal that the cavities are constructed from, meaning that experimentation performed on the sample would better inform the scientific body concerned with the use of the metal. Niobium generated a large voltage peak when cooled down from room temperature to roughly 77 K (liquid nitrogen temperature). The voltage had a maximum and a minimum during its cool down, corresponding to an increase in voltage measured, then a decrease, before it slowly attempted to reach an equilibrium below 0 μV/K. Niobium had a known range of Seebeck coefficients (see source 6.4), and from that, an extrapolation graph was obtained. Using this graph, and the temperature at which the material was cooled down to, it was simple to obtain an extrapolated Seebeck coefficient value. The validity of these values could not be ascertained, however, the voltage generated by the sample could be verified through these values and the difference in temperature generated between each end. The first trial had appreciably low error, though the second and third trials had greater discrepancy in their calculations. The voltage generated means that at low temperatures, there is a voltage that is generated by the singular metal sample itself, lending credence to the idea that two metals would generate one as well. The magnitude of the voltage generated relates to the amount of current it may produce, as well as the capability of the metal to have electrons flow from end to end. The higher the difference in temperature, the higher the error may be in the Seebeck voltage generated, as well as the magnitude of that voltage. For the results of this sample, it is safe to assume that Niobium is able to generate a Seebeck effect, and thereby, a seebeck current, the magnitude of which will be detailed in the next section of this chapter. The error in the calculations was at highest in the 19-20 percent

range, and the lowest was around 5%. An interpretation of this is that most of the data was somewhat off the expected values, but some of the results stayed within an acceptable range. It is safe to say that there was confirmation for the Seebeck coefficients of niobium, but it is important not to ignore the majority of the results having over 10% error.

7.1.2 Stainless steel – Titanium

Stainless steel is a metal that is joined with titanium in FRIB cryomodules, and for FRIB β = 0.53 HWRs. The locations at which they are joines are mainly in the helium filling and helium return ports on the cryomodule. For the material of stainless steel, it was not possible to find accepted values for the Seebeck coefficient. This made calculations difficult, though not impossible. Using the known Seebeck values for titanium at lower temperatures, another extrapolation graph was procured. Through the reference material of titanium, it was possible to obtain a range of Seebeck coefficient values for stainless steel, though there is no easy way to verify them. It would seem that the Seebeck coefficient of stainless steel is unknown at lower temperatures, and for the purpose of this thesis, lower temperatures refers to below room temperature. Due to the large variety of steel alloys, and types of steel, it could be an entire research paper in and of itself for the verification of steel Seebeck coefficients. For the use of this paper, it should be suffice to say that, in reference to titanium, stainless steel has a Seebeck value of around 4μV/K at around room temperature, and lower than that below room temperature. As for the voltage generated by the sample overall, the maximum was much lower than in the other samples, most likely due to the small size of the sample. In addition, the voltage curve had a minimum at around 12-14 μV, but slowly leveled out higher than that for both trials. Only one point of curvature in the graph implies that the sample could not have produced the same curve as in niobium, or in the next sample of niobium and NbTi. The sample size, namely the thickness, and the length, are dissimilar to the other two samples, and as such, led to this result.

7.1.3 NbTi – Niobium

NbTi is an alloy metal that is often used in cryomodules for a variety of purposes, and in the case of FRIB β = 0.53 HWRs, are used as part of a metallic joint that connects to niobium in the cryomodule. As discussed in Chapter 6, the joints that use this metallic junction are the beam flanges, coupling flanges, and RF flanges. For the purposes of this thesis, the NbTi alloy had its Seebeck coefficient found in reference to niobium in a method similar to the SS/Ti sample. The differences between this sample and the SS/Ti sample are its physical dimensions, and metallic composition. The sample is similar in length, width, and thickness to the pure niobium sample, which allowed for a decent comparison of its generated voltage. The Nb/NbTi sample generated the largest voltage out of all of the samples, at more than 150 μV in magnitude. The curve for this voltage was similar to the SS/Ti sample in that it had one peak, not two. In this way, bi-metal samples seem to only have one peak, whereas single metal samples may have two peaks on their voltage curves. The double peak for single metals has yet to be validated due to the small number of samples used during this thesis. Upon close inspection, it seems as if the Nb/NbTi sample is one to monitor in the case of cavity and cryomodule testing. At the very least, the voltage generated by the temperature difference is significant enough to be picked up on high sensitivity voltage meters. It is advisable to use caution when cooling down with these joints, especially around high sensitivity electronics and sensors.

7.2 Magnetic flux trapping and the Seebeck thermoelectric effect

Magnetic flux produced by the Seebeck effect is discussed in this section, specifically, it is discussed with regard to the general approach that was taken to measure the flux, as well as the direct results. Each sample obtained a different set of measurements, and in this section, they are each discussed at length. The purpose of this section is to draw conclusions from the magnetic measurements made, as well as to discuss the effect each metal sample may have in a cavity.

7.2.1 Magnetic flux calibration mapping

The flux mapping, as seen in Chapter 6 section 7, is a process by which a known current is passed through each sample, and the resulting magnetic field is measured. Once the full range of current has been measured, a profile for each sample can be used to compare with experimental measurements during cool down. This is so that, in comparison, it is relatively simple to determine the magnitude of current produced by each metal sample. The sample, when it is being measured, is shorted from each end using a wire, which allows it to complete a circuit, and generate current from the cooling of one end of the metal. In an ideal Seebeck circuit, one end is heated, while the other end is cooled, though in this paper, there was no heating element used.

7.2.1.1 Niobium

The niobium cool down experiment sample saw a small magnetic flux, on the order of a tenth of a milliGauss (mG). This is in line with the current mapping that was performed on the sample, matching around 0.2 mG in magnitude for the current range of roughly 3 mA. The current mapping of the niobium sample produced a maximum field of around 2.5 mG. On the second trial, the magnetic field seemed to be higher in magnitude, but it still did not surpass an order of ten greater in value. The reason for this jump in field from one measurement to another is not known, and requires further experimentation to characterize properly. The magnitude of this field alone should pose no issue to the cavity. The reason that this result stands out, is that it proves a single metal is not capable of producing a problematic magnetic field. This being said, a tenth of a mG does mean it can be measured on a sensitive hall probe. The impact of this metal alone in the cavity should be relatively low, and unpronounced. It is for this reason that niobium alone lends no major contribution through the Seebeck effect to residual resistance. Further study, and experimentation should be implemented to better understand the full range of niobium's thermoelectric potential.

7.2.1.2 Stainless Steel / Titanium

The second sample, stainless steel and titanium, had the largest theoretical field calculated from 1 to 30 mA. The magnitude of this field would reach, in theory, around 9 milligauss. This alone would be reason enough to count it as a major contributor of residual resistance inside of the cavity. The current mapping from 1 to 30 mA of the sample yielded smaller results in magnitude on the first trial, of not even one mG. When the probes were switched, the magnitude of the field measured was around 3 mG, which seems to indicate that either one probe is faulty, or that edge effects contribute to a different field on the sample. The reason for this difference in magnitude from theoretical to physical can be attributed to the cross sectional area, and the length of the sample (current path). Due to its small size, the cool down of the sample took a shorter amount of time, and the magnetic field measured surpassed expectations. The first trial saw magnetic fields in magnitude of nearly 25 mG, whereas the second trial saw a magnitude of roughly 7-8

mG. The graphs, as seen in Chapter 6 in section 7, show a curve that grows rapidly, and levels off after roughly 30 minutes of measurements. The magnetic field generated by this sample is strong enough to account for the losses seen earlier in this paper. The current generated by this sample, if judged by the theoretical calculations, should be anywhere between 80-90 mA. If judged by the current mapping results, at least the one where the probes were switched, the current should be around 0.25 A.

7.2.1.3 Niobium / NbTi

The third sample, niobium and the NbTi alloy, had a theoretical maximum of roughly 3 mG from calculations along the current path. These calculations are for the current range of 1 to 30 mA, which were compared to the current mappings shortly after. The first current mapping showed that its maximum field was close to 1 mG in magnitude at 30 mA. The current mapping where the probes were switched also reflected this magnitude, which confirmed the first current mapping. The cool down trials for the sample went a bit differently, where the first trial had a magnitude at the largest of around 0.2 mG, which differed from the second trial. The second cool down trial showed a magnetic field of around 1.6 mG in magnitude. The exact cause for this jump in field is unknown between the two trials, since they were carried out in the same exact manner. The current that would have been generated by the sample to achieve this field should have been roughly 45 mA if the current mappings were to be used. The current would be 15 mA if it were compared to the theoretical calculations.

7.2.2 Generation of a current by the Seebeck effect

A thermoelectric current is generated inside of a circuit that is closed, and when the Seebeck effect is active within the circuit. This means that, in essence, one end of the circuit is being heated, while the other end is being cooled. At each of these junctions, the two metals in the circuit that comprise the Seebeck effect are joined. When they are joined, the electrons in each of them start moving from the temperature differential, and start flowing in the circuit. The Seebeck effect, in this way, can generate current when more of these metals are joined in a series, such as described in Chapter 5. For the purposes of this paper, the generation of the current inside of a cavity is the primary assumption. For current to be generated, there must be a closed loop of metals that are not insulated from one another, which causes the current to flow through, essentially, the entire cavity, and the cromodule. The far-reaching effects of this are not yet fully understood, but to encapsulate the point being illustrated here, a generated current loop inside of an SRF cavity is not ideal, especially when it generates magnetic fields that become trapped during cool down.

7.2.3 Conclusions and future notes

Each sample generated its own magnetic flux, even the single metal sample that was used. The Seebeck effect is not an effect that only affects a single group of metals. The Seebeck effect occurs when any metal has opposite ends cooled down and heated. The metals tested were only a few examples of what may be possible inside of a cryomodule that undergoes conventional cool down processes. In the future, additional samples of metal junctions must be tested in order to fully characterize the magnetic field inside of a cryomodule. This research must also be validated with repeated trials, and better-known Seebeck coefficients. Metals that may aid in this process are platinum, and lead. In order to fully explore the characteristics of stainless steel and NbTi, lower temperatures should be achieved with cool downs. This research is limited by the extent to

which the assembly can be cooled down, and hold its temperature gradient steady. The improvement of the measurement apparatus would also benefit this research.

7.3 Elimination of the thermoelectric current

The thermoelectric current is something that must be removed from the cavity, or at the very least, cut so that it cannot form a complete circuit. The methods for implementing this cut, and future recommendations for cryomodules regarding the research learned in this paper are detailed in this section. The extent of this research, though small, could be expanded upon, and lessons learned by this experimentation process should be passed on to future researchers. To better illustrate the struggles of this research, helpful information and suggestions will be made as to the improvement of future experiments. Future researchers are recommended to read this portion of the paper, if nothing else has been learned so far.

7.3.1 Potential insulation of parts

One way to deal with the Seebeck effect is to insulate metallic junctions inside of the cryomodule. This involves a coating of some insulator on the metallic surface between the junctions and mechanical connections of the cryomodule. This, in essence, would cut any current flowing around the cryomodule, and allow for the circuit to be broken, however, it does have its limits. Insulation can be expensive if applied to every cryomodule within a machine, regardless of its use. It should also be noted that even when known metallic junctions are insulated, that others may appear without detection. If there is ground within a cryomodule, it is possible to see a current forming between two pieces of metal at different temperatures. It is also known that small temperature differences, as small as 2-3 K, can generate a voltage difference. At this point, it becomes an issue of what parts of the cryomodule need to be coated, and which do not. Certainly, coating surfaces is not a bad idea, though it is important to weigh the costs and benefits of this performance boost, as well as the practicality of insulating every cryomodule in this way. For a large machine, or any machine for that matter, cavities can and will experience a Seebeck effect, and loss due to that Seebeck effect. The decision to circumvent this issue is one that comes down to cost, time, and resources. In the end, the boost in performance made by insulating these cavities against thermoelectric effects is unknown.

7.3.2 For future use in cryomodules and cavities

The importance of this research that there is now definitive evidence that the Seebeck effect causes the generation of a magnetic field from materials found in a cryomodule. The magnetic field gets trapped within the cavity after it passes its critical temperature, and causes surface resistance, which produces loss. The importance of this loss is that it prevents higher efficiency within the SRF cavities used at FRIB, and prevents future potential upgrades to the machine's capability in that aspect. To be sure, this is something that must be further investigated, but it is not the only conclusion one must make from this paper. All cryomodules, if cooled down conventionally, will produce this effect in some capacity, and generate losses or unwanted effects. One cannot completely do away with the Seebeck effect without first fundamentally understanding the mechanisms that enable it. To do that, it is the recommendation of this paper that future research be carried out at a lower temperature range than the one in this paper. Liquid helium is a sufficient coolant, but due to its limited supply, another coolant should be considered. The design of the measurement apparatus should fit its designed end goal, yet be simple enough to modify that it is not impossible to make changes. More samples should be tested, such as

aluminum, copper, and other grades of steel. These are just a few suggestions, but the following are mistakes made that should be accounted for in future research.
Account for black body radiative heat effects when cooling down the sample. Understand which materials are thermally conductive yet electrically insulate the sample, and decide on one that will not shatter under 50 kelvin. Remember to shield the sample from outside heating effects using insulation, or any other method of temperature control. If possible, calibrate the temperature sensors more than once to assure that they read the same temperature at the same time. The voltage meter used in experimentation should be sensitive enough to measure microvolts. Conduct multiple trials across selected samples, and validate measurement results by comparison to known values, or previous trials for consistency. When choosing a heating element, make sure that it can vary in its heating output, and keep up with the speed at which the sample is chilled. These suggestions apply for all future Seebeck research. For future use in cryomodules, consideration of the above suggestions should be made.

8. Summary

The process of understanding SRF cavities begins with understanding the Q_0 and E_{acc} factors that define performance. These two terms represent the efficiency of the cavity to hold its energy, and to accelerate the particle along the beamline. In this paper, the means of flux trapping in the cavities was investigated, and a major source was found. This source was found to be flux trapping from the magnetic fields generated by an initially unknown source. When a cavity has trapped flux, it can experience RF power loss, which is detrimental to the ability of the cavity to retain its energy. Magnetic shielding was the first method that was attempted to reduce this flux, but with little success. Then, another source was determined by further investigation, known as the Seebeck effect. With little information on its nature, the Seebeck effect was investigated in detail, to determine if the effect could produce magnetic flux strong enough to cause this loss. In addition, the source of this flux, and which materials produced it most, was also investigated.

Measuring the Seebeck effect was able to be performed through cool down of the samples, and the voltage produced was measured. Comparison between the voltage produced and known Seebeck values proved to be challenging, since the Seebeck coefficients for this temperature range (273 – 77 K) had not been characterized yet. The magnetic flux produced by the Seebeck effect was verified during experimentation, though validation of the strength of the field to known values was unable to be completed, due to lack of available data. For the purposes of this thesis, the stainless steel and titanium sample produced the largest magnetic field out of the three samples used. It is the conclusion of this paper that more research must be undertaken to further characterize and understand the metals investigated with respect to their Seebeck coefficients, and produced magnetic fields. Furthermore, improvements to this experimentation process should be made in order to assist with the collection of data, and the reproducibility of the data gathered.